Scanning Nanomagnetometry: Probing Magnetism with Single Spins in Diamond

Inauguraldissertation

zur
Erlangung der Würde eines Doktors der Philosophie
vorgelegt der
Philosophisch-Naturwissenschaftlichen Fakultät
der Universität Basel

von

**Patrick Appel
aus Deutschland**

Basel, 2017

Genehmigt von der Philosophisch-Naturwissenschaftlichen Fakultät
auf Antrag von
Prof. Dr. Patrick Maletinsky
Prof. Dr. Frithjof Nolting

Basel, den 23. Mai 2017

Prof. Dr. Martin Spiess
Dekan

Creative Commons License Deed

Abstract

Scanning nanomagnetometry based on the electronic spin of the nitrogen vacancy (NV) center in diamond is an emerging sensing technology, which allows for the probing of magnetic fields on the nanoscale. High sensitivity, of a few tens of $\mathrm{nT}/\sqrt{\mathrm{Hz}}$, can be achieved by exploiting the extraordinary properties of this special lattice defect. Incorporating this atomic sized sensor in the apex of all-diamond scanning probes allows controlled proximity of the NV center and a sample to be achieved. The resulting resolution of a few tens of nm in combination with an NV's sensitivity offers unique possibilities for exploring new physical properties or phenomena.

In this thesis, we developed and characterized a high performance scanning NV magnetometer and we demonstrate its potential for probing magnetic fields in two applications. We implemented a procedure to fabricate single-crystal, all-diamond scanning probes and developed a highly efficient and robust approach for integrating these devices into our setup. The resulting sensitivities of $\eta_{\mathrm{DC}} \sim 750\,\mathrm{nT}/\sqrt{\mathrm{Hz}}$ for DC and $\eta_{\mathrm{AC}} \sim 114\,\mathrm{nT}/\sqrt{\mathrm{Hz}}$ for AC-magnetic fields and resolution of $50 \pm 32\,\mathrm{nm}$ enabled real space imaging of the stray field of an antiferromagnet and the imaging of microwave magnetic fields with unprecedented spatial resolution. Both applications illustrate the potential of this powerful technique for imaging weak magnetic fields and revealing physical properties that are inaccessible with alternative approaches. Scanning NV magnetometry therefore forms an attractive, new technique, which will have a profound impact on many different research areas ranging from magnetism and advanced material sciences to spintronics and quantum computing.

Contents

Contents

Contents

Contents

Introduction

The detection of magnetic moments of neutrons, protons, electrons or atoms forms a powerful technique for analyzing materials, which has contributed to various research areas, ranging from fundamental physics to chemistry and biology. Visualizing these moments using magnetic resonance imaging (MRI) has revolutionized medical science and has found applications in today's clinical diagnostics. While these conventional detection schemes measure the moment of a large ensemble of spins, the detection and imaging on the single electron or nucleon level remained elusive, until new, advanced imaging schemes were developed. These new approaches combine scanning probe techniques with modern sensors, providing nanoscale resolution and the capability of measuring and imaging the small magnetic field of single electrons [1, 2, 3]. Such highly sensitive, nanoscale magnetic field sensing has many applications and provides novel insights in nanotechnologies ranging from medicine and biology to magnetism, advanced material sciences, spintronics and quantum computing.

As a consequence of this multitude of potential applications, many different nanoscale magnetic field sensors have been realized and optimized in recent decades. The most important figure of merit for such sensors is the magnetic field sensitivity, which describes the smallest magnetic field that can be detected within a given measurement time. Moreover, as the dipole field of a single spin decreases with the distance cubed, a magnetic field sensor must combine a small sensor size with the ability to be placed in close proximity to the sample in order to be capable of measuring the stray field. The state-of-the-art sensitivity and sensor-to-sample distance for the four most promising scanning nanomagnetometry techniques are summarized in Fig. 1 and will be discussed in the following.

Scanning Hall probe microscopy (SHPM) utilizes Hall sensors mounted to micro scanning systems for measuring the stray magnetic field of a target. These sensors achieve sensitivities of $nT/\sqrt{Hz}$ and a sensor-to-sample distance of $\sim 1\mu m$. For applications in nanoscale imaging this distance as well as the sensor's volume has to be reduced. However, a reduction in the active area of the Hall sensor typically comes at the expense of a smaller sensitivity [6]. Therefore, improvements to bring this technique to nanoscale spatial resolution are challenging.

In contrast to SHPM, the magnetic tip of a magnetic resonance force microscope (MRFM) can be placed at a distance of $\sim 100\,nm$ to a target spin. By ultra sensitive detection of the force between the target spin and the magnetic tip, the field of a

1
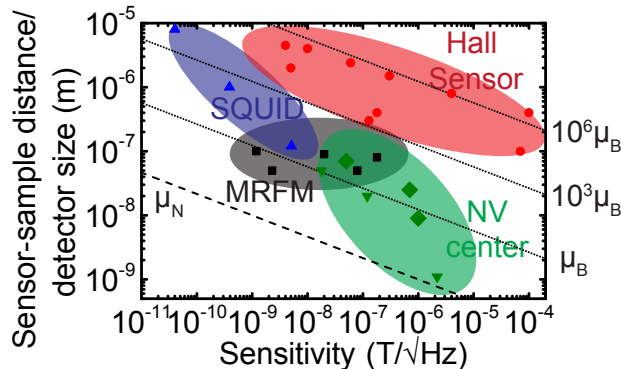
Figure 1: Comparison of various scanning nanomagnetometry techniques (adapted and extended from Ref. [4] and Ref. [5]). The data points represent experimentally demonstrated magnetic field sensitivities for Hall sensors [6], scanning SQUID sensors [3, 7, 8], magnetic resonance force microscopy [1, 9, 10, 11, 12], NV center sensors [2, 13, 14, 15, 16, 17] as a function of the sensor-sample distance. The larger green diamonds corresponds to experiments performed during this thesis. For the Hall sensors the detector size is used as an estimation for the characteristic length scale. An optimal sensor for nanoscale spin sensing combines high magnetic field sensitivity with a small sensor-sample distance and a small detector size. Thus, the best magnetic moment sensitivity correspond to the the lower left region of the graph. Diagonal dotted lines indicate the threshold for the detection of 10^6, 10^3, or 1 electron spin (dipole moment $1\mu_B$) and the dashed line corresponds to the threshold for detecting a single nuclear spin (dipole moment $1\mu_N$) within 1s.

single electron can be measured [1]. However, MRFM is restricted to low temperature and the stray field of the magnetic tip perturbs the magnetic state of a target, which limits the range of applications.

For sensitive, non invasive detection of magnetic fields, superconducting quantum interference devices (SQUIDs) can be applied. These devices can reach a sensitivity of $1\,\mathrm{fT}/\sqrt{Hz}$ [18]. However, it has proven difficult to ensure a close proximity of the sensor to the sample. First approaches used planar geometries, resulting in large lateral sizes of the devices, and thereby limiting the ability to place the SQUID near a target. Recently, the approach of fabricating SQUIDs on tips, which have diameter of a several tens of nm, has attracted a lot of attention [3]. Although the sensitivity is reduced with the decreasing lateral sizes, this approach still allows for the fabrication of SQUIDS with an excellent sensitivity of $5.1\,\mathrm{nT}/\sqrt{\mathrm{Hz}}$. These nanoscale SQUIDs on the tip of capillary quartz needles can be scanned with a sensor-to-sample distance of $120\,\mathrm{nm}$ across the sample and are predicted to be capable of scanning single electron spins [3]. However, this approach is restricted to a cryogenic environment, which again limits its applicability.

A promising new sensor that can be operated in ambient conditions is the nitrogen vacancy (NV) center in diamond. The NV center is an optically active lattice defect with a spin $S = 1$ ground state. Its exceptionally long coherence time (up tp 1 ms) combined with efficient initialization and readout capabilities allows sensitivities of a few $nT/\sqrt{Hz}$ to be reached [19] making the NV center a remarkable atomic scale sensor. The first experiments in scanning NV magnetometry employed nanodiamonds grafted to atomic force microscope (AFM) tips, which already combined an extraordinary resolution of several tens of nm with the sensitivity of the NV center. Recently a novel, advanced approach, that relies on the fabrication of robust, all-diamond, single crystalline scanning probes has been developed [20]. Scanning probes, with advanced optical properties that improve the sensitivity, provide control of the NV-to-sample distance to within a few tens of nm. This improvement enabled imaging of the magnetic field of a single electron spin[2]. Moreover, scanning NV magnetometry has recently been applied to study magnetic systems [21, 22], where its superior combination of sensitivity and resolution revealed the internal structure of a domain wall [23]. These first applications demonstrate the excellent imaging capabilities scanning NV magnetometry offers and illustrate the potential for exploring physics that is inaccessible with alternative approaches.

Scope of the thesis

This thesis describes the implementation of a scanning NV magnetometer for highly sensitive, nanoscale imaging of magnetic fields and demonstrates the excellent performance of this technique in two applications: real space stray field imaging of antiferromagnets and microwave imaging with unprecedented nanoscale resolution.

In Chap. 1 we introduce the exceptional properties of the NV center exploited for magnetic field sensing and discuss the sensing schemes used in this thesis. Chap. 2 describes the implementation of a scanning NV magnetometer. We start with a description of the experimental setup and then present the fabrication process of the all-diamond scanning probes, which was developed during this thesis. The performance of our scanning probe based magnetometer is demonstrated by introducing the basic imaging modes applied to measure the nanoscale stray field of single Ni nanorods. Finally, we discuss the state-of-the-art DC sensitivity and resolution and outline possibilities for improving the performance of our scanning NV magnetometer.

In Chap. 3 we apply our magnetometer to study the magnetic stray field of antiferromagnets (AFs). We demonstrate the first quantitative, real space imaging of the stray field of the AF Cr_2O_3.

In Chap. 4 we demonstrate our scanning NV magnetometer's ability to measure and image microwave (MW) magnetic fields. In a proof of concept experiment, we quantitatively image the magnetic field generated by a high frequency (GHz) MW current with nanoscale spatial resolution.

Both of these applications establish scanning NV magnetometry as a versatile and high performance tool for imaging weak magnetic fields.

To conclude, we outline future applications where the superior sensing capabilities can be applied to analyze physical properties or phenomena that are challenging to measure using alternative techniques.

Part of the results presented in Chap. 2, Chap. 3 and Chap. 4 have been published in Reference [16], [17] and [24], respectively. These references are separately listed at the end of this thesis.

Chapter 1

The Nitrogen Vacancy Center

The nitrogen vacancy (NV) center in diamond forms a highly promising sensor: On the one hand, its unique combination of long spin coherence times and efficient optical spin readout enables the detection of magnetic and electric fields, as well as local temperature. On the other hand, the NV center is a highly photostable single photon source and therefore an ideal emitter for near-field scanning and single photon microscopy. In this thesis, we will focus on the sensitive evaluation of magnetic fields with a nanoscale spatial resolution using single NV centers. All properties relevant for magnetic field sensing are sustained from cryogenic temperatures up to 550 K and will be introduced in this chapter. We give an overview of the basic properties exploited for magnetic field sensing and discuss the basic sensing schemes together with their operation ranges and achievable sensitivities.

1.1 The nitrogen vacancy color center in diamond

Diamond is an exceptional material with various extraordinary properties. Its lattice is formed by carbon (C) atoms in a face-centered cubic (fcc) lattice structure with a two-atomic base. Similar to zincblende structure, all neighbors of a C atom build a regular tetrahedron with covalent bonds. The exceptional hardness and thermal conductivity of diamond results from these strong bonds. Furthermore, diamond is an electrical insulator with an indirect band gap of $5.48\,\text{eV}$. Due to this large band gap, diamond is transparent from the infrared to the deep UV region which makes it an ideal host for various color centers.

One of the best studied color centers in diamond is the NV center, a stable lattice defect consisting of a vacancy and a neighboring, substitutional nitrogen (N) atom (see Fig. 1.1 (a)). Nitrogen is one of the common impurities in diamond and can be found as single substitutional defects, NV centers or larger complexes containing multiple N atoms. The NV center is energetically favored and can be synthetically created by various techniques. One approach relies on controlling the diamond growth parameters (gas composition, pressure, etc.) to allow NV centers to form during the plasma-enhanced, chemical-vapor-deposition based growth process

of synthetic diamond [25]. In contrast to this in situ creation, the NV center can also be incorporated in diamond after the growth process. One commonly used technique is the implantation of N by ion irradiation. After the implantation the diamond hosts N as well as vacancies that are created by scattering during the implantation process. These vacancies can diffuse while the diamond is annealed at $\sim 800\,^\circ$C leading to the formation of NV centers in the nitrogen implanted diamond samples. Alternatively, N rich diamond can be used as a starting material and vacancies can be created by ion implantation or electron irradiation forming NV centers during the subsequent annealing.

Two different optically active forms of the NV center have been observed: the charge-neutral and the negatively charged NV^0 and NV^-, respectively. The charge-neutral NV^0 center consists of 5 electrons: The lone electron pair of the N atom and 3 electrons from the dangling bonds of the C atoms surrounding the vacancy, resulting in an overall spin of 1/2. Depending on the Fermi level in the diamond, an additional electron (most likely from substitutional N in the surrounding diamond) can be captured, resulting in the NV^- with an overall spin of 1. The Fermi level and thereby the charge state can be electronically tuned [26], controlled via the surface potential [27, 28] or by selective laser excitation [29, 30]. However, only NV^- has the extraordinary properties exploited for sensing. Note that charge conversion is subject to current research and it was recently demonstrated that the conversion can be exploited for enhanced spin readout [30]. In this thesis, we will focus on the negatively charged NV^-, which will be simply denoted as the NV center.
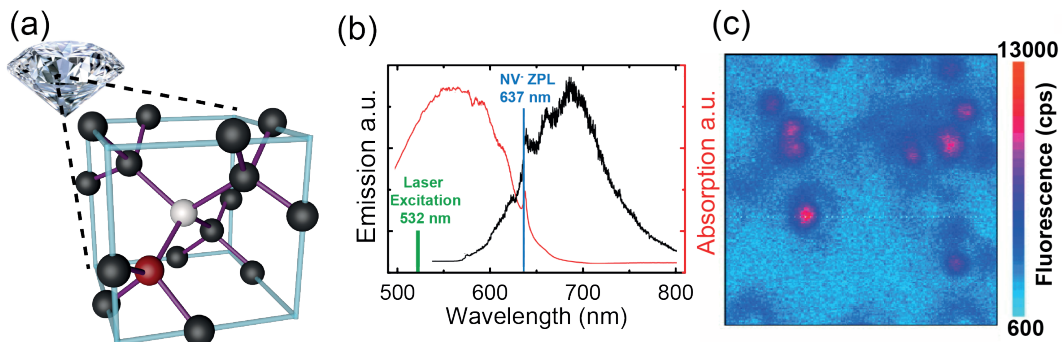
Figure 1.1: (a) Atomic structure of a nitrogen vacancy (NV) defect center in the diamond crystal. Black spheres indicate the carbon lattice. The NV center consists of a nitrogen (red sphere) and a neighboring vacancy (white sphere). (b) Absorption and emission spectrum of the NV center (adapted from [31]) and (c) confocal microscopy map of NV centers in diamond. Figure reprinted from [32]. Reprinted with permission from AAAS. The bright spots arise from the photoluminescence of single NV centers.

The NV center is a color center that absorbs green light (see absorption spectrum in Fig. 1.1 (b)) leading to a pink appearance for diamonds with very high NV con-

centration. Additionally, it exhibits broadband red shifted emission with the zero phonon line (ZPL) at 1.945 eV (637 nm). In 1997, Gruber et al. [32] demonstrated that single NV centers can optically be detected using non resonant excitation with a 532 nm laser combined with confocal microscopy (see Fig. 1.1 (c)) and that its spin state can be addressed through optically detected magnetic resonance (ODMR). This work inspired several research groups to analyze and study the structure of single NV centers and forms the basic technique for addressing single NV centers.

1.2 Electronic structure of the NV center

To understand the origin of the extraordinary properties of the NV center for magnetic field sensing, the knowledge of the electronic structure of the NV center is essential. While a complete theoretical treatment of the origin of the level structure is beyond the scope of this thesis (more detailed descriptions can be found in [33, 34, 35]), we present the model depicted in Fig. 1.2, which explains all properties relevant for magnetic field sensing [36, 37].

The 6 electrons of the NV center reveal a C_{3v}-symmetry, with the symmetry axis given by the vector connecting the N atom and the vacancy. The tetrahedral geometry of the diamond allows four different NV center orientations, corresponding to the four equivalent $\langle 111 \rangle$ directions of the diamond lattice. The 6 electrons will quantize according to this symmetry axis and form a spin triplet ($S = 1$) in the ground (gs) and first excited state (es), which are separated by 1.945 eV. The triplet states with the magnetic quantum number $m_s^{\mathrm{gs,es}} = 0$ and the degenerate $m_s^{\mathrm{gs,es}} = \pm 1$ states experience a zero field splitting (ZFS) due to spin-spin-interaction. The ZFS is $D_{\mathrm{gs}} = 2.87\,\mathrm{GHz}$ for the ground and $D_{\mathrm{es}} = 1.42\,\mathrm{GHz}$ for the excited state. A singlet state is located energetically between the ground and excited state. Note that the structure of this singlet state is still not fully understood and in particular two singlet states with a radiative transition at 1043 nm were observed [39, 35].

The ability to optically initialize and read out the spin state of the NV center forms the basis for magnetic field sensing. These properties arise from the transitions between the electron levels. The transitions between the ground and the first excited states are largely spin conserving, with radiative lifetimes of $\tau \sim 15\,\mathrm{ns}$ [37]. There exists a non radiative decay from the $m_s^{\mathrm{es}} = \pm 1$ excited state to the singlet state with lifetimes of $\tau \sim 20\,\mathrm{ns}$. Furthermore, there are non radiative decay channels from the singlet to the ground states with lifetimes of $\tau \sim 1\,\mu\mathrm{s}$ [37]. Due to this non radiative, non spin-preserving decay channels the spin can be initialized in the $m_s^{\mathrm{gs}} = 0$ state by continuous laser excitation. The polarization fidelity of this initialization is determined by all decay rates involved and can reach 95% [40]. The second consequence of this non radiative, spin selective transition is a spin dependent fluorescence of the NV center. When exciting an NV center, which is initialized in the $m_s^{\mathrm{gs}} = 0$ state, population will be pumped into $m_s^{\mathrm{es}} = 0$. From this excited state, the population can only radiatively relax, whereas population in the $m_s^{\mathrm{es}} = \pm 1$ excited state has a significant probability to relax non radiatively via the singlet state and
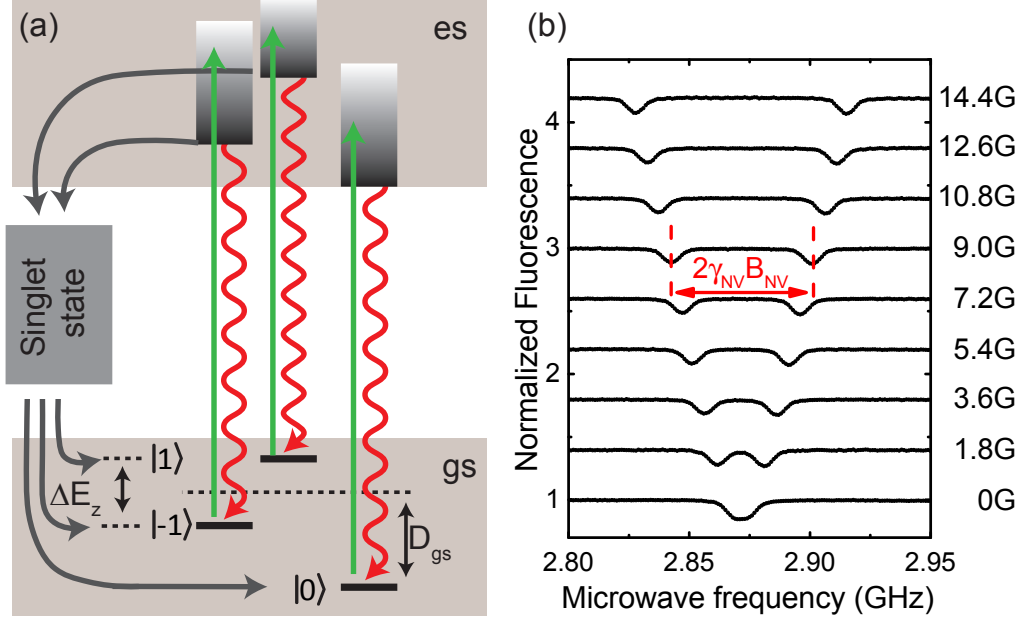
Figure 1.2: (a) Model of the level structure of the NV center. The ground (gs) and excited state (es) (gray boxes) are spin triplets consisting of three levels ($|0\rangle$ and $|\pm1\rangle$) with the corresponding magnetic quantum numbers ($m_s = 0, \pm1$). A green laser (green arrow) excites the transitions from the ground to the excited state and the red shifted fluorescence (red arrows) is detected. The gray arrow indicates a non-radiative relaxation path involving the singlet state leading to an intersystem crossing. This intersystem crossing leads to the ability to initialize the NV into the $m_s = 0$ spin state and to spin dependent fluorescence. Together with the ability to coherently drive ground state transitions using resonant microwave (MW) magnetic fields these properties are essential for magnetic field sensing. (b) Optically detected electron spin resonance (ESR) spectra of the NV center recorded in various applied magnetic fields. The ground state transitions are shifted by the Zeeman splitting, providing a quantitative measurement of the magnetic field projection B_{NV} along the NV axis. These spectra are recorded by monitoring the NV fluorescence intensity, while sweeping the frequency of the MW field. Spectra for different magnetic fields are shifted vertically for clarity (this figure is adapted from [38]).

therefore result in a significant lower fluorescence rate. Measuring the fluorescence intensity therefore enables the efficient detection of the spin state. This detection in addition to the ability of initializing the spin state with a high fidelity are the basic properties exploited for sensing. Note that the spin state of the excited state can also be adressed using ODMR [41]. However, a reduced fluorescence contrast is observed which results in a reduced sensitivity (see Sec. 1.7). Thus, the magnetic

field sensing protocols and applications, described in this thesis, exploit the ground state manifold. In the following we only refer to the ground state manifold and its quantum number as m_s and omit the indices m_s^{gs} and m_s^{es}.

1.3 Electron spin resonance

Magnetic resonance spectroscopy is a commonly used technique to read out the transition frequencies of molecules, atoms or spins [42]. Typically, a magnetic field at microwave (MW) frequencies is applied and its frequency is swept. When the MW frequency matches the transition frequency, the MW is absorbed and induces spin flips (see Sec. 1.6.1). This absorption can be detected and the electron transition frequencies can be measured. In electron spin resonance (ESR) experiments, a known magnetic field is applied to induce a Zeeman splitting for a target spin. This splitting can then be analyzed to gain information about the target. For a known target, such as the NV center, the Zeeman splitting can, on the other hand, be used to quantitatively evaluate magnetic fields.

In contrast to conventional ESR, the NV center's spin state can efficiently be detected optically and therefore ESR for the NV center is also referred to as optically detected magnetic resonance (ODMR). In ODMR measurements the NV center is excited by a continuous wave (CW) laser to initialize the NV into the bright $m_s = 0$ state while the frequency of an applied MW magnetic field is swept. When the MW frequency matches the transition frequency of the NV center, the spin can be flipped into the darker $m_s = \pm 1$ state and a decrease in overall fluorescence is detected, as depicted in Fig. 1.2. If no magnetic field is applied a resonance at the ZFS of $D = 2.87\,\text{GHz}$ can be observed. If an on axis magnetic field is applied the degeneracy of the two $m_s = \pm 1$ states will be lifted by the Zeeman effect and two resonances will be detected. In a small magnetic field (see Sec. 1.4), the splitting between the two resonances is given by $2\gamma_{NV}B_{NV}$, where $\gamma_{\text{NV}} = 28\,\text{MHz/mT}$ is the gyromagnetic ratio of the NV center and B_{NV} is the magnetic field along the NV quantization axis. An unknown magnetic field can therefore be evaluated quantitatively by detecting the resonances in an ESR spectrum.

1.4 The ground state spin Hamiltonian

Magnetic field sensing using NV centers relies on evaluating the Zeeman shift induced by an arbitrary magnetic field. Thus, understanding the effect of an arbitrary magnetic field on the NV center spin states is crucial. The ground state response to a magnetic field can be described by the following spin Hamiltonian [38]:

$$H = hDS_z^2 + hE(S_x^2 - S_y^2) + h\gamma_{\text{NV}}\vec{B} \cdot \vec{S} \tag{1.1}$$

where z is the NV quantization axis as depicted in Fig. 1.3 (a), h is Planck's constant, D and E are the axial and transverse ZFS parameters, S_x, S_y and S_z the Pauli matrices.

The first term describes the zero-field-splitting $D \approx 2.87\,\mathrm{GHz}$, which results from spin-spin interaction. This parameter changes with temperature by $\sim 80\,\mathrm{kHz/K}$ at room temperature [39], which allows the NV center to also be utilized for temperature sensing. The second term in Eq. 1.1 describes the effect of local strain in the diamond matrix. Thus, the strain parameter E varies between different diamond matrices hosting the NV center. For the synthetic, high purity diamond used in this thesis, E is typically $\sim 100\,\mathrm{kHz}$ and can be neglected for all practical purpose.

The last term in Eq. 1.1 describes the Zeeman shift due to an arbitrary external magnetic field. For analyzing the impact of an arbitrary magnetic field on spin states, the eigenstates of this Hamiltonian need to be determined.
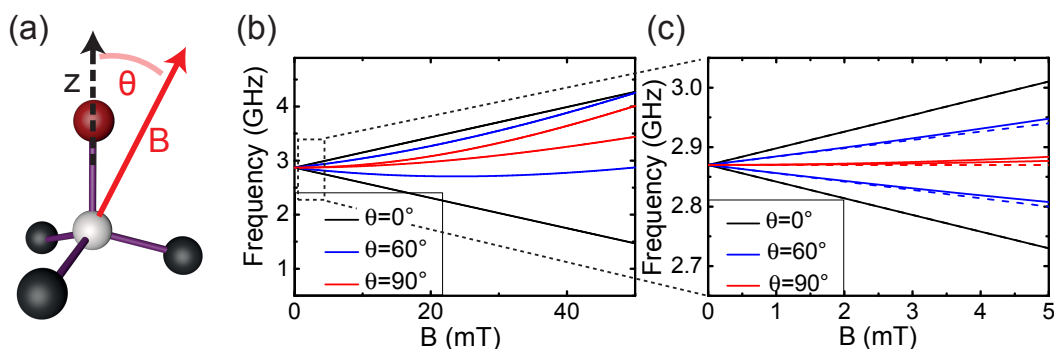
Figure 1.3: (a) A magnetic field B is applied with an angle θ to the NV axis z. (b) ESR frequencies $f_{m_s=\pm1}$ as a function of applied magnetic field B for different θ determined from the eigenenergies of the Hamiltonian (Eq. 1.1). (c) Weak magnetic field regime: The eigenenergies can by approximated by the dashed lines obtained by the linear Zeeman effect described by Eq. 1.2 (figure adapted from [38]).

We first consider the eigenenergies of the Hamiltonian (Eq. 1.1) for a magnetic field aligned with the NV axis [38]:

$$f_{m_s=\pm1} = D \pm \sqrt{(\gamma_{\mathrm{NV}}B_{NV})^2 + E^2}. \tag{1.2}$$

A magnetic field coinciding with the NV axis (with $B_{NV} \gg h/g\mu_{\mathrm{Bohr}}E$) results in a linear Zeeman effect with a splitting proportional to B_{NV}, with a proportionality constant γ_{NV}, as depicted in Fig 1.3 (b).

If the magnetic field does not coincide with the NV axis, the Hamiltonian (Eq. 1.1) needs to be diagonalized to determine the eigenenergies. Assuming that the magnetic field component orthogonal to the NV axis is small ($B_{\mathrm{ortho}} < 5\,\mathrm{mT}$) results in a perturbation of the eigenstates, which is depicted in Fig. 1.3 (b). For these magnetic fields, the splitting is, in a good approximation, described by the linear Zeeman shift arising from the magnetic field projected onto the NV axis (as indicated by the dashed lines in Fig. 1.3 (c)). For magnetic fields with large components orthogonal to the NV axis ($B_{\mathrm{ortho}} > 5\,\mathrm{mT}$) , the quantization axis is not defined

by the NV axis and the magnetic states become mixed. Therefore the Hamiltonian has to be diagonalized to describe the eigenenergies of the NV center. Because the newly formed eigenstates are mixed states, the transition rates between these states are also a mixture of the transition rates described in Sec. 1.2. The mixing of the transition rates leads to the breakdown of the spin dependent fluorescence as well as a decrease in the overall fluorescence [37]. Magnetic fields with large components orthogonal to the NV quantization axis ($\gg 1\,\mathrm{mT}$) can therefore be detected by measuring the overall fluorescence rate of the NV center [37, 43].

1.5 Sensitivity

The major figure of merit for magnetic field sensing is the sensitivity η. It defines the magnetic field that can be detected in a given measurement time T

$$\eta = \delta B \sqrt{T}, \tag{1.3}$$

where δB is the smallest magnetic field obtained for a signal-to-noise ratio (SNR) of 1. δB can be derived from the magnetic field dependent signal. In ESR measurements, the signal $I(f)$ (in counts per second, cps) can be described by the formula [44]

$$I(f) = I_0 \left[1 - C_{\mathrm{ESR}} F \left(\frac{f - f_{\mathrm{NV}}}{\Delta f} \right) \right], \tag{1.4}$$

where I_0 is the average count rate of the NV center, C_{ESR} is the ESR contrast and F is the line shape profile. The profile depends on the MW driving frequency f, the NV-transition frequency f_{NV} and the linewidth Δf (defined as the full width at half maximum (FWHM)). Under weak driving conditions (weak optical pumping and weak MW fields) the line shape of the NV center is described by a Gaussian. Under strong driving conditions, a Lorentzian profile needs to be considered [44].

In Fig. 1.4, we used a Gaussian fit to describe the ESR

$$I = I_0 \left[1 - C_{\mathrm{ESR}} e^{\left(-\frac{(f - f_{\mathrm{NV}})^2}{2\sigma^2} \right)} \right]. \tag{1.5}$$

The fit yields $I_0 = 205\,\mathrm{kcps}$, $C_{\mathrm{ESR}} = 0.19$, $f_{\mathrm{NV}} = 2.821\,\mathrm{GHz}$ and $\sigma = 4.96\,\mathrm{MHz}$. Note that the depicted ESR spectrum was measured under moderate driving conditions, which can be approximated by the Gaussian profile for small detuning.

The maximum, magnetic field-dependent signal is illustrated by the red line in Fig. 1.4 and can be deduced from the maximum slope of the ESR spectrum as follows

$$S = \left. \frac{\partial I}{\partial B} \right|_{\mathrm{max}} B = \gamma_{\mathrm{NV}} \left. \frac{\partial I}{\partial f} \right|_{\mathrm{max}} B = \gamma_{\mathrm{NV}} I_0 C_{\mathrm{ESR}} \frac{B}{\sqrt{e}\sigma}. \tag{1.6}$$

Here, the magnetic field B corresponds to a frequency shift $f = \gamma_{\mathrm{NV}} B$ (assuming a linear Zeeman shift, see Sec. 1.4). The noise N for the NV center is dominated by
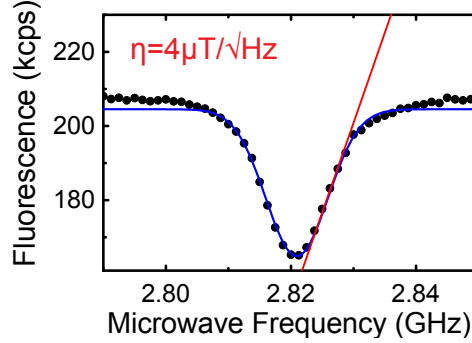
Figure 1.4: ESR measurements. Data are plotted in black and a Gaussian fit (see main text) is depicted in blue. The red line indicates the maximum signal response at the optimal working point, which is used to deduce the sensitivity of $\eta = 4\,\mu\mathrm{T}/\sqrt{\mathrm{Hz}}$ (data taken from [16]).

photon shot-noise [45]. With the shot noise of $N = \sqrt{I_0}$ we deduce the sensitivity

$$\eta_{\mathrm{DC,ESR}} = \frac{N}{\partial S/\partial B|_{\max}}\sqrt{T} = \frac{\sqrt{e}}{\gamma_{\mathrm{NV}}}\frac{\sigma}{C_{\mathrm{ESR}}\sqrt{I_0}}. \tag{1.7}$$

Analogously to the Gaussian profile a sensitivity for a Lorentzian profile can be calculated. We define the general sensitivity as

$$\eta_{\mathrm{DC,ESR}} = \frac{1}{\gamma_{\mathrm{NV}}}\frac{\sqrt{I}}{\delta I/\delta f_{\mathrm{MW}}} = P_F\frac{1}{\gamma_{\mathrm{NV}}}\frac{\Delta f}{C_{\mathrm{ESR}}\sqrt{I_0}}, \tag{1.8}$$

where P_F is a numerical parameter for the specific profile [44]. This parameter is given by $P_G = \sqrt{e/8\ln 2} \approx 0.70$ for a Gaussian and $P_L = 4/3\sqrt{3} \approx 0.77$ for a Lorentzian profile. For the depicted NV center in a scanning probe, we obtain a sensitivity of $\eta_{\mathrm{ESR}} = 4\mu\mathrm{T}/\sqrt{\mathrm{Hz}}$.

This sensitivity can be improved by minimizing the linewidth Δf. Decreasing the optical and MW power will result in less broadening of the NV resonance, which will decrease Δf. However, decreasing these parameters will also reduce C_{ESR} and I_0, which has an adverse effect on the sensitivity. Hence, the impact of the optical and MW power on the NV center's ESR spectrum has to be analyzed, which allows to determine the optimal driving conditions for a particular NV center. Alternatively, pulsing techniques can be applied to eliminate the effect of optical power broadening in the ESR [44]. With these techniques, a FWHM Δf that is fundamentally limited by the dephasing rate $\Gamma_2^* = 1/T_2^*$ (typically $T_2^* \sim 1\,\mu\mathrm{s}$ for shallow NV center) can be reached, which results in a sensitivity of (see discussion in Sec. 1.7)

$$\eta \sim \frac{1}{\gamma_{\mathrm{NV}}}\frac{1}{C\sqrt{I_0}}\frac{1}{\sqrt{T_2^*}} \approx 500\,\mathrm{nT}/\sqrt{\mathrm{Hz}}. \tag{1.9}$$

Using coherent spin manipulation protocols, which will be discussed in the following sections, the NV center can be decoupled from the environment, which further extends the coherence time and allows sensitivities of $28\,\mathrm{nT}/\sqrt{\mathrm{Hz}}$ to be reached.

1.6 Coherent spin manipulation

Coherent manipulation protocols, which are commonly used in nuclear magnetic resonance (NMR), can be applied to exploit the full potential of NV centers for magnetic field sensing. These techniques rely on having a quantum system with two energy levels, which can be coherently manipulated and which interact with magnetic fields. By applying different pulsed manipulation protocols, the long coherence times of the NV center spin can be exploited in order to increase the sensitivity. In this section, we will introduce the basic manipulation protocols and discuss their operation ranges and sensitivities, which determines important figures of merit for the NV center's ability to sense magnetic fields.

1.6.1 Two level system

Generally, the coherent detection techniques are used to determine the magnetic field dependence of the population of a two level system, which is coherently manipulated. The magnetic field induced shift of the two levels can be evaluated efficiently by measuring the population of the two levels. For the NV center, the two states can either represent the subset of the $m_s = 0, 1$ or the $m_s = 0, -1$ ground states and its population is evaluated using optical methods. We restrict the following discussion on the $m_s = 0, 1$ level and refer to the two levels as the $|0\rangle$ and $|1\rangle$ state. The ground state of the NV center can be described by a Hamiltonian (see Sec. 1.4), which in the basis $|0\rangle = (0, 1)^T$, $|1\rangle = (1, 0)^T$, can be described by

$$H_0 = \begin{bmatrix} \hbar\omega & 0 \\ 0 & 0 \end{bmatrix},$$
(1.10)

where $\hbar\omega$ corresponds to the energy difference between the two levels. An arbitrary pure quantum state in this basis can be written as

$$|\psi\rangle = c_0 |0\rangle + c_1 |1\rangle,$$
(1.11)

where c_0 and c_1 are complex constants which have to comply with the continuity equation. The time evolution of the wavefunction is given by the Schrödinger equation

$$i\hbar\frac{\partial |\psi\rangle}{\partial t} = H_0 |\psi\rangle.$$
(1.12)

By solving this equation, we can determine the time evolution of a particular quantum state. If the system described by the Hamiltonian in Eq. 1.10 is initialized in the $|0\rangle$ state, it remains in this state. To manipulate the spin and induce spin

flips, we therefore need an additional interaction. The interaction most commonly used to produce spin flips is an alternating MW magnetic field perpendicular to the quantization axis [42]. A magnetic field that oscillates with a frequency ω_1 in the x direction (with z being the quantization axis) can be described as a superposition of two circularly polarized magnetic fields

$$
\begin{aligned}
\vec{B}_{\mathrm{MW}}(t) &= B_{1,\mathrm{MW}} \cos(\omega_1 t) \vec{e_x} \\
&= B_{\mathrm{MW}}^+ \left[\cos(\omega_1 t)\vec{e_x} + \sin(\omega_1 t)\vec{e_y}\right] + B_{\mathrm{MW}}^- \left[\cos(\omega_1 t)\vec{e_x} - \sin(\omega_1 t)\vec{e_y}\right]
\end{aligned}
\tag{1.13}
$$

where the first and second term describe the right handed and left handed, circularly polarized magnetic field with the amplitudes B_{MW}^+ and B_{MW}^-, which for linear polarized MW fields are given by $B_{\mathrm{MW}}^\pm = 0.5 B_{1,\mathrm{MW}}$. The interaction Hamiltonian H_{int} is given by:

$$
\begin{aligned}
H_{\mathrm{int}} &= g\mu_{\mathrm{Bohr}} B_{0,\mathrm{MW}} \cos(\omega_1 t) S_x \\
&= g\mu_{\mathrm{Bohr}} \left[B_{\mathrm{MW}}^+ \left(\cos(\omega_1 t)S_x + \sin(\omega_1 t)S_y\right) + B_{\mathrm{MW}}^- \left(\cos(\omega_1 t)S_x - \sin(\omega_1 t)S_y\right)\right] \\
&= g\mu_{\mathrm{Bohr}} \left[B_{\mathrm{MW}}^+ \left(e^{-i\omega_1 t}S_+ + e^{i\omega_1 t}S_-\right) + B_{\mathrm{MW}}^- \left(e^{i\omega_1 t}S_+ + e^{-i\omega_1 t}S_-\right)\right], \quad (1.14)
\end{aligned}
$$

where we introduce the raising and lowering operator $S_\pm = 1/2(S_x \pm iS_y)$.

Due to selection rules for magnetic dipole transitions, the first and the second term in Eq. 1.14 (corresponding to the right and left handed circularly polarized magnetic field components) only excite transitions with a difference in the magnetic quantum number of $\Delta m = \pm 1$ [42]. Therefore the transition from $m_s = 0 \rightarrow m_s = 1$ can only be excited by the right handed, circularly polarized magnetic field components whereas the $m_s = 0 \rightarrow m_s = -1$ transition can only be excited by the left handed circularly polarized magnetic fields. We will in the following only consider the B_{MW}^+ component of an alternating field in resonance with the $m_s = 0$ to $m_s = 1$ transition, where $\omega_1 = \omega$. The overall Hamiltonian $H = H_0 + H_{\mathrm{int}}$ describing the system is

$$
H = \begin{bmatrix} \hbar\omega & \frac{g\mu_{\mathrm{Bohr}}}{2}B_{\mathrm{MW}}^+ e^{-i\omega t} \\ \frac{g\mu_{\mathrm{Bohr}}}{2}B_{\mathrm{MW}}^+ e^{i\omega t} & 0 \end{bmatrix} = \hbar \begin{bmatrix} \omega & \frac{\Omega}{2}e^{-i\omega t} \\ \frac{\Omega}{2}e^{i\omega t} & 0 \end{bmatrix}
\tag{1.15}
$$

where we introduce the Rabi frequency $\Omega = \frac{g\mu_{\mathrm{Bohr}}}{\hbar}B_{\mathrm{MW}}^+ = 2\pi\gamma_{\mathrm{NV}}B_{\mathrm{MW}}^+$. B_{MW}^+ corresponds to the amplitude of the right handed circularly polarized magnetic field. The Schrödinger equation for the electron spin under MW driving results in two coupled differential equations

$$
\frac{\partial c_0}{\partial t} = -i\,\frac{\Omega}{2}e^{i\omega t}c_1
\tag{1.16}
$$

$$
\frac{\partial c_1}{\partial t} = -i\omega c_1 - i\,\frac{\Omega}{2}e^{-i\omega t}c_0
\tag{1.17}
$$

We transform our variables into the rotating frame, a frame that rotates around the quantization axis with a frequency given by the eigenfrequency ω

$$C_1 = c_1 e^{i\omega t}, \tag{1.18}$$

which results in two coupled differential equations

$$\frac{\partial c_0}{\partial t} = -i\,\frac{\Omega}{2}C_1 \tag{1.19}$$

$$\frac{\partial C_1}{\partial t} = -i\,\frac{\Omega}{2}c_0. \tag{1.20}$$

A general solution for these coupled differential equations is

$$c_0 = a_0(0)\cos\left(\frac{\Omega}{2}t\right) + i\,a_1(0)\sin\left(\frac{\Omega}{2}t\right) \tag{1.21}$$

$$C_1 = a_1(0)\cos\left(\frac{\Omega}{2}t\right) + i\,a_0(0)\sin\left(\frac{\Omega}{2}t\right), \tag{1.22}$$

where $a_0(0)$, $a_1(0)$ are constants, which are set by the spin's initial conditions. Assuming the system to be initialized in $|0\rangle$ state yields $a_0(0) = 1$ and $a_1(0) = 0$. The upper state probability is then given by

$$P_1(t) = |C_1|^2 = |\sin\left(\frac{\Omega}{2}t\right)|^2 = \frac{1}{2}\left(1 - \cos\left(\Omega t\right)\right), \tag{1.23}$$

which can be measured in experiments. This equation illustrates that a MW magnetic field coherently drives spin flips leading to oscillations with a frequency given by $\Omega = 2\pi\gamma_{\mathrm{NV}}B_{\mathrm{MW}}^+$. These oscillations are known as Rabi oscillations. MW pulses thereby allow coherent manipulation of the spin state, an essential tool used in the magnetic field sensing schemes discussed in the following sections.

1.6.2 Decoherence

The NV center not only interacts with MW pulses but also with its environment. Due to this interaction, the spin state will lose its information and decay into a thermal equilibrium state. This decoherence process is typically characterized by the relaxation T_1, the dephasing T_2^* and decoherence time T_2.

The relaxation T_1 describes the time for the system to relax to thermal equilibrium when it is initialized in one of its eigenstates ($m_s = 0, m_s = \pm 1$). This time depends on noise at the transition frequency, which for the NV center corresponds to high frequency noise ($\sim$GHz) caused by lattice phonons in the diamond and spin or charge noise at the surface. Typically shallowly implanted NV centers in high purity diamond, such as those used in this thesis, exhibit T_1 times of a few ms at room temperature [46, 47]. Note that the relaxation rate strongly depends on temperature and can reach $T_1 \gg 1\,\mathrm{s}$ in a cryogenic environment [46, 48].

The dephasing time T_2^* and the decoherence time T_2 describe the time during which the phase information of a superposition state (see Eq. 1.11) is lost. The dephasing time T_2^* is measured using Ramsey interferometry (see Sec. 1.6.5) and depends on slow magnetic field noise. In contrast, the decoherence time T_2 measured using Spin Echo spectroscopy is insensitive to slow magnetic field noise and exhibits a maximum sensitivity at MHz frequencies (see Sec. 1.6.6 and 1.7). The noise in both regimes is governed by environmental spin impurities. In the high purity diamond samples, the spin bath is dominated by ^{13}C nuclear spins. ^{13}C isotopes are present with a natural abundance of 1.1% in the diamond lattice. Additionally, a spin bath attributed to surface spins could be detected for shallow NV centers [47, 49]. All these spins interact with the NV center and thereby limit the dephasing and decoherence time. For NV centers implanted $\sim 10\,$nm below the surface of high purity diamond, typically the dephasing T_2^* is $\sim 1\,\mu$s, whereas the decoherence time T_2 is $\sim 100\mu$s [47].

1.6.3 Spin readout

The NV center spin states can be read out optically and efficiently due to the spin dependent fluorescence as discussed in Sec. 1.2. To experimentally achieve the most efficient detection, it is essential to analyze the transient fluorescence after illuminating a spin-polarized NV center with a laser (see Fig. 1.5 (b)). The NV is first initialized into the $m_s = 0$ state with a laser pulse and after a waiting time, which allows population in the singlet state to decay to the ground state (see Fig. 1.2 (a)), a second laser pulse is applied while the the NV fluorescence is read out (see Fig. 1.5 (a)). For analyzing the fluorescence rates from the $m_s = 1$ state, a MW π-pulse (a pulse which induces a spin flip) is applied before the readout.

The resulting fluorescence is depicted in Fig. 1.5 (b) for the different initial spin states. The efficiency of a single measurement with a readout-duration of τ_{Read} is described by the SNR. The signal S is defined as the difference between the fluorescence photons from the different spin states $(S = \int_0^{\tau_{\text{Read}}} I_{m_s=0}(\tau) - I_{m_s=1}(\tau)d\tau)$. The noise N, for an NV center, is dominated by photon shot noise $(N = \int_0^{\tau_{\text{Read}}} \sqrt{0.5(I_{m_s=1}(\tau) + I_{m_s=0}(\tau))}d\tau)$. From the transient fluorescence measurement the SNR of a single read out for a given readout duration τ_{Read} can be determined using

$$\text{SNR}(\tau_{\text{Read}}) = \frac{\int_0^{\tau_{\text{Read}}} I_{m_s=0}(\tau) - I_{m_s=1}(\tau)d\tau}{\int_0^{\tau_{\text{Read}}} \sqrt{0.5(I_{m_s=1}(\tau) + I_{m_s=0}(\tau))}d\tau}. \tag{1.24}$$

The blue curve in Fig. 1.5 (b) depicts the SNR for various τ_{Read}, which allows to determine the optimal readout duration τ_{opt} for achieving a maximum SNR. Note that the SNR depends on the NV center and on the laser power. For the depicted measurement with a laser excitation of $\sim 100\,\mu$W (excitation through an objective with $NA = 0.8$ and the NV located in a scanning probe) the optimal duration is $\tau_{\text{opt}} = 500\,$ns which results in a SNR of 6%. Within a time window of $\sim 1\,$ms, a single readout (typical duration of $\sim 1 - 10\,\mu$s) can be repeated $100 - 1000$ times, which
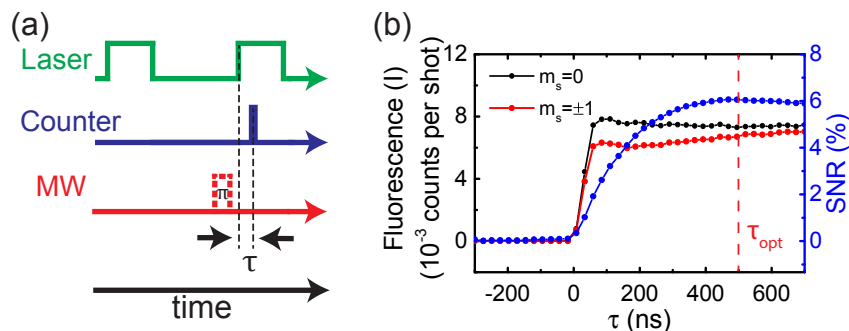
Figure 1.5: (a) Pulse sequence for measuring the transient NV fluorescence. The sequence consists of an initialization laser pulse and a readout of the spin state (laser pulse combined with a counter measuring the fluorescence intensity for 25 ns). For measuring the $m_s = \pm 1$ fluorescence an additional π pulse is added before the read out. (b) Transient fluorescence after laser illumination for the $m_s = 0$ (black) and the $m_s = \pm 1$ spin state (red). The optimal readout length τ_{opt} is determined by the signal-to-noise ratio of the data (blue). For $\tau_{\text{opt}} = 500$ ns the SNR approaches 6% for the depicted NV center in scanning probes.

enables spin state determination (SNR $= 1$) and thereby the efficient evaluation of magnetic fields.

1.6.4 Rabi oscillations

A MW magnetic field induces Rabi oscillations between two ground states as derived in Sec. 1.6.1. Such Rabi oscillations can be used to sense arbitrary MW magnetic fields. To address only one subset of the ground state triplet, a DC magnetic field is applied to induce a Zeeman splitting between the $m_s = \pm 1$ states. If this DC field is large compared to the applied MW magnetic field, the $m_s = \pm 1$ states form isolated two-level systems. Selection rules impose that the subsets with ($\Delta m_s = \pm 1$) can only be driven by the right or left handed circular MW field ($B_{\text{MW}}^{\pm}$). An arbitrarily polarized MW field resonant with one subset therefore leads to oscillations of the population between the two involved spin states, at a frequency $\Omega = 2\pi \gamma_{\text{NV}} B_{\text{MW}}^{\pm}$, where $B_{\text{MW}}^{\pm}$ is the corresponding circularly polarized component of the MW field in a plane perpendicular to the NV axis. The measurement sequence to measure Rabi oscillations consists of an initialization into the $m_s = 0$ state, a MW magnetic field pulse of variable duration τ, and spin readout, as illustrated in Fig. 1.6 (a). By varying the MW pulse duration, the oscillations in the spin state population can be measured optically, as depicted in Fig. 1.6 (c).

In addition to the mathematical description introduced in Sec. 1.6.1, Rabi oscillations can be illustrated on the Bloch sphere in the rotating frame. The south and north poles of the Bloch sphere represent a subset of the NV center ground states, i.e.
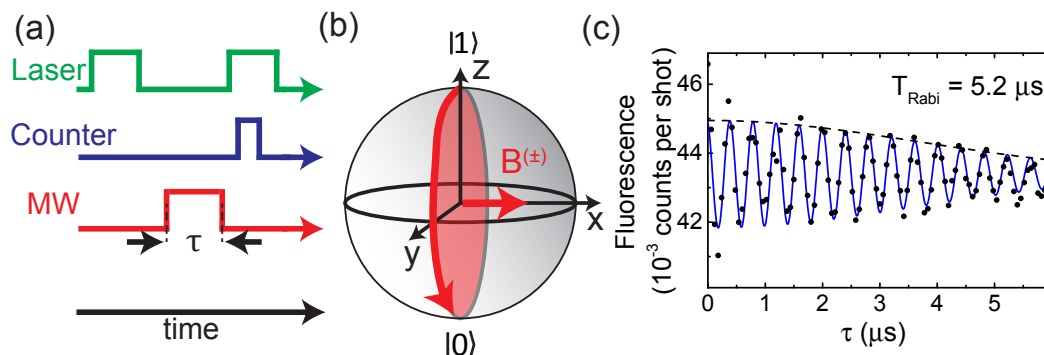
Figure 1.6: (a) Pulse sequence for measuring Rabi oscillations. Between initialization and readout ($\tau_\mathrm{read} = 300\,\mathrm{ns}$), a MW pulse of varying duration τ is applied. (b) Bloch sphere representation of Rabi oscillations. The MW magnetic field $B_\mathrm{MW}^{\pm}$ acts as an effective magnetic field along the x-axis of the Bloch sphere in the rotating frame (see main text) and induces a Larmor procession. This precession is mapped onto the spin state population and is read out optically. (c) Rabi oscillations. The fit (described in more detail in Appendix B) is depicted in blue and yields a decay time of $T_\mathrm{Rabi} = 5.2\,\mu\mathrm{s}$. (data taken from [17])

the $m_s = 0$ and $m_s = \pm 1$. The rotating frame rotates with a frequency ω around the two level system's quantization axis. In this rotating frame, a resonant MW magnetic field can be seen as an effective DC magnetic field $B_\mathrm{MW}^{\pm}$, that is aligned along the x-axis of this sphere. This will lead to a precession of the spin, with a frequency given by the Larmor frequency $\Omega = 2\pi\gamma_\mathrm{NV}B_\mathrm{MW}^{\pm}$, around this effective field as indicated in Fig. 1.6 (b). When reading out the spin state, we therefore obtain Rabi oscillations, with a frequency proportional to the applied MW magnetic field, as depicted in Fig. 1.6 (c). The measured Rabi signal additionally exhibits a decay constant T_Rabi, that depends on the spin environment and the driving conditions (see Appendix B). From the determined $T_\mathrm{Rabi} = 5.2\,\mu\mathrm{s}$, we obtain a maximal achievable sensitivity of $800\,\mathrm{nT}/\sqrt{\mathrm{Hz}}$ (see Appendix B for details on the determination).

In Chap. 4, we employ this method of measuring the MW magnetic field by evaluating the Rabi frequency and use it to demonstrate the first proof-of-concept nanoscale MW imaging experiment on a prototypical MW device.

1.6.5 Ramsey interferometry

Ramsey interferometry can be applied to sensitively evaluate DC-magnetic fields. A pulse sequence, as depicted in Fig. 1.7 (a), is applied to evaluate the free Larmor precession and measure the magnetic field.
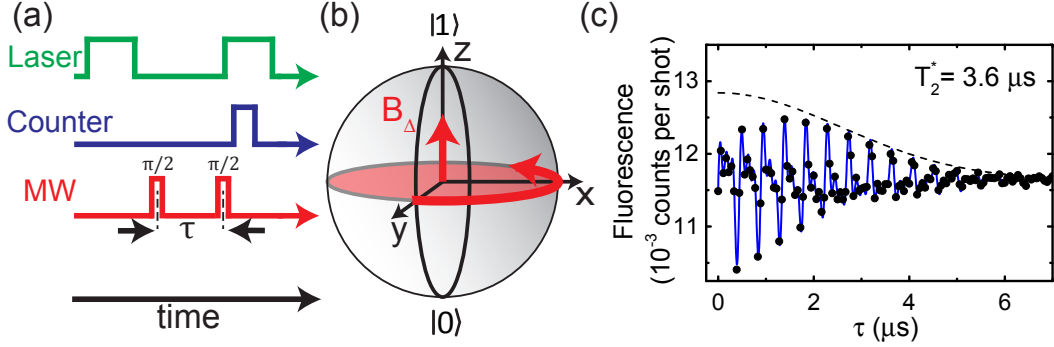
Figure 1.7: (a) Pulse sequence for Ramsey interferometry. Between the initialization and the readout ($\tau_{\mathrm{read}} = 300\,\mathrm{ns}$), a MW $\pi/2$ pulse creates a superposition state on the equator of the Bloch sphere that acquires a phase during the free precession time. This phase is mapped onto a population difference using a second MW $\pi/2$ pulse and is finally read out optically. (b) The accumulation of a phase can be described by a Larmor precession around an effective magnetic field B_Δ on the Bloch sphere, which is given by the detuning of the MW magnetic field pulses. (c) Measured Ramsey signal. The envelope is fitted by a typical signal (described in more detail in Appendix B) which yields $T_2^* = 3.6\,\mu\mathrm{s}$ (data taken from [50]).

The process of Ramsey interferometry is illustrated in Fig. 1.7 (b) in the rotating frame on the Bloch sphere. By applying a MW $\pi/2$ pulse a superposition state on the equator can be generated

$$\psi_s = \frac{1}{\sqrt{2}}(|0\rangle + e^{i\phi}|1\rangle). \tag{1.25}$$

MW magnetic fields with a detuning Δf_{MW} from the transition frequency will generate states on the equator, which in the rotating frame are precessing around the quantization axis. This rotation can be interpreted as a Larmor precession around an effective magnetic field B_Δ, which can mathematically be described by an accumulation of a phase

$$\phi = 2\pi\Delta f_{\mathrm{MW}}\tau = 2\pi\gamma_{\mathrm{NV}}\int_0^\tau B_\Delta(t)dt, \tag{1.26}$$

where τ is the duration of free spin precession. A second $\pi/2$ MW pulse acts as a rotation of $\pi/2$ around the x axis in the rotating frame and therefore maps the accumulated phase onto a population difference, which can be read out optically.

For probing DC magnetic fields $B_{\mathrm{DC}}^{\mathrm{probe}}$, the MW frequency is set to a known reference detuning, i.e. a detuning in the absence of $B_{\mathrm{DC}}^{\mathrm{probe}}$, which corresponds to a known magnetic field B_Δ^{ref}. In the presence of the probe DC field the effective field is given by $B_\Delta = B_\Delta^{\mathrm{ref}} + B_{\mathrm{DC}}^{\mathrm{probe}}$. When sweeping τ for an ideal two level system, oscillations with a magnetic field dependent frequency $\omega_\Delta = 2\pi\gamma_{NV}B_\Delta$ can

19

be observed, which allow one to determine the probe field $B_{\mathrm{DC}}^{\mathrm{probe}}$. In reality, however, the NV center spin is coupled to the nuclear spin of its ^{14}N atom (or ^{15}N atom depending on the isotope) by hyperfine interaction, which results in a splitting of the $m_s = \pm 1$ state into three (two for ^{15}N) sub-levels which are separated by 2.2 MHz ($\approx 4\,\mathrm{MHz}$) [35]. Therefore, the resulting Ramsey signal exhibits beat notes, comprised of oscillations of three (two) different frequencies as depicted in Fig. 1.7 (c). Additionally, the signal exhibits a damping due to environmental spin impurities, which is characterized by the dephasing time T_2^*. By fitting the signal consisting of three frequencies and a decay as described in Appendix B, the corresponding magnetic field and dephasing time T_2^* can be evaluated. For the depicted measurement the fit yields $T_2^* = 3.6\,\mu\mathrm{s}$ which results in a sensitivity of $500\,\mathrm{nT}/\sqrt{\mathrm{Hz}}$ (see Appendix B for the details on the determination).

1.6.6 Spin Echo spectroscopy

Spin Echo spectroscopy, which is also referred to as Hahn Echo, can be applied to improve sensitivity and evaluate oscillating magnetic fields. The pulse sequence for this corresponds to a Ramsey sequence with a π-pulse inserted in the middle of the free evolution time (see Fig. 1.8 (a)).
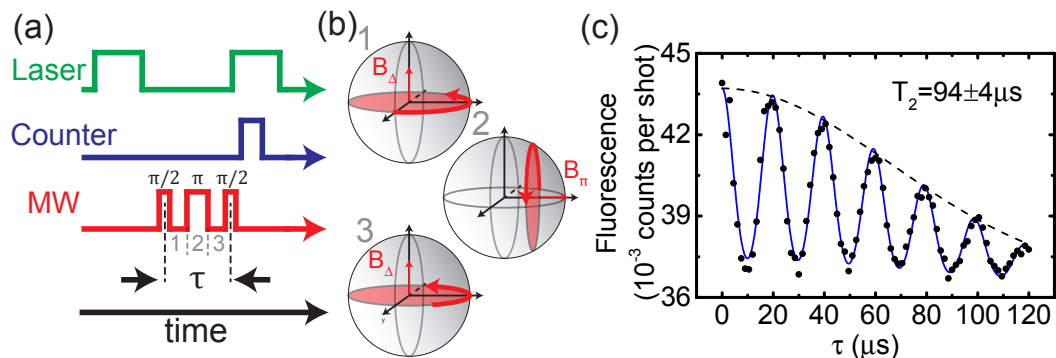
Figure 1.8: (a) Pulse sequence for Spin Echo spectroscopy. A π-pulse is inserted in the middle of the free evolution time τ. (b) Bloch sphere representation of Spin Echo spectroscopy. The π-pulse (2) leads to a cancellation of the phase accumulated due to DC magnetic fields in the first free precession time (1) and the second free precession time (3) and the resulting measurement is insensitive to low frequency magnetic fields (see main text). (c) Measured Spin Echo signal. The envelope is fitted to the characteristic decay (described in more detail in Appendix B), which yields a decay time of $T_2 = 94 \pm 4\,\mu\mathrm{s}$ (data taken from [16]).

Because of the π-pulse the measurement is insensitive to slowly varying magnetic fields, which can be seen in the overall accumulated phase of the Spin Echo pulse sequence of

$$\phi = 2\pi\gamma_{NV}\left[\int_0^{\tau/2} B_\Delta(t)dt - \int_{\tau/2}^\tau B_\Delta(t)dt\right]. \qquad (1.27)$$

The phase accumulated during the first free precession time (1) will cancel with the phase accumulated during the second free precession time (3) and the final superposition state is insensitive to a static B_Δ (independent of the angle of the rotation in the first and third interval in Fig. 1.8 (b)). Hence, the Spin Echo signal is insensitive to static magnetic fields and has a maximum sensitivity at the frequency $f = 1/\tau$ (see Eq. 1.27 and Appendix. A). For the perfect two level system in a DC magnetic field (no AC magnetic field), we expect the signal to decay due to the environmental field fluctuations. However, the typical signal for the NV center consists of revivals (see Fig. 1.8 (c)), which are a prominent Electron Spin Echo Envelope Modulation (ESEEM) [51]. These revivals are caused by the Larmor precession of the ^{13}C spin bath. Each ^{13}C isotope possesses a spin $1/2$, which leads to a magnetic field at the NV center. In an external DC-magnetic field B, the ^{13}C start to precess with a Larmor frequency $f_{\text{Larmor}} = g_n\mu_n B$, where $g_n\mu_n = 1.071\,\text{kHz/G}$. This results in an AC-magnetic field at the NV center. If half of the evolution time τ in the Spin Echo measurement is equal to a multiple of the Larmor period, T_{Larmor}, the NV center phase collected due to the AC-magnetic field of the ^{13}C spin bath is $\phi = 0$. Hence, only when this condition is fulfilled the NV center is insensitive to the AC field of the ^{13}C spin bath and the signal is maximal. This explains the observed revivals.

In the presence of an external AC field B_{AC} at a frequency $f = 1/\tau$, the Spin Echo signal additionally exhibits oscillations at a frequency $\omega_{\text{AC}} = 2\pi\gamma_{\text{NV}}B_{\text{AC}}$. Measuring these oscillation therefore allows one to quantitatively evaluate B_{AC}. Because of the longer coherence time of $T_2 = 94\,\mu\text{s}$ (compared to the dephasing time $T_2^* = 3.6\,\mu\text{s}$) a sensitivity of $28\,\text{nT}/\sqrt{\text{Hz}}$ can be achieved (see Appendix B for details on the determination), making Spin Echo spectroscopy an efficient tool to probe AC magnetic fields.

1.7 Summary of sensing schemes

This chapter introduced the extraordinary properties of the NV center and how they can be exploited for magnetic field sensing. When operated in the various sensing schemes, the NV center can be applied to sensitively study magnetic fields at various frequencies, which allows to analyze various phenomena in solid state physics (see Chap. 5).

The frequency range covered by a particular sensing scheme can be described by a weighting function, which describes the weighted signal at a particular frequency (see Appendix A). The weighting functions are depicted in Fig. 1.9 for the different sensing schemes. While Ramsey interferometry is mostly sensitive at low frequencies, Spin Echo is sensitive at MHz-frequencies and can be tuned by the evolution time.
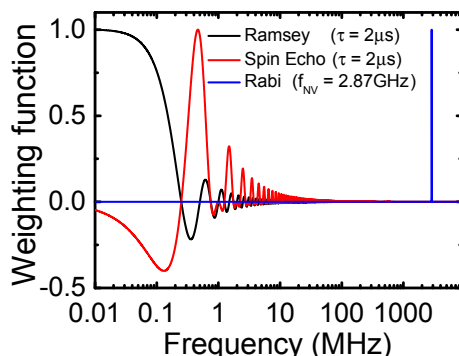
Figure 1.9: Normalized frequency domain weighting function for the different sensing schemes illustrating the different operation ranges. The function describes the weighted signal at a particular frequency when measured with the different sensing scheme (see Appendix A). Note that the weighting function depends on the phase of the investigated magnetic field in respect to the pulse sequence. The weighting function of the Ramsey and Spin Echo depends on the evolution time τ which was set to $2\,\mu$s. Rabi oscillations are sensitive at the NV transition frequency which can be tuned by an applied DC magnetic field and was set to the zero field splitting of $f_{\mathrm{NV}} = 2.87\,$GHz.

Rabi oscillations are sensitive at the transition frequency of the NV center, which allows to study magnetic fields in the GHz range. As the transition frequency can be tuned, Rabi oscillation can also be applied for studying fields from MHz to $\sim 20\,$GHz by applying DC magnetic fields along the NV symmetry axis [52].

Besides the addressable frequency range the major figure of merit of a magnetic field sensor is the sensitivity η, which can be described by the general formula [38]:

$$\eta \sim \frac{1}{\gamma_{\mathrm{NV}}} \frac{1}{C\sqrt{I}} \frac{1}{\sqrt{T_{\mathrm{Coh}}}}, \tag{1.28}$$

where I is the detected fluorescence rate, C the contrast and T_{Coh} the coherence time measured with a particular sensing scheme. Hence, these parameters limit the sensitivity and several methods have been developed to increase the detected fluorescence rate or extend the coherence time [38]. In Chap. 2, we discuss some of these routes that can be applied to optimize these parameters for single NV centers in the presented scanning probe geometry and thereby improve the sensitivity of our all diamond scanning probes.

In Table 1.1, we summarize the coherence times T_{Coh} and the sensitivities of the different sensing schemes reached in this work with shallowly implanted NV centers. Note that the decay time of the Rabi oscillations T_{Rabi} depends on the MW driving conditions (see Appendix B) and we here refer to our experimentally measured T_{Rabi}. The long coherence times T_{Coh} of single NV centers together with their optical properties yield sensitivities ranging from $\eta_{\mathrm{ESR}} = 4\,\mu\mathrm{T}/\sqrt{\mathrm{Hz}}$ to $\eta_{\mathrm{Spin\,Echo}} = 28\,\mathrm{nT}/\sqrt{\mathrm{Hz}}$.

This excellent sensitivity enables the precise evaluation of magnetic fields. Using a NV center embedded in scanning probes the magnetic stray field of a single electron was imaged [2], which demonstrates the performance of NV centers.

Table 1.1:   Overview of the coherence times and sensitivities of the different sensing techniques presented here, combined with the typical frequency range of sensing. Note that Rabi oscillations are sensitive to magnetic fields at the transition frequency of the NV center. Using DC magnetic fields this transition frequency can be shifted, which allows to use Rabi oscillations to study magnetic fields from MHz up to several GHz.

NMR technique	NV depth	T_{Coh}	η	Frequency range
ESR	$9\,\mathrm{nm}$		$4\,\mu\mathrm{T}/\sqrt{\mathrm{Hz}}$	DC
Ramsey	$17\,\mathrm{nm}$	$T_2^* = 3.6\mu\mathrm{s}$	$500\,\mathrm{nT}/\sqrt{\mathrm{Hz}}$	DC
Spin Echo	$9\,\mathrm{nm}$	$T_2 = 94\,\mu\mathrm{s}$	$28\,\mathrm{nT}/\sqrt{\mathrm{Hz}}$	$0.1-1\,\mathrm{MHz}$
Rabi Oscillation	$9\,\mathrm{nm}$	$T_{\mathrm{Rabi}} = 5.2\,\mu\mathrm{s}$	$800\,\mathrm{nT}/\sqrt{\mathrm{Hz}}$	MHz-20GHz

In conclusion, the NV center forms an atomically sized, highly sensitive magnetic field sensor. Operated with the different sensing schemes, it can be applied to measure magnetic fields from DC to several GHz with a sensitivity reaching $\eta = 28\,\mathrm{nT}/\sqrt{\mathrm{Hz}}$. In contrast to other quantum sensors such as molecules and quantum dots, these magnetic sensing capabilities are sustained from cryogenic temperatures up to $550\,\mathrm{K}$, allowing sensitive magnetic field evaluation even in ambient conditions. Its broad operation range makes the NV center an ideal sensor with applications ranging from mesoscopic physics to material science and biology.

Chapter 2

Scanning NV Magnetometry

To harness the full potential of NV centers for measuring magnetic fields with nanoscale spatial resolution, a close proximity of the NV center and the sample has to be ensured. This can be achieved by placing the sample directly onto the diamond surface, which allows to sensitively detect and image its magnetic field using wide-field microscopy [53, 54, 55]. The resolution these techniques offer is limited by the optical diffraction limit, which can be overcome by scanning a targeted sample that is attached to an atomic force microscopy (AFM) tip with respect to the diamond surface. Thus, sensitive, high resolution stray field imaging can be performed [56, 57]. However, only very specific targets can be attached to an AFM tip, which limits the applicability of this approach. In contrast, NV centers attached to an AFM tip enable sensitive, high resolution, imaging of the local magnetic environment emanating from arbitrary samples. This approach may find applications in different research fields ranging from material science to biology and quantum technologies.

Triggered by this multitude of possible applications, various approaches to bring a scanable NV center in close proximity to a sample were recently developed. The first experiments in scanning NV magnetometry employed nanodiamonds (NDs) grafted to AFM tips (see Fig. 2.1 (c)) [58, 21, 38, 23]. However, NVs in NDs suffer from short coherence times limiting their sensitivity for magnetic sensing. Moreover, efficient light collection from NDs on scanning probe tips is difficult and limits the resulting sensitivities. Lastly, it has proven challenging to ensure small NV-to-sample distances using this approach. Most published work on NDs reports scanning distances of $\gtrsim 100$ nm from the sample surface, which limits the spatial resolution of the scanning probe images. Additionally, the fluorescence of NV centers in single digit NDs is typically unstable without further surface treatment [59]. Motivated by these drawbacks, a novel approach using all-diamond, single crystalline AFM tips has recently been demonstrated (see Fig. 2.1 (b)) [20]. This approach relies on fabricating all-diamond scanning probes with the NV center placed close to the apex of a scanning diamond nanopillar. Aside from achieving close proximity of the NV center to the sample, the pillar's light guiding properties enhance the collection
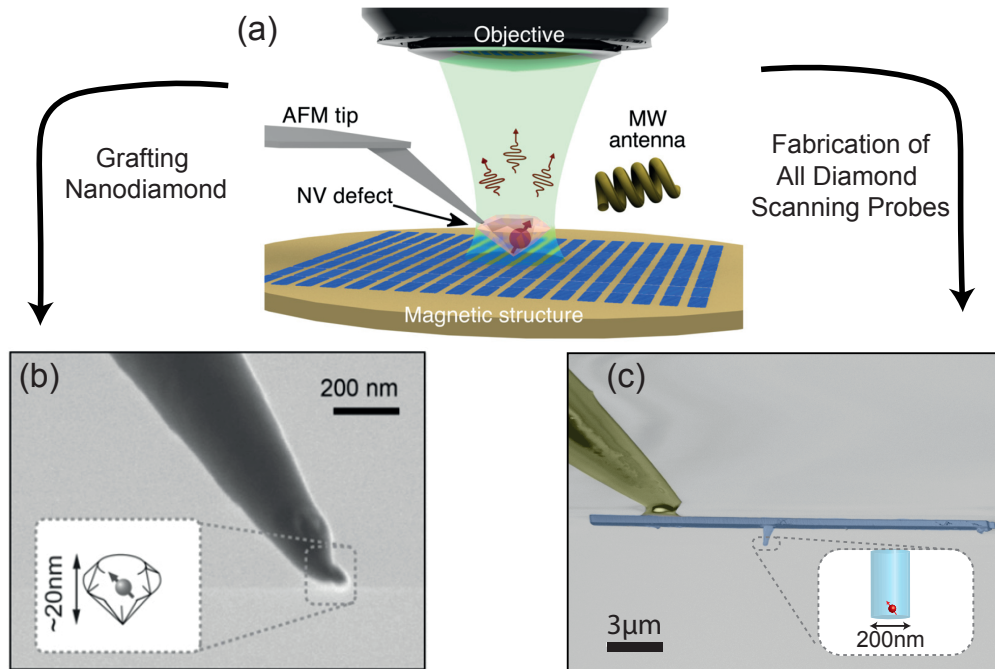
Figure 2.1: (a) Principle of scanning NV magnetometry which combines an atomic force microscope (AFM) and a confocal microscope (CFM). The AFM tip is functionalized with a single NV center. The confocal microscope is equipped with a microwave (MW) antenna to perform optical detection of the NV center ESR transition. Reprinted from [21], with the permission of AIP Publishing. (b) The NV center is hosted in a diamond nanocrystal grafted at the end of an AFM tip. Figure reprinted from [38], © IOP Publishing. Reproduced with permission. All rights reserved. (c) All diamond scanning probe with a single NV center placed at the apex of the tip.

efficiency for the NV fluorescence. Furthermore, the devices can be sculpted out of high purity diamond, which enables long NV spin coherence times. These properties (photo-stability, spin coherence and efficient light collection) make the NV center containing all diamond scanning probes excellent sensors for probing magnetic fields on the nanoscale.

In this chapter, we describe the implementation and performance of our scanning NV magnetometer based on all-diamond scanning probes. We introduce our magnetometry setup, which consists of a confocal microscope to read out the NV fluorescence and a tuning fork-based AFM, which enables a controlled scanning of the NV center in close proximity to the sample. In Section 2.2 we focus on the key component of our setup: the all-diamond scanning probes. We present the nanofabrication of diamond nanopillars for scanning probe microscopy, discuss their characteristics and show a highly efficient and robust approach for integrating these

devices into our AFM. Finally, we demonstrate the magnetometry performance by presenting two imaging modes, which we apply for high resolution imaging of the stray field of single magnetic Ni nanorods. We conclude with the state-of-the-art sensitivity and resolution and illustrate routes to improve the performance of scanning NV-magnetometry.

2.1 Experimental setup

Scanning NV-magnetometry combines two established techniques: AFM and confocal fluorescence microscopy (CFM). The magnetic field of a sample can be evaluated and imaged by detecting the spin dependent fluorescence of the NV center while the NV center is scanned in close proximity to a sample via AFM feedback.
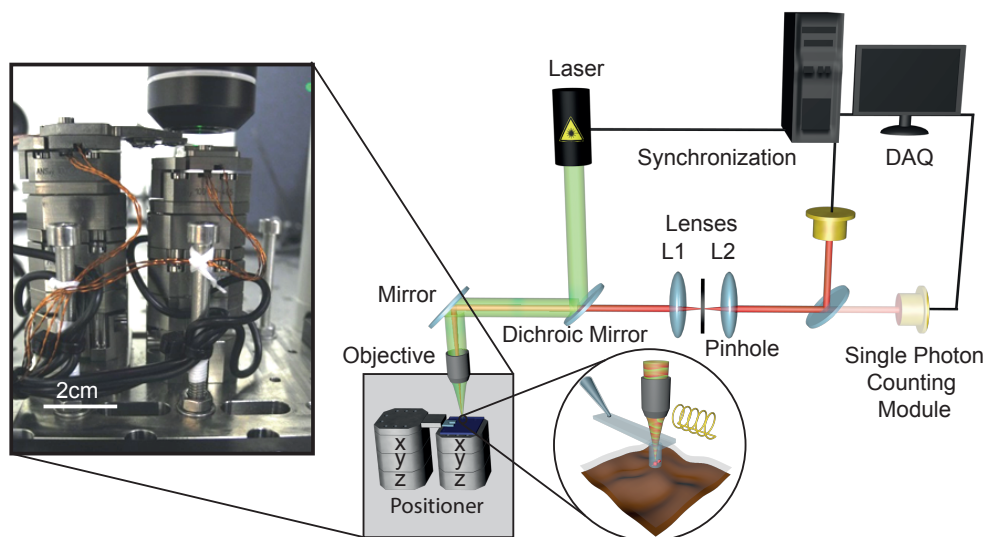
Figure 2.2: Schematic of the scanning NV setup consisting of an AFM and a CFM. A green (532 nm) laser excites the NV center and the red fluorescence is collected via a single photon counting module, which is read out by a computer. A second single photon counting module can be used in a Hanbury Brown-Twiss geometry for performing second order autocorrelation measurements to determine if a single NV center is observed. The setup is furthermore equipped with MW electronics to drive the NV center ground state transitions (not depicted). Electronics for applying different pulse sequences and synchronizing laser, MW excitation and detection counter are used to operate the NV in the different sensing schemes. The AFM consists of two positioners (attocube ANPx101, ANPz101, ANSxyz100). One positioner is used to place the NV in the focus of the CFM (see inset) and the second is used to scan the sample, while fluorescence of the NV is continuously monitored.

To collect the NV center fluorescence, we use a free-space, homebuilt confocal microscope as depicted in Fig. 2.2 [32]. A 532 nm laser (Laser Quantum, Gem 532) off resonantly excites the NV center and the emitted fluorescence intensity is detected by single photon counting modules (Excelitas, SPCM-AQRH-13). To filter the red fluorescence from the excitation, a dichroic mirror (Semrock, LM01-552-25) and a bandpass filter (Thorlabs, FEL-0550) are employed to suppress the excitation light. A pinhole ($50\,\mu m - 100\,\mu m$) in between two lenses (Thorlabs, L1: AC254-075-B-ML and L2: AC254-100-B-ML) act as spatial filter for CFM operation (i.e. to block light emitted outside the optical focus). This enhances optical resolution and signal to background ratio of the optical signal. The Olympus MPLFLN100X objective with a numerical aperture (NA) of 0.8 and a working distance of 3.4 mm offers an ideal tradeoff between efficient light collection and long working distance. To control the NV spin state, the microscope is equipped with a microwave antenna to drive the ground state spin transitions. A programmable TTL pulse generator (Spincore, PulseBlasterESR-PRO 500) is employed to synchronize microwave and laser excitation with the fluorescence readout. This is used to apply different pulse sequences required for Rabi, Ramsey or Spin-Echo experiments. Additionally, the setup is also equipped with a second single photon counting module in a Hanbury Brown-Twiss geometry with correlation electronics to perform second order autocorrelation ($g^{(2)}$) measurements to identify single NV centers (see Sec. 2.2.5).

A tuning fork (TF) based AFM is used to ensure close proximity between the sample and the NV center [60, 61]. We mechanically excite the TF via a piezo actuator (PI-ceramics, PIC255) and detect the resonance oscillation amplitude (phase) by reading out the resulting piezoelectric signal using a charge amplifier (Femto, HQA-15M-10T) and an SPM controller (Attocube, ASC500) [62]. When the sample approaches the AFM tip that is attached to one prong of the TF, short range forces, such as Van-der-Waals forces, result in a damping that lead to a decrease of the amplitude and a shift in the phase of the TF. This decrease of the TF amplitude (shift of the resonance) can be used to control the distance between the sample and the tip via a feedback loop [60, 61]. Thus, robust scanning in close proximity to the sample can be achieved.

2.2 Fabrication of all-diamond scanning probes

The key component of the scanning NV-magnetometer is an all-diamond scanning probe with an NV center placed close to the apex of a diamond nanopillar. Here, we describe an optimized procedure to fabricate such single-crystal, all-diamond scanning probes, which was developed during this work and is published in Ref. [16]. In particular, we present in detail the nanofabrication of diamond nanopillars for scanning probe microscopy and describe a highly efficient and robust approach for integrating these devices into our AFM/CFM system.

The fabrication procedure that we describe here consists of 6 steps: We start with commercially available, high purity diamond plates (50 μm thick, Sec. 2.2.1),

in which we create shallow NV centers using ion implantation (Sec. 2.2.2). Our all diamond scanning probes consist of a cylindrical nanopillar (200 nm diameter, 1.5 μm height) on a < 1 μm thick cantilever. Thus, it is essential to thin down the commercially available plates to a suitable thickness (Sec. 2.2.3). The thinned membranes are subject to two consecutive lithography and plasma etching steps to form the pillars and the cantilevers (Sec. 2.2.4). In the subsequent step, we identify the scanning probes that contain single NV centers (Sec. 2.2.5). Finally, we mount the selected scanning probes on a tuning fork based AFM head (Sec. 2.2.6).

2.2.1   Diamond material and initial sample preparation

Our nanofabrication procedure for the all-diamond scanning probe devices is based on commercially available, high purity, synthetic diamond grown by chemical vapor deposition (Element Six, electronic grade, [N]^s<5 ppb, [B]<1 ppb) [63]. The 500 μm thick diamonds are processed into 30-100 μm thick diamond plates by laser cutting and subsequent polishing (Delaware Diamond Knives, USA or Almax Easy Lab, Belgium [64]). While our process can be applied to a large range of thicknesses, we found 50 μm thick plates to form the best compromise between mechanical stability, ease of handling and reasonable processing times (see Sec. 2.2.3).

The surface roughness of the initial diamond plates is typically 0.7 nm, as evidenced by AFM imaging (Fig. 2.4 (d)), and the plates have a wedge of typically several micrometers across its lateral dimensions of 4 mm. We note that such a high quality polish is mandatory for the subsequent processing steps. Initially, we clean the plates using a boiling tri-acid mixture (1:1:1 sulfuric acid, perchloric acid, nitric acid, boiled until it reverts to clear appearance) to remove any surface contamination that might have resulted from polishing [65, 66]. Lastly, the sample is cleaned in solvents (deionized water, acetone, ethanol, isopropanol) to remove possible contaminants present in the acids.

Mechanical polishing of diamond is known to introduce crystal damage below the polished surface into a depth of up to several micrometers [67, 68, 69]. The lattice in this damaged layer can be deformed and defective: cathodoluminescence (CL) measurements indicate a high concentration of defects [67] and etching away 3-4 μm of diamond almost recovers the CL of pristine diamond. NVs in this damaged layer might therefore suffer from an unstable charge state or spin decoherence due to trapped paramagnetic defects or fluctuating charges. Furthermore, strain in the damaged layer might render the NV spins insensitive to magnetic fields in first order and therefore useless for magnetometry [38]. To circumvent these potential obstacles, we remove ≈ 3 μm or more of the damaged surface layer using inductively coupled reactive ion etching (ICP-RIE) as described in the following.

For all etch steps, the diamond plates are mounted on Si chips (1 cm squares) as carriers; we perform plasma etching using a Sentech SI 500 ICP-RIE apparatus. We initiate the etching by removing roughly the first micrometer of diamond using an

$ArCl_2$ plasma step[1]. This plasma chemistry has been reported to remove damaged diamond layers without roughening the surface [68]. Note that even slight surface roughening would be detrimental for all subsequent processes. We summarize the plasma parameters used as well as the resulting etch rates (as determined by an in-situ laser interferometer, SenTech SLI 670) in table 2.1.

While enabling optimal etching of defective diamond, the $ArCl_2$ plasma also strongly erodes Si carrier wafers routinely used in ICP-RIE processes. The resulting high level of Si contamination introduces a roughening of the diamond surface. To avoid this, we employ a ceramics based carrier system which we find to be more resistant to etching in the $ArCl_2$ plasma consequently avoiding contamination. Diamond surfaces prepared by $ArCl_2$ plasma have been suspected to contain Cl_2 [70], which might deteriorate the NV spin properties. As a consequence, we terminate etching using an O_2 plasma to remove any such potential Cl_2 contamination (see table 2.1).

Table 2.1: Plasma parameters for the nano-fabrication procedure. Note that the ArO_2 plasma is used to etch the nanopillar structures, while the other plasma types are used for the 'deep etches' to remove polishing damage and form the thin membrane. The nanopillar etching is carried out using a (6 Inch) silicon carrier inside the reactor, while all other etches are performed using a ceramics carrier (96% Al_2O_3) to avoid silicon contamination. The plasma bias voltage was stable within roughly 10% for runs performed within a time-span of several weeks.

plasma	ICP power [W]	RF power/bias [W]/[V]	flux [sccm]	Pressure [Pa]	Etch rate [nm/min]
$ArCl_2$	400	100/220	Ar 25; Cl_2 40	1	60
O_2	700	50/120	O_2 60	1.3	150
ArO_2	500	200/120	Ar 50; O_2 50	0.5	150

2.2.2   Creation of NV color centers

To realize high-resolution imaging, it is mandatory to achieve close proximity between NV spin and sample, which implies the creation of NV centers close to the diamond surface. To create such a shallow layer of NV centers, we implant the etched diamond surface with ^{14}N ions at an energy of 6 keV and a dose of 3×10^{11} cm^{-2} (at "Ion beam services", France). The estimated resulting stopping depth of the ^{14}N ions in diamond is 9 ± 4 nm according to numerical simulations [71]. We anneal the sample in vacuum (chamber base pressure: 3-4 $\times 10^{-7}$ mbar) partly following the recipe from Ref. [72]. The heating device is a boron nitride plate, electrically heated via buried graphite strips (Tectra, Boralectric HTR-1001). The temperature of the oven is calibrated using a comparison between pyrometer measurements and

---

[1]Recent etching recipies revealed that such long $ArCl_2$ etch is not required

a thermocouple (tungsten/rhenium) inserted into a bore hole in the heater plate. We use the following sequence of annealing steps: ramp from room temperature to 400°C in 1 h, hold at 400°C for 4 h, ramp to 800°C in 1 h, hold at 800°C for 2 h, cool down. We also investigated the effect of a high temperature annealing step at 1200°C (ramp from 800°C to 1200°C in 1 h, hold at 1200°C for 2 h) according to Ref. [72]. However, we did not find any significant effect on the NV yield or the NV spin coherence properties. With the previously described procedure, we create a layer of NV centers with a density of $2.6 \times 10^9 \, \mathrm{cm}^{-2}$ (see Sec. 2.2.5). From this, we estimate the yield of the NV creation to be $0.9\,\%$ which is comparable to previously reported values [73].

2.2.3   Deep etching to form diamond membranes

We now introduce an etching process leading to a thinned membrane of several micron thickness and $\sim 400 \times 400 \, \mu$m size, supported by the surrounding 50 μm thick diamond plate. Typical etch masks with sub-micron thickness would not withstand the long etching process necessary to thin a 50 μm thick diamond plate down to a few microns. Thus, we employ thin quartz cover slips (SPI supplies, 75-125 μm thick) as etch masks. Using water jet cutting (Microwater Jet, Switzerland) a slot ($\leq 500 \, \mu$m width) is cut into the cover slip. The sample is then sandwiched between a Si carrier chip and the mask; the latter is fixed onto the 6 inch carrier wafer using vacuum grease (see Fig. 2.3 (a)). The etch resistance of the quartz material allows for a high quality etching, whereas using standard glass cover slips leads to micro-masking and roughening of the etched diamond as a result of low etch resistance. The masks can be reused several times.
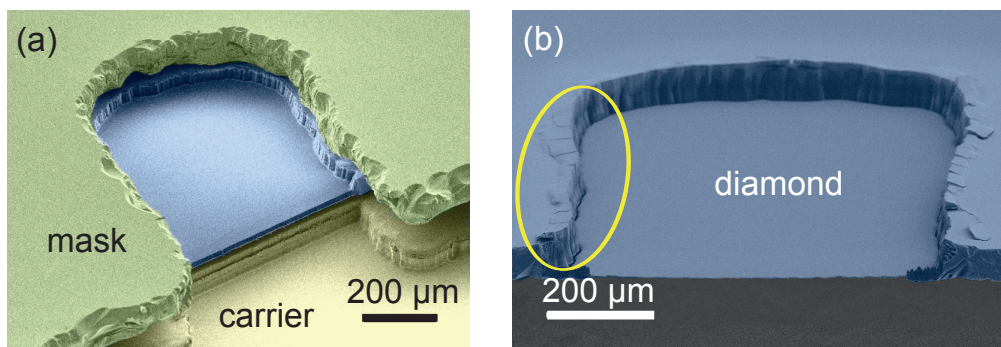
Figure 2.3: (a) False-colored scanning electron microscopy (SEM) image of a diamond plate (blue) sandwiched between a quartz cover slip (green) and a Si carrier (yellow). (b) Thin diamond membrane etched in one run.

For the membrane 'deep etch', we use an $\mathrm{ArCl_2}$ and an $\mathrm{O_2}$ based plasma, with plasma parameters as summarized in table 2.1. The etching process starts with 5 mins of $\mathrm{ArCl_2}$ plasma, then the following sequence is cycled until the desired etch

depth is reached: 5 mins $ArCl_2$, 5 mins O_2, 5 mins O_2. Consecutive etch steps were separated by 5 mins of cooling under Ar (100 sccm, 13.2 Pa). In the ICP-RIE plasma, a trench forms close to the edge of the quartz mask and the sidewalls of the pit etched into the diamond plate, see yellow marker in Fig. 2.3 (b). As the depth of this trench can exceed 1 μm during our deep etch, the thinned membrane becomes mechanically unstable as its connection to the thick diamond plate is compromised. The formation of the trench can be explained as follows: the reflection of high energy ions impinging under grazing incidence onto the sidewalls of the mask and the already etched pit leads to a focusing of the ions close to the sidewalls of the pit and a locally enhanced etch rate induces the trench [74]. To ensure membrane stability, we exchange the initial etch mask (mostly 400-500 μm etched area) by a narrower mask (300-400 μm) when the membrane has reached a thickness of about 8-10 μm. Due to the shifted mask edge, the trench formation restarts at the new mask edge location (see e.g. Fig. 2.5 (b), right side). The trench formed during the residual etching does not destabilize the membrane. Due to the thick etch mask, we
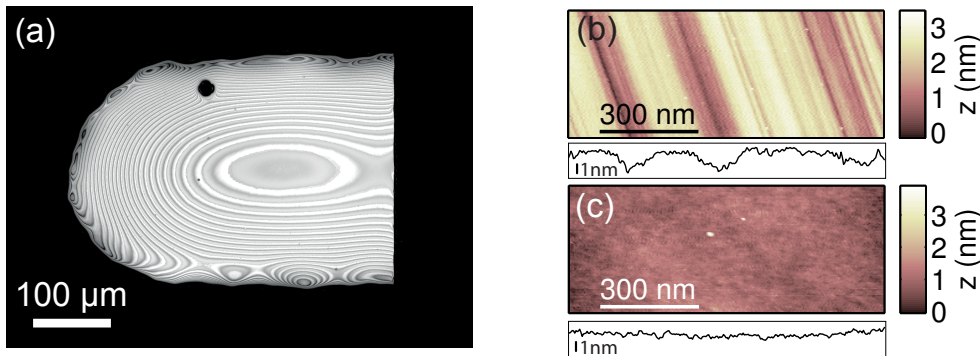
Figure 2.4: (a) Laser scanning confocal microscope (Keyence VK-X210, $\lambda =$ 408 nm) image of a 10-12 μm thick membrane etched from a 57 μm thick plate. Note the interference fringes, witnessing a thickness variation of roughly 1 μm (middle to sidewall) as well as the formation of a trench close to the mask. (b) AFM measurement of the commercially available diamond plate; marks due to polishing are clearly visible, the RMS roughness amounts to 0.7 nm. (c) AFM image of the same plate thinned to form a micron-thick membrane, the roughness is reduced (0.3 nm) and the polishing marks are no longer visible.

observe a significantly non uniform thickness of the final membrane, which is much thicker close to the mask than in the center. We measure the membrane's thickness at its free-standing edge using an SEM and estimate the overall thickness variation using a laser scanning confocal microscope (see Fig. 2.4 (a)). Our membranes for scanning probe fabrication finally have a thickness of around 1.5 μm in the center and 2.5-3 μm close to the mask. AFM measurements show that the etching process improves the surface quality of the membrane: Polishing marks observed before the etching (Fig. 2.4 (b), RMS roughness 0.7 nm) are not observed anymore after the

deep etch (see Fig. 2.4 (c)) and we find an RMS roughness of 0.3 nm for the thinned membrane.

We note that the trenching at the rim of the membranes as well as the non-uniformity might be reduced or even avoided using quartz masks with angled side-walls. Such angled sidewalls could reduce the effective thickness of the mask and thus lead to a more uniform etch rate and less trenching. Deep etches using this novel mask geometry, fabricated using laser cutting (Photonikzentrum Kaiserslautern, Germany), are currently being investigated.

2.2.4 Structuring scanning probes

Our scanning probes consist of 20 μm long, 3 μm wide cantilevers, which hold a nanopillars for scanning and sensing (see Fig. 2.1 (c), Fig. 2.5 (c) and Fig. 2.6 (a)). Following Ref. [75], we aim for pillars with $\approx$ 200 nm diameter and a straight, cylindrical shape to enable efficient collection of the NV fluorescence. The cantilevers are connected to a holding bar in the membrane by 500 nm wide bridges. These bridges are strong enough to reliably fix the cantilever to the membrane, but still allow for easy breaking off of the cantilever for subsequent mounting onto an AFM head.

To form these scanning probes, we use two mutually aligned electron beam lithography steps each followed by structuring via ICP-RIE. In the first step, the holding bar pattern together with the cantilevers are formed. Subsequently, pillars are structured on top of the cantilevers, as sketched in Fig. 2.5 (a).

For lithography, we use hydrogen silsesquioxane (HSQ), a negative electron beam resist (FOX-16, Dow Corning), as an etch mask. To create a thick mask with a high aspect ratio, we evaporate 2 nm Ti as an adhesion layer before spin coating a 600 nm thick layer of HSQ, which we bake on a hotplate at 90°C for 10 min. Note that the Ti layer only efficiently enhances the adhesion when not allowed to oxidize before applying the resist. We use electron beam lithography with 30 keV to pattern the HSQ layer. To prevent charging of the diamond sample, we expose the mask with currents below 50 pA and structure our 200 nm diameter pillar with a dose of 1500 μAs/cm^2 and the cantilever with a dose of 150 μAs/cm^2. Finally, we develop the samples for 20 s in 25 wt% TMAH and remove the Ti in 70°C hot 37% HCl. Both steps are followed by rinsing in de-ionized water and cleaning in isopropanol.

We transfer the HSQ masks into the diamond via an ArO$_2$ plasma (parameters see table 2.1). Our ArO$_2$ plasma enables a highly anisotropic etch while simultaneously creating a smooth surface in-between the etch masks. After each etch step, we remove residual HSQ and Ti using 20:1 buffered oxide etch (10:10:1 deionized water, ammonium fluoride, 40% HF) and clean the sample in a boiling tri-acid mixture and a solvent clean (see Sec. 2.2.1).

Fabricating the scanning probes requires multiple steps as illustrated in Fig. 2.5 (a): In the first step, we structure the pattern consisting of the transverse holding bars and the cantilevers. Additionally, markers (crosses) located adjacent to the thin membrane are defined in the HSQ mask and transferred into the surrounding diamond plate simultaneously to the pattern (markers not shown in Fig. 2.5 (a)). In
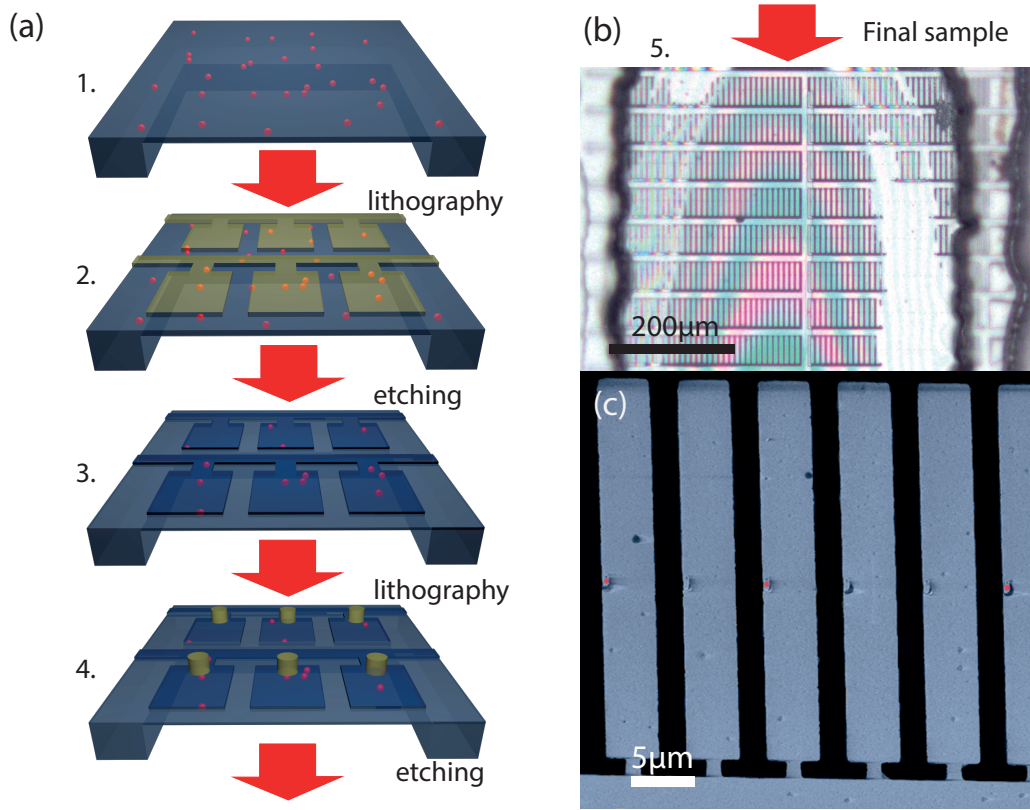
Figure 2.5: (a) Schematics of the fabrication process for the all diamond scanning probes; starting from the membrane (1.) with the shallowly implanted NV centers (red). We use electron beam lithography to structure a pattern (2.) consisting of transverse holding bars to which 20 μm long, 3 μm wide cantilevers are connected via 500 nm bridges (see also Fig. 2.6 (a)). The structure is transferred onto diamond (3.) via ICP RIE and afterward we sculpt the pillar on top via lithography (4.) and subsequent etching (5.). (b) Optical and (c) SEM image of the fabricated pattern of all diamond scanning probes fabricated using the alternative approach described at the end of this section.

the second step, we spin coat HSQ on top of the etched pattern which on top of the structures forms a homogeneous film. To ease marker identification, we mechanically remove the HSQ film on top of the markers using sharp needles. This allows us to clearly identify the markers during electron beam lithography and use them to align the pillars with respect to the cantilevers. In the last step, we transfer the pillar pattern into the diamond. As only the pillar is protected by an HSQ mask, the previously defined pattern including the membrane is thinned down during this etching. We continue etching, until the membrane is thinned to a point where all diamond material in-between the cantilevers has been etched away and the cantilevers remain free-standing. Note that the length of the pillars is limited by mask

erosion and faceting, as well as the formation of a trench around the pillar (see also Sec. 2.2.3) leading to detachment of the pillar from the cantilever. In general, we are able to etch $2\,\mu$m long wires with a $600\,$nm thick HSQ mask. As a consequence, we start with a membrane of $2-3\,\mu$m and etch $\sim 1\,\mu$m deep when we transfer the holding bars and cantilevers into the membrane. In the second step, we are thus able to etch $\sim 2\,\mu$m long pillars while removing all diamond material in-between the cantilevers. It should also be noted, that we have observed micromasking effects forming needles at the edge of the cantilever during this final etch step. While the magnetometry performance remains unaffected, we have explored an alternative approach to eliminate such micromasking effects. Based on the work of Ref. [20], we have also structured the cantilevers and pillars from different sides of the membrane (examples shown in Fig. 2.5 (b) and (c)). Although this approach fully eliminates the above mentioned micromasking problem, the alignment of the pillar with respect to the cantilever becomes challenging. Despite these drawbacks, both techniques allow mass-production of hundreds of scanning probes on a single membrane in one run (see Fig. 2.5 (b)).

Furthermore, the nano-fabrication results we present have been obtained using (100) oriented diamond material, however first results clearly indicate that our fabrication process is not restricted to this crystal orientation and can be extended to orientations more favorable for NV sensing applications, e.g. (111) [76].

2.2.5 Device characterization

We characterize the scanning probes to identify the most suitable devices to be transferred and integrated into our AFM setup. Fig. 2.6 (a) shows a confocal fluorescence map of our structured scanning probe array. To distinguish the scanning probes with single and multiple NV centers, we measure $g^{(2)}$ and the ESR spectra. We apply a moderate magnetic field mis-aligned with all four NV directions, which induces a splitting proportional to the magnetic field projection along the different NV symmetry axes (see Chap. 1). Thus, scanning probes with multiple NV centers aligned along more than one of the four equivalent $\langle 111 \rangle$ crystal-directions show multiple resonances. While multiple pairs of ESR dips quickly identify multiple NVs, no ESR signal identifies pillars without NV. As a single photon source, single NV center do not emit photons at the same time and therefore scanning probes containing single NV center can be reliably identified by a significant antibunching dip below 0.5 in the autocorrelation $g^{(2)}$ measurement (see Fig. 2.7 (a)) [77]. Using these measurements, we classify the scanning probes into devices with no, single and multiple NVs.

Figure 2.7 (b) shows the statistics of the number of NVs found in 79 scanning probes and reveals that approx. $30\,\%$ of them yield single NV centers. As expected, the number of NV centers per scanning probe follows a Poissonian distribution. Using the probability for 0 and 1 NV center per pillar, we deduce an average number of NV centers of $0.82\pm0.13\,$NV centers/scanning probe (see Fig. 2.7 (b)) corresponding to a NV density of $2.6 \times 10^9\,$cm^{-2} and a creation yield of $0.9\,\%$. We note that we
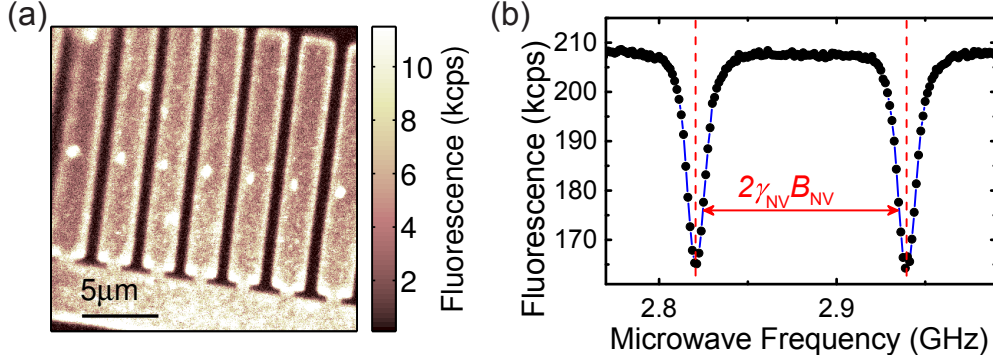
Figure 2.6: (a) Confocal image of an array of all-diamond scanning probes in 10^3 counts per second (kcps). (b) Typical optically detected electron spin resonance (ESR) for a scanning probe with a single NV center.
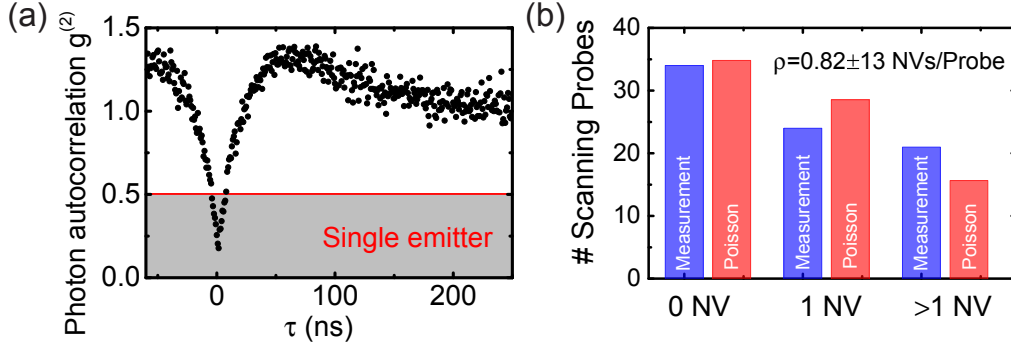
Figure 2.7: (a) Photon autocorrelation curve, $g^{(2)}$, measured on a scanning probe identifying a single NV center. (b) Statistics of the NV number per scanning probes for 79 scanning probes together with a Poissonian fit yielding an average of 0.82 ± 0.13 NV centers/scanning probe.

observed a high variation of this value between different diamond plates, which we attribute to variations in pillar diameter, uncertainty in the implanted nitrogen dose and possible variations in material properties (e.g. strain or vacancy concentrations).

The magnetometry performance of scanning probes with single NV centers is typically characterized by their sensitivity (η) to magnetic fields. The sensitivity set by the optical and spin coherence properties of the NV center can be derived from a Spin Echo measurement as described in Appendix B. For 13 scanning probes, we determined the coherence time and the magnetic field sensitivities as summarized in Fig. 2.8 (a) and (b). We find an average coherence time of $T_2 = 43 \pm 25\,\mu s$ and a sensitivity of $\eta_{AC} \approx 114 \pm 53\,nT/\sqrt{Hz}$. The shot noise limited sensitivity to DC magnetic fields can be equivalently determined, since $\eta_{DC} = \sqrt{T_2/T_2^*}\,\eta_{AC}$ (see Appendix B). Typical values for T_2^* are few μs. Assuming a comparatively short $T_2^* = 1\,\mu s$ therefore results in a DC sensitivity of $\eta_{DC} \approx 750\,nT/\sqrt{Hz}$.
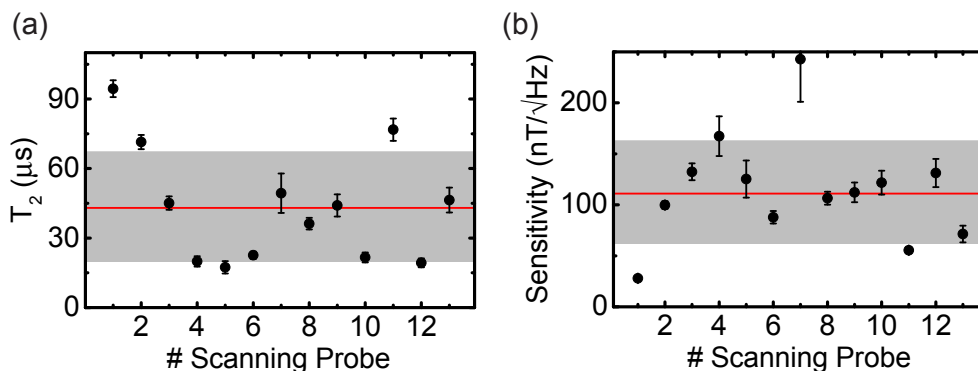
Figure 2.8: (a) Coherence time and (b) the AC sensitivity for 13 scanning probes with single NV centers. The red lines indicates the mean value of $T_2 = 43 \pm 25 \, \mu s$ and $\eta_{AC} \approx 114 \pm 53, nT/\sqrt{Hz}$ respectively. The gray region illustrates the standard deviation.

2.2.6 Transfer to scanning probe setup

In order to employ the scanning probes for imaging, the individually characterized cantilevers have to be transferred to an AFM head. Previous work employed ion beam assisted metal deposition to attach scanning probes to a quartz rod and subsequent focused ion beam (FIB) milling to detach the diamond scanning probe from the substrate [20]. This approach suffers from low yield, high complexity and significant contamination of the scanning probe by the Gallium ions used for FIB. Here we present an alternative method we developed to transfer the scanning probes using micromanipulators (Sutter Instruments, MPC-385) under ambient conditions. Using quartz micropipettes with an end diameter of $\sim 3 \, \mu m$, we apply $\sim 3 \, \mu m$ sized droplets of UV curable glue (Thorlabs, NO81) to the device to be transferred (see Fig. 2.9 (b)). After curing the glue, we remove the device from the substrate by mechanically breaking the 0.5 μm wide holding bar with the quartz pipette.

In a second step, we glue the quartz tip with the scanning probe to a tuning fork attached to an AFM head. To that end, we employ a stereo microscope setup which allows precise alignment of the scanning probe with respect to the AFM head and subsequent gluing of the quartz tip to the tuning fork using UV curable optical glue. As a last step, we carefully break the quartz pipette above its connection (gluing point) to the tuning fork using a diamond scribe.

With this procedure, we are able to produce tuning fork based AFM heads with the scanning probes aligned within a few degrees to the AFM holder in a robust and fast way. The UV glue forms a strong connecting link that can be used even in cryogenic environments and enables long-term use of the device.

Figure 2.9: (a) Schematic of the setup for gluing the scanning probe to quartz tips. (b) Optical microscope image during the transfer process. The scanning probe is glued to the apex of the quartz capillary tip using UV glue and the scanning probe is detached from the diamond chip by breaking. (c) SEM image of the final scanning probe attached to the end of the quartz tip.
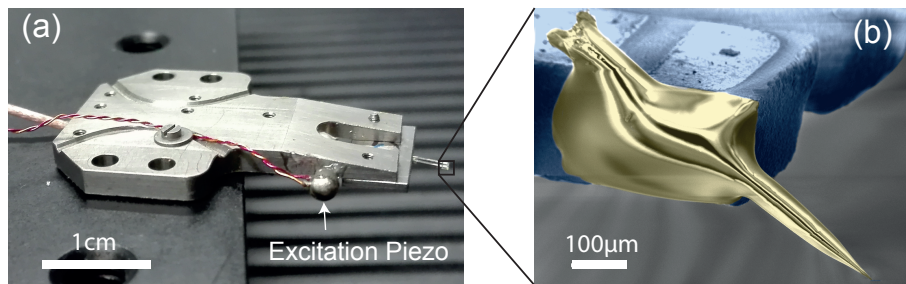
Figure 2.10: (a) AFM head equipped with the excitation piezo and the tuning fork mounted at the front end to form the lowest point of the AFM. (b) SEM image of the scanning probe attached to one prong of the tuning fork.

2.3 Imaging DC magnetic fields

We now demonstrate the performance of scanning probes by showing our device's capability to quantitatively image magnetic fields with nanoscale resolution. We applied NV magnetometry to study single Ni nanorods. These nanorods have various potential applications such as magneto-optical switches [78], probe particles in homogeneous immunoassays for the detection of proteins [79] or in microrheology [80]. NV center based magnetometry allows us to study the magnetic properties (spin densities, spin textures etc. [81, 23]) of individual particles. Here, we present two different approaches for imaging the stray field of single Ni nanorods which have typical diameters $\sim 24\,\mathrm{nm}$ and lengths $\sim 230\,\mathrm{nm}$ and which are deposited from a solution onto a quartz substrate (see inset of Fig. 2.11 (b), (d)).

2.3.1 Iso-B-imaging

To image the magnetic field of nanomagnetic objects the equi-magnetic field contour lines can be imaged using 'iso-B-imaging'. To that end, the driving MW frequency is set to be detuned from the ESR resonance frequency, with a detuning that corresponds to the magnetic field to be probed. In Fig. 2.11, this method is illustrated for two different magnetic field values for single Ni nanorods. To perform iso-B-imaging of the 0 G line, the driving microwave frequency (f_{MW}) is set to the NV transition frequency ($f_{NV}^{retracted}$) in the absence of the sample. The sample is subsequently approached and the NV is scanned in AFM contract across the sample. In the presence of a magnetic field, e.g. the stray field of the Ni nanorod, the frequency of NV spin transitions gets detuned from the MW frequency which results in an increase of NV fluorescence (see Fig. 2.11 (b)). Conversely, by setting the driving MW frequency to a detuning, which corresponds to a magnetic field of $B_{NV} \approx 21$ G, we obtain the 21 G iso-B-image as illustrated in Fig. 2.11 (c). It should be noted that the close proximity of the NV center to a surface may induce near field effects, such as lifetime changes and or quenching, which can affect the NVs fluorescence rates [20, 82, 83]. The magnetic signal can be decoupled from these effects, by collecting a second reference fluorescence signal (without MW driving) and plotting the difference between the fluorescence rates (see Fig. 2.11 (b) and (c)).
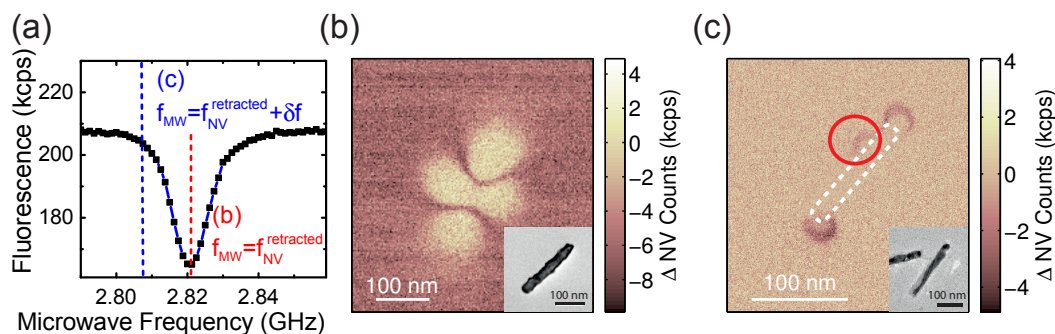
Figure 2.11: (a) ESR of the NV center inside a scanning probe in the absence of the sample (sample was retracted several μm). By setting the MW to a fixed frequency f_{MW} detuned from the ESR frequency, the magnetic field lines corresponding to this detuning are investigated. (b) 0 G iso-magnetic-field image of a single Ni nanorod. Negative fluorescence contrast indicates a local field of 0 G. The inset shows a SEM image of a rod. (c) The 21 G iso-B-image of a different nanorod with the encircled deviation from the expected dipole field. The inset shows a transmission electron microscope image (TEM) of a nanorod. We attribute the deviation from the dipole field to structural inhomogeneities.

Iso-B imaging is an efficient and fast method to investigate the magnetic field profile of magnetic objects. This profile can be used to derive the magnetic structure of the object by comparing the magnetic field with the expected profile. The 21 G iso-B-image, for example, clearly represents deviation from the expected dipole profile

(encircled in red), which we attribute to structural inhomogeneities of particular nanorods (see TEM image in Fig. 2.11 (c)).

2.3.2 Full field imaging via frequency locking

For a complete analysis of the magnetic stray field of a nanomagnetic object, it is necessary to perform full, quantitative magnetic stray field mapping. To that end, the Zeeman shift induced by the magnetic field needs to be detected for each point in the image. Various methods to measure the Zeeman shift have been discussed [23, 84, 85]. We implemented the approach presented in Ref. [84].
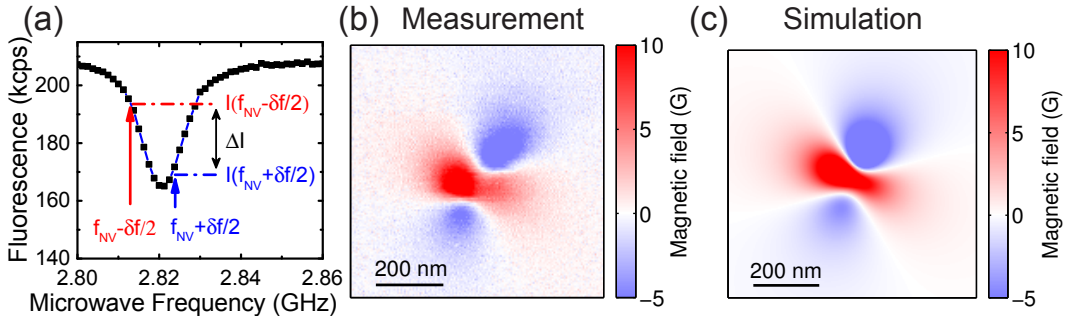
Figure 2.12: (a) ESR of the NV center inside a scanning probe. The red and the blue arrows indicate two driving MW fields at the frequencies $f_{\mathrm{NV}} - \delta f/2$ and $f_{\mathrm{NV}} + \delta f/2$ synchronized to two counters, measuring the fluorescence $I(f_{\mathrm{NV}} - \delta f/2)$ and $I(f_{\mathrm{NV}} + \delta f/2)$. Using a feedback, which locks the difference of the fluorescence ΔI to a setpoint of 0 kps, allows to track the transition frequency f_{NV} (the image illustrates the error signal ΔI before activating the feedback). By evaluating f_{NV} while scanning the sample the magnetic field can be imaged. (b) Full field map of a single Ni nanorod and (c) the simulated magnetic field of a point dipole ($m = 3.75 \times 10^{-17} \mathrm{A/m^2}$) projected onto the NV axis for an NV center located 80 nm above the dipole.

To determine the instantaneous NV ESR frequency at each point of the scan, a feedback loop is applied to lock the MW frequency to the NV spin transition frequency. For this feedback, two driving microwave fields, which have a detuning of δf are synchronized to two counters that measure the corresponding fluorescence rates $I(f_{\mathrm{NV}} - \delta f/2)$ and $I(f_{\mathrm{NV}} + \delta f/2)$ (see Fig. 2.12 (a)). The difference in fluorescence ΔI is used to lock the microwave driving frequency f_{NV} to the NV transition frequency. By keeping this ΔI at a setpoint of zero and setting $\delta f = 2\sigma_{\mathrm{Gaus}}$ (σ_{Gaus} is the standard deviation of the ESR resonance, see Appendix B), a maximum response of the feedback loop can be achieved and the local magnetic field can be evaluated by 'following' the locked MW frequency.

Using this technique, we imaged the full magnetic stray field of a single Ni nanorod as depicted in Fig. 2.12. The measured stray field matches the stray field expected for a single dipole. Assuming a point dipole with a magnetic moment of

$m = 3.75 \times 10^{-17} \text{A}/\text{m}^2$, as measured for similar rods with different methods [79], we calculated the magnetic field projected onto the NV axis. With this method we find good agreement between measurement and model and extract a distance of $70 \pm 10 \, \text{nm}$ between the sample surface and NV center. This distance defines the spatial resolution of the presented scanning magnetometer (see Sec. 2.5).

2.4 Sensitivity: Limitations and perspectives

All-diamond scanning probes enable sensitive evaluation of magnetic fields with a high spatial resolution. In this section, we highlight improvements that are currently investigated to increase the sensitivity of the presented scanning probe based sensing techniques.

Iso-B-imaging as well as full field imaging measures the magnetic field by evaluating the Zeeman shift in the ESR spectrum. For the all-diamond scanning probes used in the experiments, we typically achieve sensitivities of a few $\mu\text{T}/\sqrt{Hz}$. This sensitivity can further be improved using coherent spin manipulation protocols as discussed in Chap. 1, which allows to reach the maximum, currently achievable sensitivity of $\eta_{\text{DC}} \approx 750 \, \text{nT}/\sqrt{\text{Hz}}$ for DC magnetic fields and $\eta_{\text{AC}} \approx 114 \pm 53 \, \text{nT}/\sqrt{\text{Hz}}$ for AC magnetic fields (see Sec. 2.2.5).

These maximum sensitivities are finally limited by the corresponding coherence time and the fluorescence count rates (see Eq. 1.28). Thus, efficient detection of the NV's fluorecence is crucial for the development of highly sensitive scanning probes. Using our 200 nm diameter, cylindrical pillar, we increase the typical fluorescence count rates by a factor of ~ 3 compared to bulk diamond. More complex photonic geometries such as tapered pillars [86] are currently being investigated to enhance the collection efficiency and may be useful for scanning probes. Further improvements are also expected by optimizing the crystal orientation of the employed diamond samples. We employ (100) oriented diamond, which is the standard orientation of commercially available high purity diamond. However, we have demonstrated that the etching process can be adapted to (111) oriented diamond which yields improved photonic properties resulting in an increase of the fluorescence count by a factor of ~ 3 [76]. Combined with the coherence time of $235 \pm 46 \, \mu\text{s}$ of single NV centers in the 2 μm long pillar (no shallow NV centers) an extraordinary AC sensitivity of $\eta_{\text{Spin Echo}} = 28 \pm 10 \text{nT}/\sqrt{\text{Hz}}$ could be achieved [76].

A central advantage of the scanning probes is the use of high purity diamond, which in principle allows for long T_2^*, T_2 and T_1 times to be reached. Unfortunately, high resolution imaging requires NV centers in close proximity to the surface, which typically comes at the expense of shorter coherence times due to proximal surface spins [47, 49]. To analyze the possible impact of the fabrication process on our scanning probes and compare these effects to the literature, we characterized the coherence times. For the presented scanning probes, we have chosen an implantation depth of $9 \pm 4 \, \text{nm}$. This results in coherence times of $T_2 = 76 \pm 19 \, \mu\text{s}$ in the diamond plate before nanofabrication, which matches previous reports [47, 49].

In our scanning nanopillars, however, we find an average $T_2 = 43 \pm 25\,\mu$s. This reduced coherence time might be associated with plasma-induced defects at the diamond surface. Recent work [87] suggests that a low bias, 'soft' oxygen plasma or an annealing at 465°C in a dry oxygen environment [88] can minimize such plasma induced surface damages and could thereby increase coherence times. These and other methods for improving the NV properties using optimized surface terminations [89, 90, 91] or different creation procedures [25, 92, 93] still remain to be tested on diamond scanning probes and their influence on NV spin coherence properties remains an open question.

2.5 Spatial resolution: Limitations and perspectives

In optical microscopy the term resolution describes the smallest distance of which two separated (point-like) objects can be resolved. This resolution limit can be described by the Abbé diffraction limit, the Rayleigh criterion, or in modern physics by the full width at half maximum (FWHM) of the Point Spread Function (PSF), describing the response of the imaging system.

Classically, the PSF describes the measured intensity profile of a point source. For analyzing the resolution in terms of the FWHM of the PSF for our magnetometer, we therefore consider the measured magnetic field strength of a point like object such as a infinitesimal small domain or a single point dipole in a magnetic film. We assume the domain to be magnetized normal to the film plane (xy-plane) and parallel to the NV center symmetry axis (z-axis). This allows us to measure the z component of the magnetic field (B_z). The measured stray field B_z can be described by the stray field of two oppositely charged magnetic monopoles at the top and the bottom surface of the film [94], separated by the film thickness d. Figure 2.13 (a) depicts the stray field B_z of a small domain in a thick ($h_{\mathrm{NV}} \gg d$) and thin magnetic film ($h_{\mathrm{NV}} \ll d$) at a height $h_{\mathrm{NV}} = 100\,$nm, along the x-axis (for $y = 0$)[2]. The FWHM of the field profile of a thick film is given by $\mathrm{FWHM_{thick}} \approx 1.53 h_{\mathrm{NV}}$, whereas for the thin film it is given by $\mathrm{FWHM_{thin}} \approx 1.00 h_{\mathrm{NV}}$, which illustrates that the 'magnetic PSF' depends on h_{NV} as well as on the geometry. Note that besides the magnetic geometry, the 'magnetic PSF' also depends on the magnetization direction and the field projection that is measured [94, 95]. In contrast to conventional optical microscopes, the resulting imaging resolution therefore depends also on the sample geometry and the field projection to be measured. In all cases, the imaging resolution is, however, limited by the NV-to-sample distance h_{NV}, which therefore provides a relevant figure of merit for the resolution of our scanning NV magnetometer. Moreover, h_{NV} links the magnetic field strength at the position of the NV center with the magnetization profile and forms an important figure for estimating the applicability of our magnetometer for different experiments.

---

[2]The stray field of a thick film can be approximated by a single magnetic monopole and the magnetic field of a thin film is described by a dipole [94].
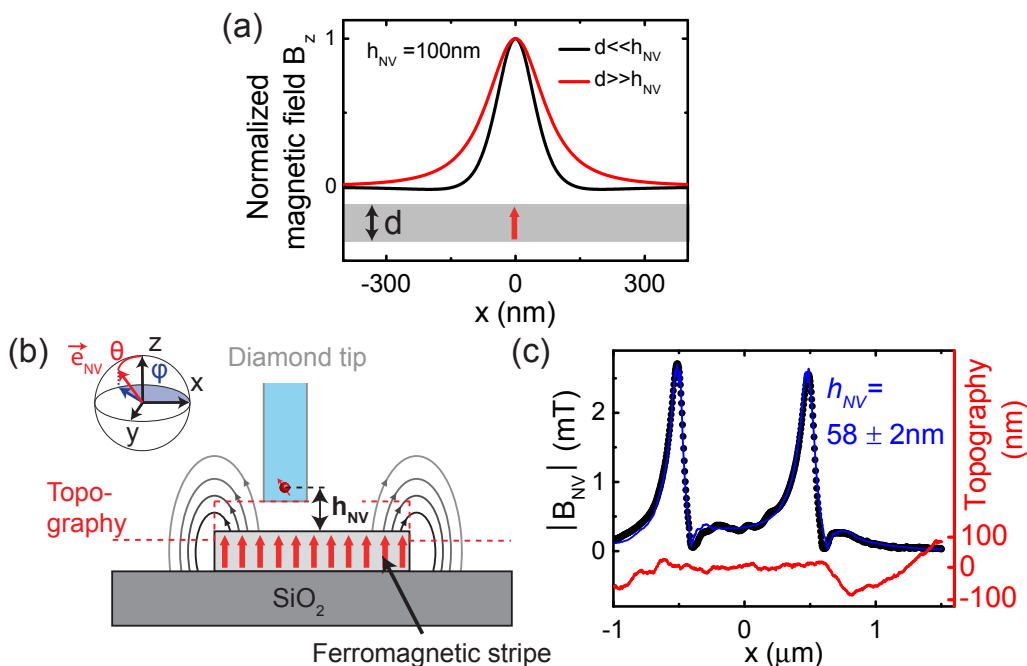
Figure 2.13: Calculated magnetic field profile $B_z(h_{NV})$ at $y = 0\,\text{nm}$ of a film with an infinitesimal small, perpendicularly magnetized, domain (red arrow). We assume a NV-to-sample distance of $h_{NV} = 100\,\text{nm}$ and show the profile for a thin (black) and a thick (red) film. The width of the resulting magnetic field profile differs in the two cases, which illustrates that the resolution depends on the geometry. In all cases, the imaging resolution is limited by h_{NV}, which therefore provides a relevant figure-of-merit for the resolution. (b) Schematic of the sample and sensor for the determination of h_{NV} using ferromagnetic stripes. The NV center incorporated in the diamond tip is scanned over the stripe, while the magnetic field is evaluated. The NV center measures the magnetic field along $\vec{e}_{NV}$ $(\theta_{NV}, \varphi_{NV})$, which is illustrated in the inset. (c) Magnetic field profile and measured topography (red) across the stripline. The black dots correspond to the measured magnetic field, while the blue curve is the modeled stray field (see main text). By fitting the model to the measured stray field, we extract a NV-to-sample distance of $h_{NV} = 58 \pm 2\,\text{nm}$.

We note that in literature, the ability to resolve the magnetic field is often referred to as resolution (or 'gradient resolution' [38]). This gradient resolution describes the highest gradient that can be resolved and is limited by the detector size, which for the NV center is defined by its wavefunction ($< 1\,\text{nm}$). Hence, claims of few nanometer and even subnanometer resolution can be found in literature [38, 96, 97]. This resolution, however, does not give information about the source of the magnetic field in most general cases.

During this thesis, several approaches have been developed to determine the NV-to-sample distance (see Chap. 3, Chap. 4 and Ref. [81, 15]). All approaches rely on modeling the magnetic stray field of the sample under investigation. The NV-to-sample distance can then be determined by fitting the modeled stray field to the measured magnetic field. Such determination (see Fig. 2.13 (c)) of the NV-to-sample distance was performed by T. Hingant et al. [81] on $1\,\mu$m stripes of a $1\,$nm thick, perpendicularly magnetized film of ferromagnetic CoFeB. More precisely, a multi-layer stack of $Ta(5\,nm)$-$Co_{20}Fe_{60}B_{20}(1\,nm)$-$MgO(2\,nm)$-$Ta(5\,nm)$ was deposited via sputtering on a Si/SiO2 substrate [81]. The magnetic field $\vec{B}(x, y, z)$ at the edge of an infinitely large film can be calculated by integrating the field generated by the magnetic surface charges at the top and the bottom surface. In the limit of a thin film the x and z components of the magnetic field can be expressed by [81]

$$B_x(x, h_{\mathrm{NV}}) = \frac{\mu_0 I_s}{2\pi} \frac{h_{\mathrm{NV}}}{h_{\mathrm{NV}}^2 + x^2} \tag{2.1}$$

$$B_z(x, h_{\mathrm{NV}}) = \frac{\mu_0 I_s}{2\pi} \frac{x}{h_{\mathrm{NV}}^2 + x^2}. \tag{2.2}$$

Here we introduce the surface moment density I_s, which is the product of the thickness d and the magnetization M.

The maximum stray field of B_x (for $x = 0$) scales as I_s/h_{NV}, while the width of the profile is given by a function that only depends on h_{NV}. The value of I_s and h_{NV} can therefore directly be determined by fitting the analytical model of the magnetic field to the measured field distribution across the edge of a homogeneously, perpendicularly magnetized film. Note that in the limit of $d \ll h_{\mathrm{NV}}$ the described stray field matches the magnetic stray field of a current I_s at the edge of the film (this current picture will be used in Chap. 3). Therefore, a one dimensional current carrying conductor can also be used to determine the NV to sample distance.

For characterization of our scanning probe based magnetometer, we also measured the stray field of CoFeB stripes (see Fig. 2.13 (c)). The overall magnetic field can be described by the magnetic field of each edge $B_{x,y}^{\mathrm{stripe}} = B_{x,y}(x, h_{\mathrm{NV}}) - B_{x,y}(x + w, h_{\mathrm{NV}})$, where w is the width of the stripe. The experimental data are depicted in Fig. 2.13 together with the fit, which yields a distance of $h_{\mathrm{NV}} = 58 \pm 2\,$nm, a moment density of $I_s = 99 \pm 3\,\mu_{\mathrm{Bohr}}/\mathrm{nm}^2$ and a NV orientation of $\theta = 62 \pm 2°$, $\varphi = 0 \pm 2°$. Note that the fitting routine also includes the topography and fits the magnetic field along the trajectory offset from the sample by h_{NV} (further details can be found in Ref. [81]).

Table 2.2 summarizes the NV-to-sample distance determined for different scanning probes and different types of experiments. We determined distances ranging from $9\,$nm[3] to $89\,$nm, with an average NV-to-sample distance of $h_{NV} = 50 \pm 32\,$nm describing the state of the art resolution of our magnetometer.

---

[3]Note that this result was obtained in the approximation of an infinitely thin superconducting sample. If the non-zero thickness of the superconducting film is taken into account, the distance needs to be corrected to $30\,$nm

Table 2.2: Extracted NV-to-sample distance for different scanning probes used in various experiments. The distance is determined by modeling the stray field and fitting to the measured magnetic field profile (more details in Chap. 3, Chap. 4 and Ref. [81, 15]). Note that the MW field of the stripline could vaporize water layer on top of the sample surface, which potentially result in a changed NV-to-sample distance. Furthermore, the experiments on the vortices in superconductor performed by L. Thiel et al. [15] were conducted in cryogenic environment, which also improves the AFM performance.

	CoFeB stripes	Cr_2O_3 stripes	Ni Nanorod	MW stripline	Vortex in superconductor
NV-to-sample distance (nm)	58 ± 2	89 ± 23	70 ± 10	25 ± 5	9 ± 3.5[3]

Note that we observed changes in the NV-to-sample distance while scanning and table 2.2 summarizes the smallest distance achieved with a particular scanning probe, which is typically achieved in the first few scans of a new probe. We attribute these changes to contaminations during the scan (potentially picking up and releasing dirt from the sample). On some used scanning probes, we observed such a contamination of the apex as depicted in Fig. 2.14 (b) , which further supports this scenario. To prevent this effect, the use of clean samples in a clean environment is essential. As the current setup is working in ambient conditions, there will always be the possibility of dust sticking to the sample or the scanning probe. To mitigate these issues, we currently investigate a method to clean the probes by scanning above small needles to mechanically remove the dirt [20]. This will help to restore the ability to place the probe near the surface and allows to study the effect of scanning probe contamination.

Neglecting the distance determined in Vortex imaging and the MW stripline because of potential changes of the NV to sample distances, results in an average distance of 72 ± 16 nm in ambient conditions. This distance is large compared to the tip-to-sample distance in typical AFMs. In non-contact AFM, short range (~ 1 nm) forces such as van der Waals, electrostatic and repulsive forces due to the Pauli exclusions are detected using sharp tips [61, 60]. A feedback loop is applied to lock the tip to a particular force in order to scan the tip in close proximity ($d_{AFM} \sim 1$ nm) to the sample and measure the topography. Under ambient conditions, additional long-range forces with different physical origin such as van der Waals, electrostatic, magnetic, capillary, etc., arise [98, 99]. Depending on the geometry and properties of the AFM tips, these forces can result in a larger distance between the tip and the sample [100, 60]. Our AFM tip is a diamond nanopillar with a diameter of 200 nm and a hydrophilic surface termination. In ambient conditions, this can induce long range forces, which might explain the NV-to-sample distance of 72 nm. To minimize the long range forces, the AFM needs to be operated with finer tips or in dry environment such as N_2 environment or vacuum. The experiments on vortices in

superconductor were conducted in He exchange gas in a liquid He bath cryostat and the determined NV-to-sample distance is smaller. Moreover, a smaller distance is also observed in the MW imaging experiments, where the MW field can possibly vaporize the water on the surface, which indicates such potential long range forces.
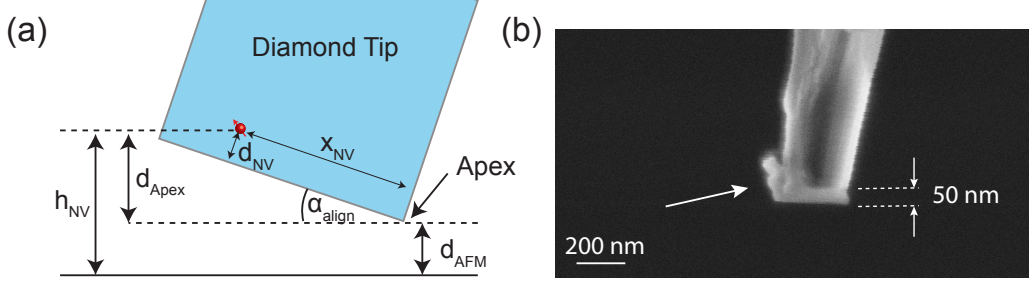
Figure 2.14: (a) Schematic of the NV-to-sample distance h_{NV}. Using an AFM feedback the NV center (red arrow) containing 200 nm wide nanopillar can be scanned at a distance of d_{AFM} given by the forces between the tip and the sample. h_{NV} finally consists of d_{AFM} and a distance of the NV-to-Apex d_{Apex} (we define the apex as the lowest point of the scanning nanopillar). d_{Apex} depends on the alignment angle of the nanopillar α_{align}, the lateral position x_{NV} and the implantation depth d_{depth}. When an aligned tip ($\alpha_{\mathrm{align}} = 0\,°$) can be scanned in a distance $d_{\mathrm{AFM}} \sim 1\,\mathrm{nm}$, defined by short range forces (see main text), we expect a NV-to-sample distance that is defined by the implantation depth $h_{\mathrm{NV}} \approx d_{\mathrm{depth}} = 9\,\mathrm{nm}$, which describes the achievable resolution. (b) SEM image of a contaminated nanopillar used in experiments. A spacing layer of a thickness of $\sim 50\,\mathrm{nm}$ can be observed leading to a larger than expected distance.

Another contribution to the NV-to-sample distance is the depth of the NV center in the diamond d_{NV}. We use N implantation at an energy of $6\,\mathrm{keV}$ to create NV center near the surface. We estimated the stopping range to be $9 \pm 4\,\mathrm{nm}$ using the Stopping Range of Ions in Matter software (SRIM, [71]). This estimation is based on a simulation of the scattering between ions and the atoms in an amorphous material. However, ions in the real diamond matrix can channel along symmetry axes of the diamond, which results in larger penetration depths of the ions. As the implantation was performed normal to the (100) sample surface, the nitrogen might channel $> 10\,\mathrm{nm}$ further than expected from SRIM simulation [87, 101]. Therefore, we currently investigate the influence of an angled implantation on d_{NV}, which will allow for better control over the distance to the surface.

A last contribution to the large NV-to-sample distance is the distance between the NV center and the apex of the scanning probe (see Fig. 2.14). The lowest point of the scanning probe with respect to the NV center depends on the alignment of the scanning probe (α_{align}) and the depth of the NV center in the diamond. Using a stereo microscope, we achieve an alignment within a few degrees to the

horizontal plane of the AFM. Depending on the lateral position of the NV center in the pillar (x_{NV}), this results in $d_{\mathrm{Apex}} \approx 10 - 30\,\mathrm{nm}$. Using an alignment based on laser deflection techniques would allow to reduce α_{align} and reach the optimal distance given by the implantation depth $d_{\mathrm{Apex}} = d_{\mathrm{NV}}$.

In conclusion, in this section we summarized the state-of-the-art resolution of NV magnetometry. In the experiments, performed during this thesis, we studied the stray field of magnetic objects with a resolution between $9\,\mathrm{nm}$ and $89\,\mathrm{nm}$. We find an average NV-to-sample distance of $50 \pm 32\,\mathrm{nm}$ and discussed several possible contributions to this large distance. We highlight recent developments, which we are currently investigating to overcome these limitations. If the scanning probe can be brought into close proximity ($\sim 1\,\mathrm{nm}$) with the sample, the resulting resolution is only limited by the implantation depth, which can be $9 \pm 4\,\mathrm{nm}$ using angled implantation [101]. Moreover, stable NV center in a proximity of $1\,\mathrm{nm}$ have been observed which defines the ultimate resolution this technique offers [13]. This extraordinary resolution, in combination with a sensitivity of $\eta_{\mathrm{DC}} \sim 750\,\mathrm{nT}/\sqrt{\mathrm{Hz}}$ and $\eta_{\mathrm{AC}} \sim 114\,\mathrm{nT}/\sqrt{\mathrm{Hz}}$, reveals the capabilities scanning NV magnetometry offers.

Chapter 3

Real Space Stray Field Imaging of Antiferromagnets

The rich physics of antiferromagnets (AF) offers attractive prospects for applications in spintronics and data storage. Magneto-electrical coupling enables electrical control of magnetism [102, 103, 104], high spin orbit torques allow for efficient spin to charge conversion [105], and the ultra-fast dynamics of AFs enable the high speed manipulation of magnetism [106]. Exploiting these attractive properties for next generation spintronic devices requires a tool to investigate the nanoscopic properties of AFs. Despite the absence of a bulk magnetic moment, in certain cases, the boundary introduces an asymmetry between the AF sub lattices that results in a small moment density at the boundary. In this chapter, we demonstrate real space imaging of the stray field produced by such surface moments for the collinear antiferromagnet Cr_2O_3 using scanning nanomagnetometry based on a single nitrogen-vacancy (NV) center in diamond. By measuring the stray field generated by the Cr_2O_3 surface moments, we capture an image of the underlying AF domain pattern and monitor its evolution through the AF-to-paramagnetic phase transition. These measurements provide evidence of local variations in the critical temperature T_{crit}, which we imaged here for the first time. Furthermore, the quantitative nature of NV magnetometry allows us to measure the surface moment density of Cr_2O_3 in ambient conditions. The measured moment density is reduced from the bulk value, which indicates a rearrangement of spins at the surface. Besides demonstrating the potential of scanning NV magnetometry for analyzing AFs, these measurements reveal phenomena, which are critical for the development of efficient spintronic or memory devices and can in the future systematically be studied using the presented methods.

3.1 Motivation

In recent years, many functionalities, so far realized using ferromagnets, have been implemented using more advantageous AF materials [106, 107, 108, 109]. New methods of manipulating and reading the AF order enabled the use of AFs for next generation spintronic and data storage devices [108, 109, 104]. A central requirement for these applications is the nanoscale control of the magnetic state. However, only a few techniques exist to image the magnetic structure on these length scales. Atomic resolution can be obtained by measuring the magnetic moments using spin-polarized scanning tunneling microscopy (STM) [110]. However, STM requires a conductive target and can therefore not be applied to the large class of insulating AFs. Spatial resolution of a few tens of nm can be achieved using magnetic force microscopy (MFM) or X-ray photoemission electron microscopy (PEEM) methods [111, 112, 113, 108]. Using X-ray magnetic linear dichroism (XMLD) PEEM the spin axis of antiferromagnets can be determined [111, 112, 108]. While this powerful technique allows to image domains with different spin axis, the detection of domains with different spin orientations within the same spin axis still remains challenging. The sensitivities reached in MFM and X-ray magnetic circular dichroism (XMCD) PEEM limit their applicability for measuring the weak magnetic signal of AFs for determining the spin orientation [113] and additional tools are required to study the whole variety of AF materials that are attractive for technology.

Scanning NV magnetometry is a promising, new method for the nanoscale study of AFs. The combination of a highly sensitive sensor, with the ability to place the sensor in close proximity to the sample, makes scanning NV magnetometry an attractive technique for measuring small magnetic fields with high spatial resolution [20, 38, 16]. In this chapter, we demonstrate the ability of this powerful technique to map the magnetic stray field of Cr_2O_3 and thereby deduce the domain structure and the surface moment density in ambient conditions.

3.2 The stray field of antiferromagnetic Cr_2O_3

For real space imaging of the stray field of an AF, we chose (0001) oriented Cr_2O_3, because of its special crystal structure. Cr_2O_3 has broken time and inversion symmetry but is invariant under subsequent application of time and spatial inversion [114, 115]. As a result, Cr_2O_3 exhibits a magneto-electric coupling and an asymmetry of the spin species, which can be described by a boundary magnetization that creates the stray field [114]. In order to link the measured magnetic field map with the underlying magnetic structure, we, in this section, provide models for analyzing the stray field emerging from AF Cr_2O_3, which enable the deduction of the domain structure and the determination of the moment density.

First, we introduce the microscopic structure of Cr_2O_3, from which we define a boundary magnetization resulting from a spin asymmetry at the surface. Based on this boundary magnetization, we then present an inverse Fourier propagation

protocol following earlier work presented in Ref. [116], which we apply to determine the domain structure from the magnetic field map of a thin Cr_2O_3 film . For a precise, quantitative determination of the moment density, we present a second, independent approach, which describes the magnetic stray field of a uniformly magnetized AF stripe. By fitting this model to our measured field maps, we can precisely determine the moment density, which provides important information about the surface and the sample.

3.2.1 The boundary magnetization of Cr_2O_3

The stray field of Cr_2O_3 can be described by its boundary magnetization originating from a spin asymmetry at the surface [114]. Generally, AFs have vanishing bulk magnetization because of the oppositely aligned moments in the two sub lattices, which macroscopically results in a vanishing stray field (see Fig. 3.1 (a)). When approaching the surfaces, however, the finite displacement between the sub lattices of the AF has to be considered, which generally results in small stray fields. (0001) oriented Cr_2O_3 is an A-type AF, where the spins are aligned orthogonal to the (0001) plane and the spins of the two sub lattices are vertically shifted with respect to each other (see Fig. 3.1 (a)). A boundary that is parallel to the plane of one sub lattice results in an asymmetry of the spins at this boundary. Because the two sub lattices of Cr_2O_3 are vertically shifted by approximately the lattice constant of one sub lattice (see Fig. 3.1 (a)), the stray field of the bulk AF can be neglected and the boundary magnetization responsible for the stray field represents the uncompensated spin layer at the boundary. Additionally, each oxygen (O) layer consists of an equal contribution from each sub-lattice. Removing one layer of O therefore results in the same spin asymmetry at the boundary, so that the resulting boundary magnetization is roughness insensitive [114], making Cr_2O_3 an ideal system for investigating domains in this AF.

For this work, Tobias Kosub and Denys Makarov (Helmholtz-Zentrum Dresden-Rossendorf e.V., Institute of Ion Beam Physics and Materials Research, 01328 Dresden, Germany) grew 200 nm thick Cr_2O_3 films using reactive evaporation of chromium in high vacuum onto c-cut sapphire substrates (Crystec GmbH) heated to 700 °C initially and to 500 °C after the first few monolayers [104]. The background gas used was molecular oxygen at a partial pressure of 10^{-5} mbar. Chromium was evaporated from a Knudsen cell and the oxide layers were subjected to a vacuum annealing process at 750 °C and residual pressure of 10^{-7} mbar directly after growth.

For the precise determination of the moment density, we structured 1 μm wide Cr_2O_3 stripes from a second 200 nm thick Cr_2O_3 film that was covered by 2 nm of Pt. We first fabricated stripe masks using ebeam lithography (30 keV) with a hydrogen silsesquioxane ebeam resist (HSQ, FOX-16 Dow Corning). The mask was afterwards transferred into the Cr_2O_3 using inductively coupled plasma reactive ion etching (ICP-RIE, Sentech SI 500) for 120 s in an $ArCl_2$ plasma (40 sccm Cl_2, 25 sccm Ar, 1.0 Pa pressure, 400 W ICP power, 100 W RF power with -232 V bias). We removed the etch mask using buffered oxide etch (10:10:1 deionized water, am-

(a)

(b)
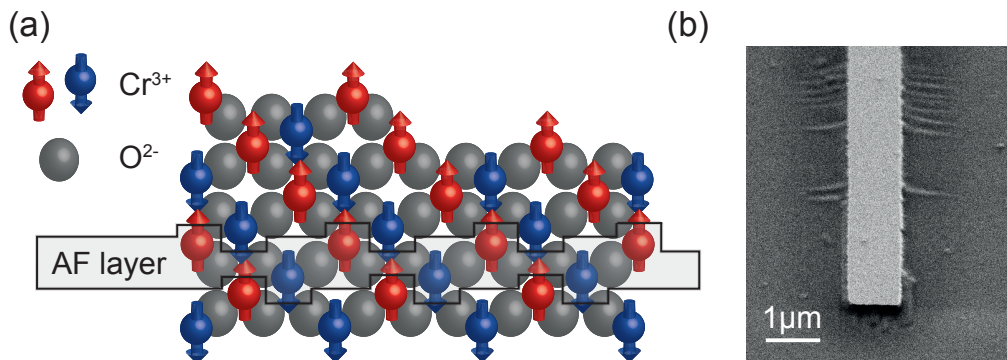
Figure 3.1: (a) Microscopic structure of Cr_2O_3. Red and blue arrows indicate Cr^{3+} spins and O^{2-} is depicted by the gray sphere. One AF layer consists of the oxygen (O) layer, the layer of spin up above and the layer of spin down below, which results in a roughness insensitive boundary magnetization. Its magnetization is given by the moment density of surface spins (see main text). (b) SEM image of a $1\,\mu m$ wide stripe, which was etched into the $200\,nm$ thick Cr_2O_3 film.

monium fluoride, $40\,\%$ HF) for $60\,s$ and characterized the final stripes using AFM and SEM (Fig. 3.1 (b)). The etch depth was $250\,nm$, which ensures that we removed all the Cr_2O_3 in-between the stripes. We also observed a tapering of the sidewalls, which we later included in the stray field calculation. The samples were finally mounted on a Peltier element, which allowed to control the temperature to $\pm 0.1\,K$. Prior to our imaging experiments, we cooled the sample through the critical temperature T_{crit} in a strong magnetic field produced by a nearby neodymium magnet to create a uniform magnetization state [104].

3.2.2 Fourier propagation of the stray field created by a Cr_2O_3 film

The relation between an arbitrary 2 dimensional domain profile in a thin Cr_2O_3 film and the stray field it generates can be described by a direct Fourier propagation [116]. By inversing this propagation protocol, we can directly determine the domain structure from a 2 dimensional magnetic field profile at a distance h_{NV} above the sample, as illustrated in Fig. 3.2.

To understand this protocol, we first consider the propagation of a stray field emanating from a sample. If no time-varying electric fields or currents exist, the magnetic field is curl free. This justifies the introduction of a scalar potential, which fulfills the Laplace equation $\Delta \phi = 0$. A general solution for this scalar potential is [116]

$$\phi(x,y,z) = \frac{1}{4\pi^2} \int \phi(k_x, k_y, 0) e^{i\vec{k}\cdot\vec{r}} e^{-\sqrt{k_x^2+k_y^2}z} d\vec{k}. \tag{3.1}$$
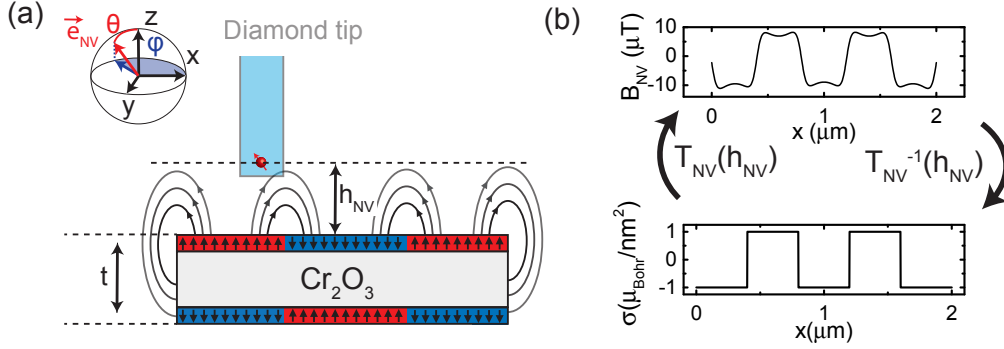
Figure 3.2: (a) Schematic of a Cr_2O_3 film and the sensor. The NV center incorporated in the diamond tip is scanned over the sample, while the magnetic field is evaluated. The NV center measures the magnetic field projected along the NV axis $\vec{e}_{NV}$ (θ_{NV}, φ_{NV}), that is generated by the boundary magnetization of the Cr_2O_3 film and can be modeled by a direct Fourier propagation. (b) Schematic of the Fourier propagation protocol. Using the propagator $T_{NV}(h_{NV})$ the moment density profile can be transformed into a magnetic field in a distance $h_{NV} = 100\,\text{nm}$ ($\theta_{NV} = 54°$, $\varphi_{NV} = 90°$). Using the inverse propagator the moment density profile can be determined from the measured magnetic field map.

The magnetic field is given by the negative gradient of the scalar potential. The scalar potential $\phi(\vec{k}, z) = \phi(k_x, k_y, 0)e^{-\sqrt{k_x^2+k_y^2}z}$ is the 2 dimensional Fourier transform of the real space scalar potential $\phi(\vec{k}, z) = \mathcal{F}[\phi(x, y, z)]$ (with $\vec{k} = (k_x, k_y)$), and decays exponentially with the distance z. The gradient on this scalar potential can be expressed in Fourier space as $\vec{\nabla}_k = (ik_x, ik_y, -k)^T$ [116]. Hence, the magnetic field can be calculated as

$$\vec{H}(x, y, z) = \mathcal{F}^{-1}\left[\vec{H}(\vec{k}, z)\right] = \mathcal{F}^{-1}\left[-\vec{\nabla}_k\phi(\vec{k}, z)\right]. \tag{3.2}$$

To evaluate the magnetic field at any point in space, we therefore need to determine the magnetic potential on the sample surface. This potential $\phi(k, 0)$ can be determined from the boundary conditions [116]

$$\Delta\phi = \rho_{\text{Volume}} = -\vec{\nabla} \cdot \vec{M} \tag{3.3}$$

$$\frac{\delta\phi(z = -0)}{\delta z} - \frac{\delta\phi(z = +0)}{\delta z} = \rho_{\text{Surface}} = -\vec{n} \cdot \vec{M}, \tag{3.4}$$

where we define the volume charge density ρ_{Volume} as the divergence of the magnetization $\vec{M}$. The surface density ρ_{Surface} is the scalar product of the magnetization and the normal vector $\vec{n}$ to the sample. The notation $z = \pm 0$ corresponds to above ($z = +0$) or below the surface ($z = -0$) in the limit $z \to 0$.

The magnetic field of the Cr_2O_3 film can be described by a magnetized ferromagnetic layer on top of the film and a second oppositely magnetized layer on the bottom of the film, as depicted in Fig. 3.2 (a). We first assume a single perpendicularly magnetized ferromagnetic film of thickness t_{layer} with a magnetization profile $\vec{M} = (0, 0, M_z(x, y))^T$. Such a film only exhibits surface charges at the top and bottom surface. The density and the corresponding magnetic field H at the surface can be determined from the continuity of the perpendicular component of the magnetic flux density B. Assuming the surface to be located at $z = 0$, the continuity of the magnetic flux densitiy B yields

$$
\begin{aligned}
B_z(z = +0) &= B_z(z = -0) \\
H_z &= -H_z + M_z(x, y) \\
H_z &= \frac{1}{2} M_z(x, y),
\end{aligned}
$$

(3.5)

where H_z corresponds to the stray field outside and $-H_z$ is the demagnetization field inside the magnetic material. The inverse of Eq. 3.2 together with Eq. 3.5 gives the scalar potential at the surface

$$
\phi(k, 0) = \frac{\mathcal{F}[H_z(z = 0)]}{k} = \frac{1}{2} \frac{\mathcal{F}[M_z(x, y)]}{k} = \frac{1}{2} \frac{M_z(\vec{k})}{k},
$$

(3.6)

where we introduce the Fourier transform of the magnetization profile $M_z(\vec{k})$. Using Eq. 3.1 and Eq. 3.2, we finally obtain the magnetic field in a height z from the surface

$$
\vec{H}(\vec{k}, z) = -\vec{\nabla}_k \frac{M_z(\vec{k})}{2k} e^{-kz}.
$$

(3.7)

This magnetic field corresponds to the magnetic field emanating from one surface. A thin film consists of two surface with opposite surface charges, which are separated by a thickness t_{layer}, resulting in an overall stray field of

$$
\vec{H}(\vec{k}, z) = -\vec{\nabla}_k \frac{e^{-kz}(1 - e^{-kt_{\text{layer}}})}{2k} M_z(\vec{k}) = -\vec{\nabla}_k \frac{e^{-kz}(1 - e^{-kt_{\text{layer}}})}{2kt_{\text{layer}}} \sigma(\vec{k}).
$$

(3.8)

In the limit of a very thin film $(kt_{\text{layer}} \ll 1)$ of fixed surface moment density $\sigma(\vec{k}) = M_z(\vec{k}) t_{\text{layer}}$, this results in

$$
\vec{H}(k, z) = -\vec{\nabla}_k \frac{e^{-kz}}{2} \sigma(\vec{k}).
$$

(3.9)

We model the stray field of the Cr_2O_3 film by the boundary magnetization. Thus, we assume two oppositely magnetized thin layers of spins which are separated by the thickness t. The components of the stray field can be calculated using

$$
H_{x,y}(\vec{k}, z) = -ik_{x,y} \frac{e^{-kz}(1 - e^{-kt})}{2} \sigma(\vec{k}) = T_{x,y} \sigma(\vec{k})
$$

(3.10)

$$H_z(\vec{k}, z) = k\frac{e^{-kz}(1 - e^{-kt})}{2}\sigma(\vec{k}) = T_z\sigma(\vec{k}), \qquad (3.11)$$

where $T_{x,y,z}$ are the propagators for the corresponding magnetic field components. Scanning NV magnetometry evaluates the magnetic field along the NV axis. The magnetic field along an arbitrary NV orientation parameterized by the polar angles θ_{NV} and φ_{NV} can be calculated by

$$
\begin{aligned}
B_{NV} &= \mu_0 T_{NV}(z, \theta_{NV}, \varphi_{NV})\sigma_z(\vec{k}) \qquad (3.12)\\
&= \mu_0 \left[\cos(\theta)T_z(z) + \sin(\theta)\left(\cos(\varphi)T_x(z) + \sin(\varphi)T_y(z)\right)\right]\sigma(\vec{k}).
\end{aligned}
$$

Using the propagator T_{NV}, the moment density profile can be transformed into a magnetic field at a height z from the sample, as illustrated in Fig. 3.2 (a). Moreover, using the inverse propagator a reverse propagation can be performed and the moment density profile can be directly determined from the 2 dimensional field map measured at a distance h_{NV} of the sample.

High frequency components (large k) of the moment density get damped by the exponential factor in the propagator (see Eq. 3.9). Conversely, by performing the reverse propagation, these fast oscillations including measurement noise get enhanced. To filter out such higher frequency noise, we introduce a filter function given by a Hanning window [117]

$$W(k) = \begin{cases} 0.5[1 + \cos(\pi\,[kh_{NV}/2\pi])], & \text{for } kh_{NV}/2\pi < 1 \\ 0, & \text{for } kh_{NV}/2\pi > 1 \end{cases} \qquad (3.13)$$

The cutoff frequency of $k_{cutoff} = 2\pi/h_{NV}$ is motivated by the fact, that the NV center can only resolve oscillations with a frequency given by the NV to sample distance h_{NV}.

The magnetic moment density profile can finally be determined from the measured magnetic field map using

$$\sigma(k) = T_{NV}^{-1}(h_{NV}, \theta_{NV}, \phi_{NV})W(k)\frac{B_z(k)}{\mu_0}. \qquad (3.14)$$

3.2.3 The stray field of a Cr_2O_3 stripe

For a precise determination of the boundary magnetization, it is necessary to model the stray field of a known geometry. Analogously to the determination of the moment density of thin ferromagnets [81], we model the stray field of Cr_2O_3 stripes in order to fit this model to the measurement.

A ferromagnetic film can be seen as the magnetic counterpart of planar capacitor as discussed in Chap. 2. For a thin film, this results in a stray field that can be described by a current at the edge of the film

$$B_x(x, h_{NV}) = \frac{\mu_0 I}{2\pi}\frac{h_{NV}}{h_{NV}^2 + x^2} \qquad (3.15)$$

$$B_z(x, h_{NV}) = \frac{\mu_0 I}{2\pi} \frac{x}{h_{NV}^2 + x^2}, \tag{3.16}$$

where the current I is set by the moment density and h_{NV} is the distance of the NV center from the sample (see Chap. 2).
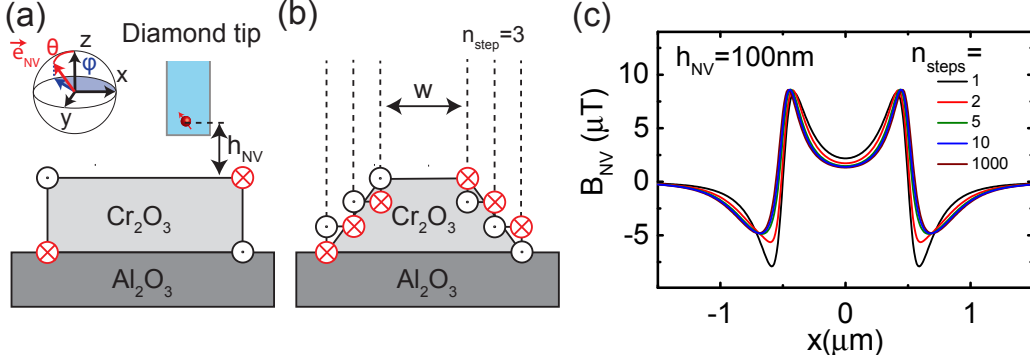
Figure 3.3: (a) Schematic of a Cr_2O_3 stripe. The magnetic field of the stripe can be calculated as the magnetic field of four currents at the edges. (b) The sidewalls of a tapered stripe are approximated as stairs carrying currents at the edges. (c) Calculated magnetic field of a stripe (width $w = 1\,\mu$m) with a tapered sidewalls (45°) in a height $h_{NV} = 100$ nm ($\theta_{NV} = 54°$, $\varphi_{NV} = 90$). The stray field for different numbers of steps indicates the convergence of this model.

The stray field of an AF film can be described as the stray field emerging from its boundary magnetization. We can thus assume a thin, perpendicularly magnetized film at the top surface and a second, oppositely magnetized layer at the bottom surface, as described in Sec. 3.2.1. The edge of an AF film is therefore characterized by an edge-current at the top and a second such current at the bottom edge, running in opposite directions (see Fig. 3.3 (a)). Thus, the stray field is given by $B_{x,z}^{edge} = B_{x,z}(x, h_{NV}) - B_{x,z}(x, h_{NV} + t)$. The measured AF stripes consist of two edges and the magnetic stray field can be interpreted as the magnetic field of 4 currents at the edges, as illustrated in Fig. 3.3 (a). The stray field is then given by $B_{x,z}^{stripe} = B_{x,z}^{edge}(x - w/2, h_{NV}) - B_{x,z}^{edge}(x + w/2, h_{NV})$, as depicted in Fig. 3.3 (c) (black curve).

The etching protocol described in Sec. 3.2.1 did not produce a straight, vertical etch but left tapered sidewalls to the stripe. We take this tapering of the sidewall into account by decomposing it into n_{steps} steps (see Fig. 3.3 (b)) and leaving the angle of the sidewall as fit parameter (see Appendix C). The final magnetic field is calculated as a field produced by $4n_{steps}$ currents. The stray field for an angle of 45° is plotted in Fig. 3.3 (c) for different n_{steps}, illustrating the convergence of the model. Finally, we fitted this model (where we chose $n_{steps} = 10$ as a trade-off between calculation time and accuracy of the model), to the measured magnetic field map to precisely determine the NV-to-sample distance and the moment density.

3.3 Antiferromagnetic domain imaging

To reveal the domain structure of Cr_2O_3 thin films, we applied scanning NV magnetometry to image the stray field emanating from the boundary magnetization. We first created AF domains in Cr_2O_3 by heating the sample into the paramagnetic phase, then cooling it back into the AF phase, while applying no external field [104]. With our scanning NV magnetometer, we afterwards captured the magnetic field in close proximity to the surface of the Cr_2O_3 film, as shown in Fig. 3.4 (a). The stray field image immediately confirms the presence of domains with opposite boundary magnetization, yielding regions of positive or negative B_{NV}. The strongest fields are at the boundaries between domains, as expected from a magnetization configuration that rapidly changes sign at the boundary.
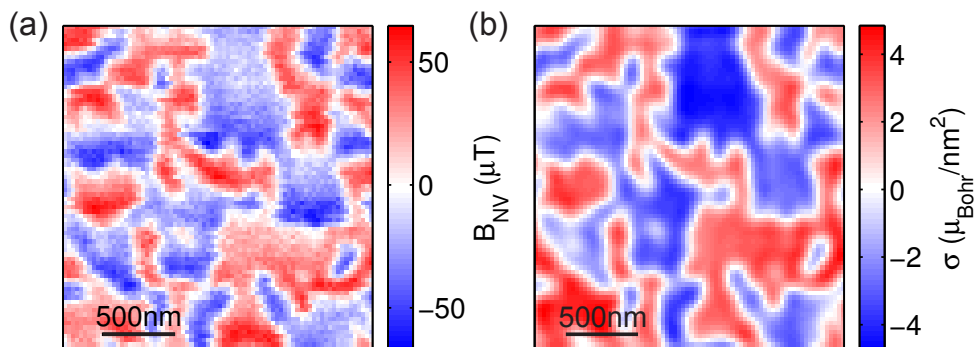
Figure 3.4: (a) Measured magnetic field map and (b) extracted moment density profile of the 200 nm thick film of AF Cr_2O_3. The moment density profile reveals multiple domains with a domain size of ≈ 200 nm.

To find the underlying magnetization pattern, we first determine the NV-to-sample distance by the following fitting routine based on the reverse propagation of the field in Fourier space (see Sec. 3.2.2). From the reverse propagated moment density profile, we extract the locations of the domain boundaries. Based on the assumption that the boundary is uniformly magnetized within a given domain, we project $\sigma(x, y)$ onto $\{+\sigma, -\sigma\}$: $\sigma_\pm(x, y) = \sigma\mathrm{sign}[\sigma(x, y)]$. We then forward propagate $\sigma_\pm(x, y)$ to compare with the original stray field data. Using a least square fitting routine, we can then find the values of the NV-to-sample distance ($h_{NV} = 121$ nm), the NV orientation ($\theta_{NV} = 54°$, $\varphi_{NV} = 92°$) and the moment density ($\sigma = 3\,\mu_{Bohr}/nm^2$) that best reproduce the measured magnetic field. The determined values are subsequently applied to perform the back-propagation to generate the moment density profile, as depicted in Fig. 3.4 (b).

The moment density profile clearly shows domains with opposite magnetization, with the typical domain size of ≈ 200 nm (as determined by the radial width of the peak of the domain pattern's autocorrelation). Importantly, the stray field pattern is well described by the boundary magnetization model, confirming our basic understanding of the Cr_2O_3 magnetic configuration.
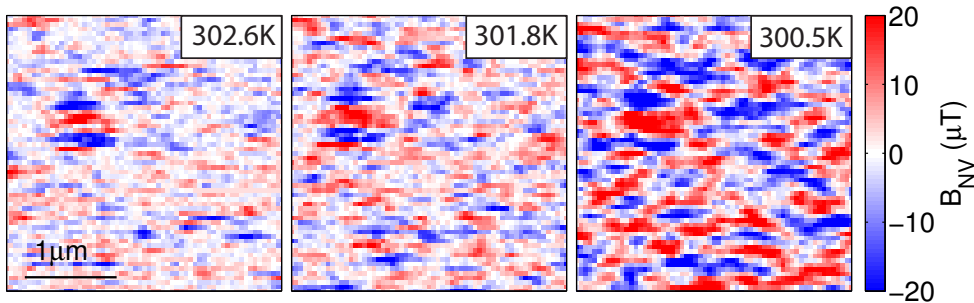
Figure 3.5: (a) Measured magnetic field map at several temperatures while slowly cooling the sample through the AF phase transition. As the sample is cooled, spatially separated regions of the film spontaneously form domains and adopt a uniform order parameter, resulting in the final multi domain pattern.

The ability to measure fine spatial features of the magnetization pattern enables a detailed study of the paramagnetic to AF phase transition at the level of individual domains. To further investigate this transition, we record snapshots of the stray field at discrete temperatures as the sample is cooled through the transition from $\sim 310\,\mathrm{K}$ to room temperature. A few such snapshots are depicted in Fig. 3.5. Initially, when the sample is above the transition temperature $\sim 310\,\mathrm{K}$, we see only noise in the magnetic field image, indicating no boundary magnetization and a paramagnetic phase. As the sample is cooled through the transition, spatially separated regions of the film spontaneously form domains and adopt a uniform magnetization. Interestingly, this spontaneous ordering occurs over a $2\,\mathrm{K}$ range of temperatures across the sample, with some regions already forming distinct domains while other regions are still paramagnetic. Although past studies have suggested such a behavior [118], this is the first direct observation of a spatially varying critical temperature in Cr_2O_3, which can explain the formation of multiple domains in this AF thin film.

3.4 Thermal cycling experiments

Because the bulk moments do not contribute to the measured stray field, the presented domain formation process does only describe the formation of the surface moments. To investigate whether the observed variations in T_{crit} and the resulting nucleation also describe the bulk behavior, we studied the reformation of the domains in the Cr_2O_2 film. To that end, we evaluated the correlation of two subsequent domain patterns before and after heating to a temperature T_{Heat} close to the phase transition. Specifically, we imaged the magnetic field at $299\,\mathrm{K}$ and extracted the normalized magnetization $M_{\mathrm{norm}} = \mathrm{sign}[B_{\mathrm{NV}}]$. We then heated the sample to T_{Heat} for several minutes and cooled the sample again to $299\,\mathrm{K}$ before we imaged the newly formed domain pattern (see Fig. 3.6 (a)).
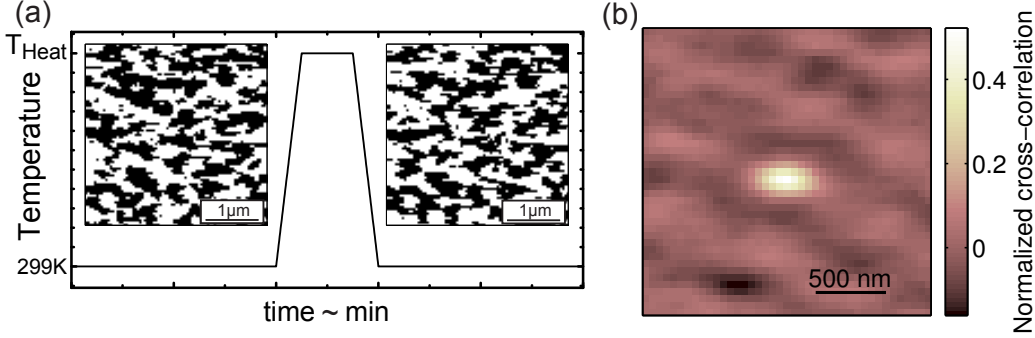
Figure 3.6: (a) Measurement routine for the correlation analysis of the reformation process of the domains. The normalized magnetization representing the domain pattern is extracted from a field map before the sample is heated to a temperature T_{Heat} close to the phase transition. After this, the sample is cooled and the reformed domain pattern is extracted again. (b) Cross-correlation of the two subsequent magnetization patterns. The clear maximum illustrates a correlation, which represents unaltered areas in the compared domain images.

Figure 3.6 (b) illustrates the normalized cross-correlation map between two subsequent domain images for $T_{\text{Heat}} = 301\,\text{K}$. Although the domain pattern changed, the maximum in the cross-correlation map clearly identifies a relation between the images. To better interpret this correlation, we need to examine the equation for the normalized cross-correlation:

$$n_{\text{corr2}}(x_i, y_i) = \frac{1}{N} \sum_{x_i=-N_x}^{N_x} \sum_{y_i=-N_y}^{N_y} M_1(x,y) M_2(x + x_i, y + y_i). \qquad (3.17)$$

Here M_1 and M_2 are the magnetization pattern before and after heating and N is the overall number of pixels. Since we clipped our data to $\{-1, 1\}$, the product of two correlated pixels is always 1, whereas for anti-correlated pixels it is -1. Consequently, two identical patterns, which consist of only correlated pixels, result in a value of the normalized cross-correlation of 1. On the other hand, two randomly formed patterns, which have the same number of correlated and anti-correlated pixels, result in an overall value of 0. As the correlation is the sum of all pixels, we can interpret the value of the correlation as the fraction (of pixels), which did not alter between the images.

To analyze the dependence of the fraction of the domain pattern which is unaltered on T_{Heat}, we repeated the correlation analysis for different T_{Heat} as depicted in Fig. 3.7. The maximum of the normalized cross correlation gradually decreases at the phase transition. As the orientation of the surface moments represents the bulk order parameter, this gradual reduction provides a clear signature for the existence of local variations in T_{crit} in the 'bulk' of the AF film. Moreover, the phase transition measured by the vanishing magnetic field of the surface moments (Sec. 3.3) and by
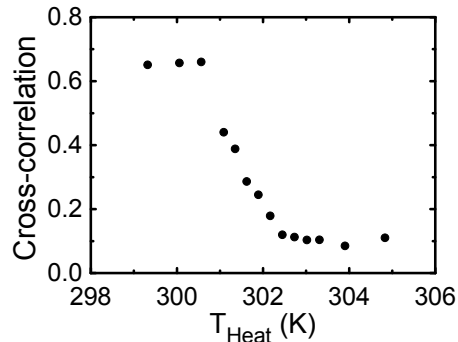
Figure 3.7: (a) Maximum of the normalized cross correlation between two subsequent domain patterns as a function of the heating temperature T_{Heat}. The gradual reduction of the correlation is a clear signature of variations of the critical temperatures that describe the bulk reformation of the domains

the 'bulk' reformation process occur at the same temperature range, which indicates a strong coupling between the surface moments and the bulk.

3.5 Determination of the surface moment density

The coupling of the surface moments and the AF 'bulk' of the thin film can be investigated by evaluating the average moment density, which provides interesting information about the properties of and interactions in the AF thin film. The reduction of $T_{\text{crit}} \approx 302\,\text{K}$ in our 200 nm thick AF film as compared to the bulk $T_{\text{Neel}} = 308\,\text{K}$ [119] is a commonly observed behavior for AF thin films [120, 121, 122]. This reduction can either be explained by the structural changes of the thin film or due to boundary effects [114, 123, 124]. Generally, the boundary induces additional interactions which modify the behavior of the surface magnetization. For NiO and MnO this results in an increased ordering temperature at the surface [125, 126] and for EuTe (111) a reduced magnetization was observed near the surface [127]. To analyze such surface effects in our Cr_2O_3 film we performed a quantitative determination of the surface moment density and compared this to the bulk moment of Cr^{3+}.

To precisely determine the surface moment density, we prepared $1\,\mu$m wide stripes, which were uniformly polarized by magnetic field cooling (see Sec. 3.2.1), and quantitatively measured the stray magnetic field, as depicted in Fig. 3.8 (a). The stray field of the $1\,\mu$m wide stripe can be modeled as the stray field of currents at the edges of the stripe as described in Sec. 3.2.3. Fitting this model to the stray field of 16 lines perpendicular to the stripes yields a distance of $h_{\text{NV}} = 89 \pm 23\,\text{nm}$ and a moment density of $\sigma = 2.8 \pm 1\,\mu_{\text{Bohr}}/\text{nm}^2$ (the details and the error estimation are discussed in Appendix C). To the best of our knowledge, this represents the first determination of surface moment density of Cr_2O_3 in ambient conditions.
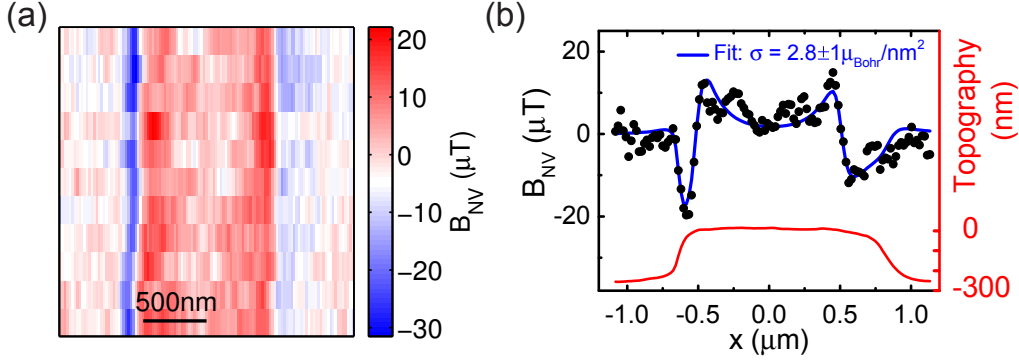
Figure 3.8: (a) Measured stray field map of the uniformly magnetized stripe. (b) Linecut of the magnetic field across the stripe. Black dots corresponds to the measurement and the blue line is the fitted field profile (see main text). The fitting of 16 linecuts yields an NV-to-sample distance $h_{NV} = 89 \pm 23$ nm and a moment density of $\sigma = 2.8 \pm 1 \, \mu_{Bohr}/nm^2$.

To compare this surface moment density with the Cr^{3+} bulk moment of $0.9 \mu_{Bohr}$[4] (assuming $T_{crit,bulk} = 300$ K for the measured thin film) at room temperature, we need to consider the microscopic structure of Cr_2O_3. (0001) oriented Cr_2O_3 exhibits a hexagonal, in-plane lattice with a unit cell of area $A_{unit\,cell} = 0.21 \, nm^2$ [129, 130, 131]. We assume the surface termination to be a cut between two oxygen layers of the bulk lattice, as depicted in Fig. 3.1 (a) [129]. This termination results in an occupation probability of one Cr^{3+} ion per unit cell, which together with our measurement of $\sigma = 2.8 \pm 1 \, \mu_{Bohr}/nm^2$ yield a magnetic moment of $0.6 \pm 0.2 \, \mu_{Bohr}$ per surface Cr^{3+} ion. Interestingly, this surface moment is notably reduced from the bulk value, which can originate from different phenomena. First of all, different physical surface structures have been reported in literature [115, 130, 129, 132]. These structures have different lattice constants and occupation probabilities of the Cr^{3+} ions for the first four layers, which leads to changes in the surface moment density. Secondly, interactions in the thin film can be modified by film parameters such as strain. In combination with the additional interactions arising from the boundary, this can allow spins at the surface to either change their thermal averages, change their spin state, or flip [114]. Moreover, such modified interactions can also result in a different temperature dependence of the surface moments, which can make a direct comparison of the moments near the phase transition ambiguous [133]. Further measurements, including structural analysis and low temperature measurements, are required to connect the measured moment density with the surface structure. How-

---

[4]The bulk value of the moment per Cr^{3+} is determined from the temperature dependence of the magnetization obtained in neutron measurements presented in Ref. [119], which we calibrate using the low temperature value of $2.76 \, \mu_{Bohr}$ from Ref. [128]. We assumed $T_{crit} = 300$ K as the lower bound for T_{crit} and thus, the determined moment at room temperature forms a lower bound of the bulk moments of the measured thin film.

ever, our data provide evidence that the simplified model for the surface presented in Fig. 3.1 cannot explain the measured surface moments. This indicates a possible impact of the boundary on the moment density, which will also have an influence on the thin film properties.

Note that in our analysis we assume oppositely magnetized layers of the same spin-densities at the top and the bottom surface. However, due to the discussed boundary effects, the two magnetized layers may have different densities, since one surface is terminated by the sample substrate an the other by air or Pt. Recently, ferrimagnetic moments have been reported for Cr_2O_3 films, which arise from interface defects during the growth process [104]. For the obtained NV-to-sample distance the magnetic field is mainly defined by the top surface and only weakly influenced by the backside of the AF film. Hence, a small asymmetry between the layers only results in minor corrections to the moment density determined here. Furthermore, we also assume the moment density of the AF stripe to be constant, although the magnetization varies due to the local variations in T_{crit}. At room temperature, however, we only expect small variations, which are included in the statistical error of the measured moment density.

We also note that we fabricated the stripes from a Cr_2O_3 film, which was covered by a 2 nm thick film of Pt. In our experiments we did not observe any changes of the magnetic stray field measured on samples with and without Pt layer, and therefore expect only minor corrections due to the Pt. Moreover, the stripes exhibit a roughness of several nm, indicating that the Pt was potentially etched during the fabrication process. However, the rough surface by itself might modify the surface interactions, which may lead to changes in the moment density [123]. The moment density extracted from the 2 dimensional stray field image measured directly on a flat Cr_2O_3 film, yields $\sigma = 3\,\mu_{Bohr}/nm^2$ (see Sec. 3.3) and is in accordance with the value determined using the stripe. We therefore conclude that neither the Pt cover layer nor the surface roughness explains the observed reduced moment density.

3.6 Conclusion

In this chapter, we imaged the stray field of a 200 nm thick Cr_2O_3 film using scanning NV magnetometry. We revealed the AF domain structure with an average domain size of ~ 200 nm. Furthermore, the performance of scanning NV magnetometry allowed us to study the evolution of the domains during the AF-to-paramagnetic phase transition. We observed the formation of domains in spatially separated regions of the film, which suggest that the film exhibits spatially varying T_{crit}. We analyzed the correlation between reformed domain patterns before and after heating to a temperature at the phase transition, which verified that the observed variations in T_{crit} describe the 'bulk' reformation process. These variations in T_{crit} are a critical ingredient for the existence of multiple domains in the Cr_2O_3 film, which we imaged here for the first time.

Moreover, the quantitative nature of scanning NV magnetometry allowed us to determine the surface moment density of $\sigma = 2.8 \pm 1 \, \mu_{\mathrm{Bohr}}/\mathrm{nm}^2$ at room temperature. Interestingly, this measured moment density cannot be explained by modeling the surface to be a cut through the bulk lattice and indicates additional interactions originating from the boundary.

The presented measurements therefore provide a new route to probe AF properties, which are inaccessible to other techniques. The systematic analysis of surface effects may allow to optimize AF thin film properties and the local variations in critical temperature can potentially be exploited for local control of AF domains, which may allow to develop highly efficient, highly dense memory devices.

To conclude, we want to highlight that a boundary magnetization can be found at surfaces of all AFs, which break time and space inversion but are invariant under subsequent application of time and space inversion. The resulting small stray field of other materials which exhibit this symmetry, such as the mentioned NiO, MnO and EuTe [125, 126, 127] or the currently investigated tetragonal CuMnAs [121, 108], can potentially be measured using scanning NV magnetometry. Additionally, recent experiments on bismuth ferrite have demonstrated that the small stray field emanating from the canting of AF moments can be imaged using single NV center [134]. All these measurements establish scanning NV magnetometry as an exciting, new sensing technique for studying the nanoscale properties of AFs, which paves the way for the development of next generation memory and spintronic devices.

Chapter 4

Nanoscale Microwave Imaging

In this chapter, we demonstrate our scanning NV magnetometer's ability to measure and image microwave (MW) magnetic fields by quantitatively imaging the magnetic field generated by a high frequency (GHz) MW current with nanoscale spatial resolution. Together with a shot noise limited MW magnetic field sensitivity of $800\,\mathrm{nT}/\sqrt{\mathrm{Hz}}$, our room temperature experiments establish scanning NV magnetometry as a versatile and high performance tool for MW imaging. Our system furthermore offers polarization selectivity and broadband capabilities. The results presented in this chapter are published in Ref. [17].

4.1   Motivation

Imaging and detecting MW fields constitutes a highly relevant element for engineering of future MW devices as well as for applications in atomic and solid state physics. For instance cavity quantum electrodynamics experiments with atoms [135, 136] and superconducting qubits [137, 138] or the coherent control of quantum magnets [139] and quantum dots [140] are based on manipulating quantum systems with MW electric or magnetic fields. Precise control and knowledge of the spatial distribution of the MW near field is thereby essential to achieve optimal device performance. Also, magnetic systems are known to exhibit a large variety of collective magnetic excitations, including spin waves [141] or excitations in frustrated magnets [142, 143]. Imaging such magnetic excitations on the nanoscale would be a crucial step towards their fundamental understanding and the development of new spintronics devices, such as magnonic waveguides [144] or domain wall racetrack memories [145]. As a consequence, various techniques have been designed to image MW electric and magnetic fields, including scanning near field microscopy [146, 147, 148], micro-Brillouin light scattering [149], superconducting quantum interference devices [150] and imaging with atomic vapor cells [151, 152, 153] or ultracold atoms [154]. With only a few exceptions [149], most of these techniques however lack a nanoscale spatial resolution or are restricted to operation in cryogenic or vacuum environments.

Microwave magnetic field imaging using NV centers in diamond offers a promising alternative. Recently, magnetometry of MW magnetic fields has been demonstrated using an NV spin in bulk diamond [155], with a resulting MW magnetic field sensitivity of $\sim 1\,\mu\text{T}/\sqrt{\text{Hz}}$. However, the bulk NV centers employed in [155] severely restricted spatial resolution in imaging, and in particular do not allow for nanoscale imaging of MW near fields, which remains an outstanding challenge for NV-based MW imaging. In this chapter, we address this issue and demonstrate the first nanoscale MW imaging using a scanning NV magnetometer [17]. Our proof-of-concept imaging experiments were performed on a prototypical MW circuit - a micron-scale MW stripline - and yield nanoscale resolution combined with shot noise limited MW magnetic field sensitivity of $800\,\text{nT}/\sqrt{\text{Hz}}$.

4.2 Prototypical stripline for microwave excitation

The MW stripline structure depicted in Fig. 4.1 forms an ideal system for demonstrating MW magnetic field imaging. The right angled edges of the stripline results in a complex MW stray field, which we image to demonstrate the performance of our scanning NV magnetometer. In contrast, the stray field of the straight wire of the stripline can be described by an analytical function. Comparing the measured magnetic field with the modeled stray field enables the determination of current density and the NV-to-sample distance, which forms an important figure of merit for scanning NV magnetometry and allows to determine the sensitivity for MW currents.

The 2.5 μm wide MW stripline is patterned onto a Si substrate by electron beam lithography and evaporation of 60 nm of Pd. The substrate is undoped Si with a 300 nm SiO_2 toplayer. A MW source (Rhode&Schwarz SMB 100A) is used to drive a MW current I_{MW}, with a frequency in the GHz range, through the stripline.
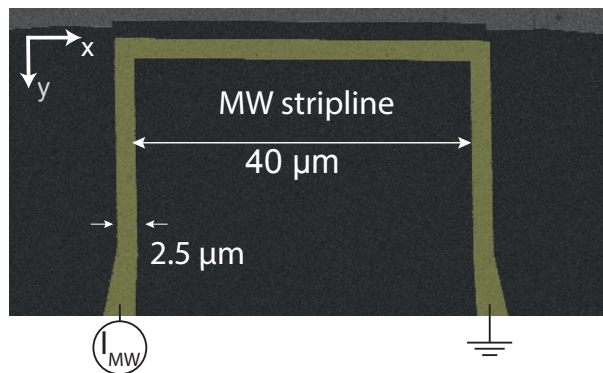
Figure 4.1: False-colored SEM image of the stripline geometry used for MW magnetic field imaging. An input current is applied to one end of the 2.5 μm wide Pd stripline (yellow) while the second end is grounded.

4.2.1 Analytical model of the microwave stray field of a stripline

For describing the stray field of a MW current in the straight part of our stripline geometry, we use an analytical expression for the generated magnetic field. Because the stripline thickness $t = 60$ nm is much smaller than its width $w = 2.5\,\mu$m, the stripline can be considered as an infinitely thin wire and because the skin depth of palladium ($\delta = 3.5\,\mu$m at 2.825 GHz) is larger than the width (and in accordance to the finite element simulation, see Sec. 4.2.2) we can assume a homogeneous MW current density (except at the right angled bend of the MW conductor). We define the stripline to be aligned along the y direction which results in a homogeneous current density $\vec{J} = (0, J, 0)$. The problem can therefore be treated as a 2D problem in the xz plane.
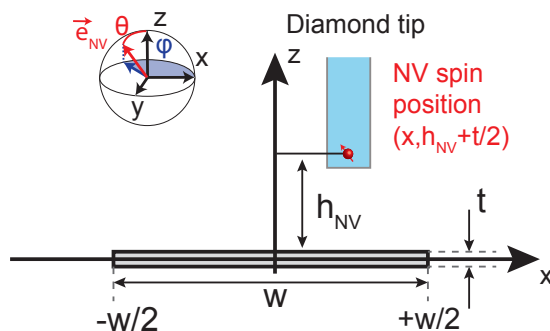
Figure 4.2: Model for the MW stripline. The stripline is centered in a xy plane and has thickness t and width w. The NV center is scanned at a distance h_{NV} above the surface across the stripline.

For calculating the magnetic field we use Poisson's equation and determine the y-component of the magnetic vector potential [94]

$$A_y(\vec{r}, J) = \frac{\mu_0}{4\pi} \int \frac{J(x', z')\, dV'}{|\vec{r} - \vec{r}'|}, \tag{4.1}$$

where A_y is evaluated at the coordinates of the NV given by $\vec{r} = (x, h_{\mathrm{NV}} + t/2)$ and $\vec{r}' = (x', z')$ is the integration variable.

Equation 4.1 can be evaluated analogously to an electrostatic potential with a charge distribution $\rho(x', z')$ [156]

$$
\begin{aligned}
\Phi &= \frac{1}{4\pi\epsilon_0} \int \frac{\rho(x', z')\, dV'}{|\vec{r} - \vec{r}'|} \\
&= -\frac{1}{2\pi\epsilon_0} \iint \rho(x', z') \ln\left(\frac{\sqrt{(x - x')^2 + (z - z')^2}}{r_0}\right) dx'\, dz',
\end{aligned} \tag{4.2}
$$

where r_0 is an integration constant. Consequently Eq. 4.1 becomes:

$$A_y(\vec{r}, J) = -\frac{\mu_0}{2\pi} \iint J\left(x', z'\right) \ln\left(\frac{\sqrt{(x-x')^2 + (z-z')^2}}{r_0}\right) dx' dz'. \tag{4.3}$$

Following the assumption of the infinitely thin wire, the integration on the right hand side of Eq. 4.3 over z' amounts to Jt. Using the integration boundaries depicted in Fig. 4.2, the magnetic potential reduces to

$$A_y(\vec{r}, J) = -\frac{\mu_0 Jt}{2\pi} \int_{-w/2}^{w/2} \ln\left(\sqrt{(x-x')^2 + z^2}\right) dx'. \tag{4.4}$$

The corresponding MW magnetic field is determined from

$$\vec{B}'_{\mathrm{MW}}(\vec{r}, J) = \vec{\nabla} \times \vec{A}(\vec{r}, J) = \begin{pmatrix} -\partial_z A_y(\vec{r}, J) \\ 0 \\ \partial_x A_y(\vec{r}, J) \end{pmatrix}. \tag{4.5}$$

The MW magnetic field in the coordinate system of the NV center (see coordinate system in the inset of Fig. 4.2) can be calculated by a rotation around the NV angle θ and φ which yields

$$\vec{B}_{\mathrm{MW}}(\vec{r}, J, \varphi, \theta) = \begin{pmatrix} -\partial_z A_y(\vec{r}, J)\cos\varphi\cos\theta - \partial_x A_y(\vec{r}, J)\sin\theta \\ \partial_z A_y(\vec{r}, J)\sin\varphi \\ -\partial_z A_y(\vec{r}, J)\cos\varphi\sin\theta + \partial_x A_y(\vec{r}, J)\cos\theta \end{pmatrix}. \tag{4.6}$$

With Eq. 4.6, we can finally determine the polarization component σ_- orthogonal to the NV axis, which can be measured with the NV center (see Chap. 1)

$$\begin{aligned} B_{\mathrm{MW}}^-(\vec{r}, J, \varphi, \theta) &= |B_{\mathrm{x,MW}}(\vec{r}, J, \varphi, \theta) + iB_{\mathrm{y,MW}}(\vec{r}, J, \varphi, \theta)| \\ &= |-\partial_z A_y(\vec{r}, J)\cos\varphi\cos\theta - \partial_x A_y(\vec{r}, J)\sin\theta + i\partial_z A_y(\vec{r}, J)\sin\varphi|. \end{aligned} \tag{4.7}$$

Since $\vec{r} = (x, h_{\mathrm{NV}} + t/2)$, the MW magnetic field strength depends on $x, h_{\mathrm{NV}}, t, J, \varphi, \theta$. With the thickness being $t = 60\,\mathrm{nm}$, we apply Eq. 4.7 to calculate the magnetic field at a distance h_{NV} from the sample across the stripline.

4.2.2 Numerical simulation of the microwave field

For simulating the magnetic field of the entire geometry, we compute the MW magnetic field using a finite element simulation (RF module, COMSOL Multiphysics).

We assume a $50\,\Omega$ Pd stripline as described above surrounded by air. A current $I_{\mathrm{MW}} = I_p \sin\omega_{\mathrm{MW}} t$ is applied at the input of the stripline, while the other end is grounded (Fig. 4.1). We use a frequency $\omega_{\mathrm{MW}} = 2.825\,\mathrm{GHz}$ and an excitation current of $I_p = 10\,\mathrm{mA}$, which corresponds to a MW power of $P_{\mathrm{MW}} = 7\,\mathrm{dBm}$.
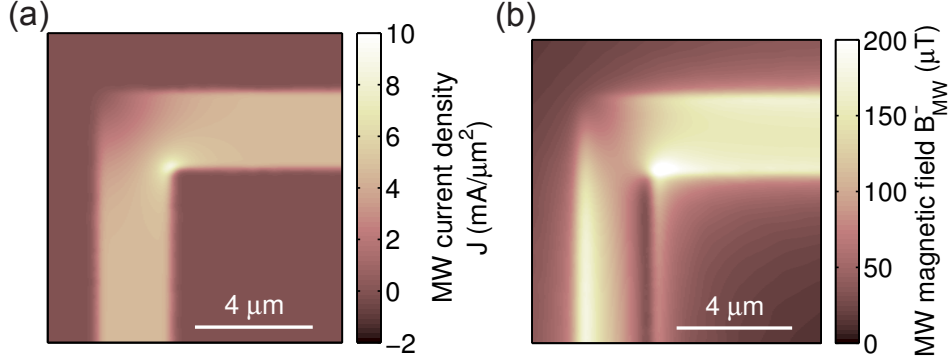
Figure 4.3: (a) MW current density and (b) σ_- polarization of MW magnetic field obtained from finite element simulations with COMSOL Multiphysics. The magnetic field is plotted for an NV orientation of $\theta = 49°$ and $\varphi = 104°$, a MW current density of $J = 3.9\,\text{mA}/\mu\text{m}^2$ and a distance $h_{\text{NV}} = 25\,\text{nm}$ above the sample. These values were determined from experiments (see Sec. 4.4).

We first compute the MW current density $\vec{J}_{\text{MW}}(\vec{r})$ at each position $\vec{r}$ for the given frequency ω_{MW} (Fig. 4.3 (a)). The MW current density is homogeneous in the MW stripline, except at the bends of the conductor. It should be noted that the skin effect can be neglected, as the skin depth of palladium ($\delta = 3.5\ \mu\text{m}$ at 2.825 GHz) is larger than the width and thickness of the MW stripline.

The MW magnetic field $\vec{B}_{\text{MW}}(\vec{r})$ can then be calculated from the current density and its σ_- polarization orthogonal to the NV axis can be extracted, as depicted in Fig. 4.3 (b).

4.3 Microwave magnetic field imaging

Our MW magnetic field detection is based on the ability of the MW field to drive coherent Rabi oscillations between the $m_s = 0$ and $m_s = \pm 1$ spin-states of the NV center, as introduced in Chap. 1. A MW field resonant with one transition therefore leads to an oscillation of the population between the two involved spin states. The oscillation frequency is then given by $\Omega^\pm/2\pi = \gamma_{NV} B_{\text{MW}}^\pm$, where $B_{\text{MW}}^\pm$ is the (right-) left-handed circularly polarized component of the MW field in a plane perpendicular to the NV axis. Measuring $\Omega^\pm$ thus allows us to directly determine the amplitude of the driving MW magnetic field in a circularly polarized basis.

In the following, we demonstrate imaging of the σ_--component of the MW magnetic field ($\omega_{\text{MW}}/2\pi = 2.825$ GHz) generated by the stripline. To that end, we tune the sensing frequency $\omega^-/2\pi = (D_{gs} - \gamma_{\text{NV}} B_z)$ of the $m_s = 0 \rightarrow m_s = -1$ transition via a static magnetic field B_z and measure the MW magnetic field while scanning the NV center across the stripline.
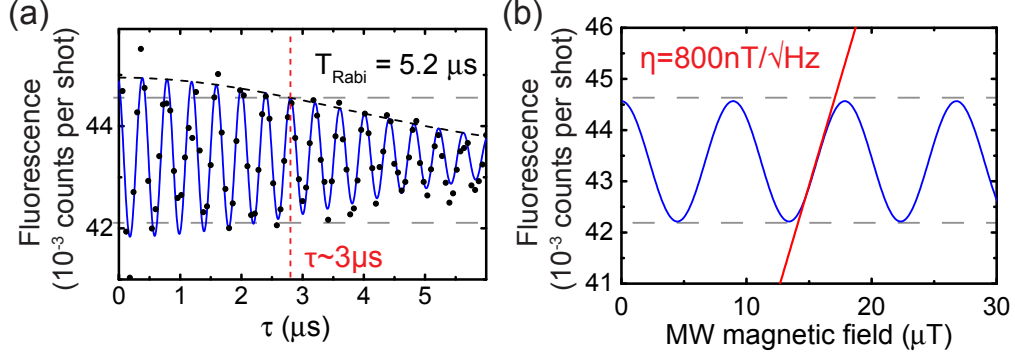
Figure 4.4: (a) Rabi oscillations of the NV spin, driven by a circularly polarized MW magnetic field $B_{MW}^{\pm}$ at $\omega_{MW}/2\pi = 2.825\,\text{GHz}$ (in a static magnetic field of $1.6\,\text{mT}$). The black dots are experimental data and the blue solid line corresponds to a fit (see Appendix B). The Rabi frequency extracted from the fit enables the determination of the MW magnetic field $B_{MW} = \omega_{MW}/2\pi\gamma_{NV} = 88\,\mu\text{T}$. (b) The magnetic field dependent signal for a fixed evolution time $\tau \sim 3\,\mu\text{s}$ (indicated by the gray dashed lines). By fixing τ for Iso-B MW imaging we can map the magnetic field onto changes in fluorescence. In this case the oscillations of the magnetic field correspond to the fringes in Fig. 4.5. Additionally, the maximum slope of this signal allows us to determine the sensitivity of $\eta = 800\,\text{nT}/\sqrt{\text{Hz}}$ (see Appendix B).

4.3.1 Microwave iso-B-imaging

For measuring the MW magnetic field profile of our stripline geometry, we first image the equi-magnetic field lines of constant amplitude B_{MW}^{-}. For a fixed microwave pulse length τ_0, the accumulated phase (pulse area) in the Rabi oscillation and thus the population difference between $m_s = 0$ and $m_s = -1$ depends on the local microwave magnetic field B_{MW}^{-} (Fig. 4.4 (b)). While scanning the NV spin at a distance h_{NV} over the stripline, we monitor variations of the microwave magnetic field via changes in the NV fluorescence I (Fig. 4.5). Analogously to DC iso-B imaging, we correct for fluorescence changes arising from potential near field effects [37, 82, 83] by simultaneously recording the bare fluorescence rate I_0 of the $m_s = 0$ state and generating the differential fluorescence.

Figure 4.5 (a) shows the differential fluorescence recorded in the xy plane in AFM contact (corresponding to a constant distance of the NV spin above the stripline) with $\tau_0 = 300\,\text{ns}$. Each bright fringe corresponds to an integer multiple of 2π of accumulated phase of the NV Rabi oscillations. Consequently, the bright fringes represent isofield lines of B_{MW}^{-}, which are spaced by $1/\gamma_{NV}\tau_0 = 120\,\mu\text{T}$. To avoid ambiguities in assigning the correct value of B_{MW}^{-} to each measured field line, we separately measured B_{MW}^{-} for several reference lines, by placing the NV at certain positions and measuring the full Rabi oscillations. The references for $B_{MW}^{-} = 360, 600$ and $840\,\mu\text{T}$ are highlighted in yellow, orange and red, respectively in Fig. 4.5 (a).
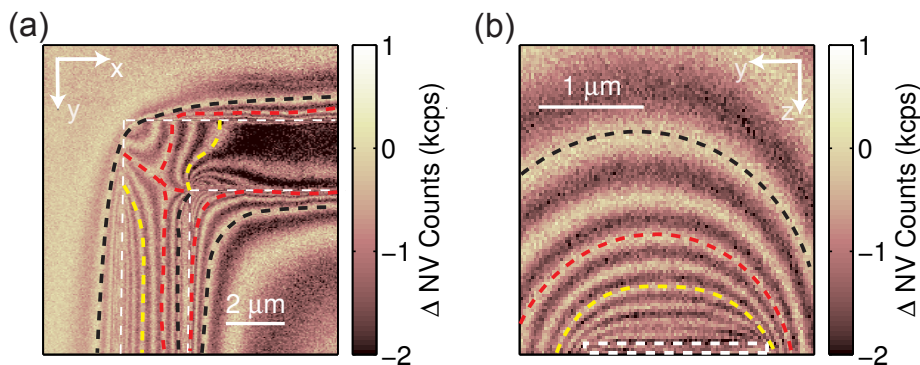
Figure 4.5: Three dimensional iso-field image of a MW magnetic field (a) in the xy plane, at a distance above the stripline and (b) in the zy plane. The measurements were performed at a frequency $\omega_{MW}/2\pi = 2.825\,\mathrm{GHz}$. The white dashed lines outline the stripline, whereas the dashed black, red and yellow lines highlight reference isofield lines for $B_{MW}^- = 360, 600$ and $840\,\mu T$, respectively. The MW magnetic change between adjacent fringes amount to $\Delta B_{MW}^- = 120\,\mathrm{nT}$, as set be the $\tau_0 = 300\,\mathrm{ns}$.

The versatility and stability of our microscope allows us to also image MW magnetic fields in all three dimensions and in particular as a function of distance to the sample. To that end, we release AFM force feedback and record the MW magnetic field image by scanning the sample in a plane orthogonal to the MW current (Fig. 4.5 (b)). In analogy to Fig. 4.5 (a), we attribute a MW magnetic field amplitude to each isofield line as shown in Fig. 4.5 (b).

4.3.2 Full field imaging

While providing a fast and straightforward method for nanoscale imaging of MW magnetic fields, our method for iso-field imaging suffers from limitations in regions of high magnetic field gradients. This is particularly appreciable near the edges of our stripline, where individual field lines are hard to distinguish and identification of the measured isofield lines becomes intractable. In order to overcome this limitation, we extended our imaging capabilities to directly determine B_{MW}^- at each point throughout the scan (Fig. 4.6). For this, we measured NV Rabi oscillations at each pixel in the scan range and determined B_{MW}^- by a sinusodial fit to each of these traces (see Appendix B). Figure 4.6 (a) depicts the resulting image of B_{MW}^- measured above the corner of the stripline imaged in Fig. 4.5 (a). The measured MW magnetic field map is in excellent agreement with the distribution of the MW magnetic field determined using finite element simulations (Fig. 4.6 (b)). For the simulation of the MW magnetic field distribution we used the distance and orientation of the NV spin determined from the analytical fit of the measured linecut discussed in Sec. 4.4.
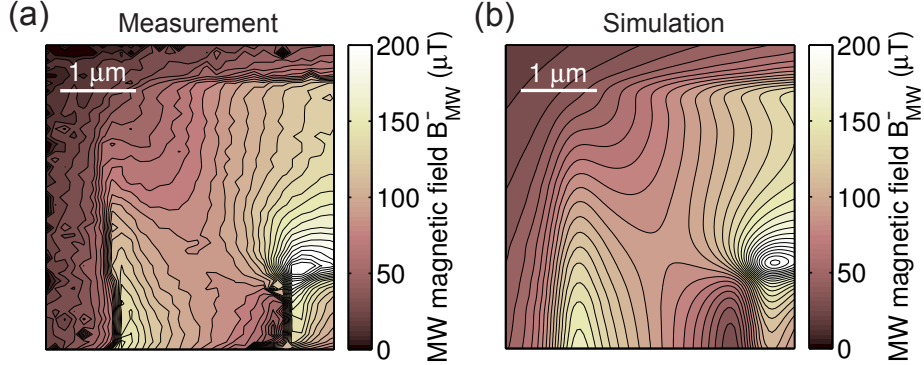
Figure 4.6: Full, quantitative field mapping. (a) Measured 2D spatial distribution of the MW magnetic field amplitude B_{MW}^- and (b) simulated spatial distribution obtained by a finite element computation of a 50 Ω stripline.

4.4 Spatial resolution and current sensitivity

The determination of the NV-to-sample distance h_{NV} is essential for various aspects of NV-based sensing, as discussed in Chap. 2. First and foremost, h_{NV} sets the spatial resolution of scanning NV magnetometry. Moreover, the distance links the MW current to the MW magnetic field seen by the NV spin and therefore sets the sensitivity with which a MW current can be detected.

To determine the NV-to-sample distance we recorded linecuts of the MW magnetic field on the straight part of the stripline (far away from the corner), where the current can be assumed to be constant. The stray field at these positions can be described by the analytical function $B_{MW}^-(h_{NV}, J, \varphi, \theta)$, with $h_{NV}, J, \varphi, \theta$ as free parameters, as derived in Sec. 4.2. The resulting fits (blue lines in Fig. 4.7 (a) and (b)) are in excellent agreement with the experimental data and yield an NV orientation of $\theta = 49 \pm 1°$ and $\varphi = 104 \pm 2°$, a MW current density of $J = 3.9 \pm 0.05 \, \text{mA}/\mu\text{m}^2$ and a distance of $h_{NV} = 25 \pm 5 \, \text{nm}$[5] for Fig. 4.7 (a). For Fig. 4.7 (b) we extract an orientation of $\theta = 48 \pm 1°$ and $\varphi = 11 \pm 1°$, a MW current density of $J = 4.05 \pm 0.05 \, \text{mA}/\mu\text{m}^2$ and a distance of $h_{NV} = 64 \pm 8 \, \text{nm}$. In addition, we have numerically computed, using a finite element simulation, the MW magnetic field amplitude and fitted this field amplitude to the measurements (orange lines in Fig. 4.7 (a) and (b)). This fitting yields $\theta = 47°$ and $\varphi = 103°$, $J = 3.9 \, \text{mA}/\mu\text{m}^2$ and $h_{NV} = 20 \, \text{nm}$ for Fig. 4.7 (a) and $\theta = 47°$ and $\varphi = 13°$, $J = 3.9 \, \text{mA}/\mu\text{m}^2$ and $h_{NV} = 70 \, \text{nm}$ for Fig. 4.7 (b). This values are almost identical to the analytical fit parameters, verifying the assumption of an infinitesimal thin wire. Note that for the data sets presented in Fig. 4.7 (b), we find $d = 64 \pm 5$ nm, significantly larger than the value of $h_{NV} = 25 \pm 5$ nm (Fig. 4.7 (a)). We attribute this discrepancy to contaminations on the diamond tip that has accumulated throughout the course of our experiments. Removing these

---

[5]h_{NV} is distance between the NV center and the top surface. For the determination half of the thickness of the stripline is subtracted from the modeled distance to an infinitely thin stripline

contaminants (see Chap. 2) or working with a fresh tip should restore h_{NV} to its original value.
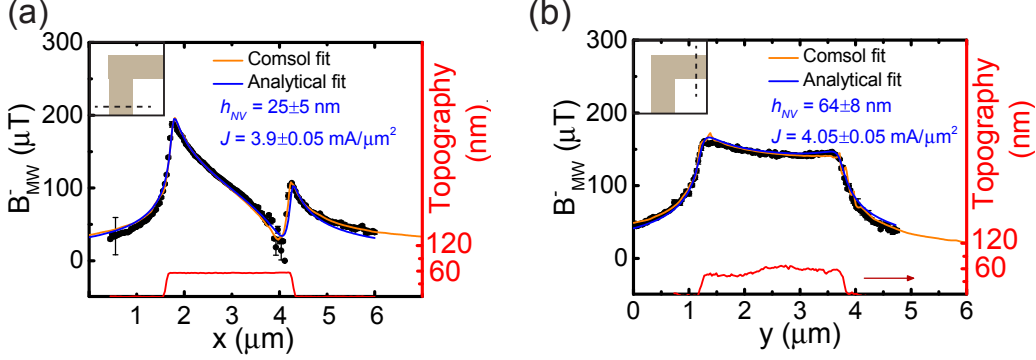
Figure 4.7: MW magnetic field $B'_{-,MW}$ (black dots) and topography (red solid line) recorded during two different linescans at the bottom (a) and top (b) of the stripline. The inset shows the stripline outlined in grey. The black dotted line depicts the direction of the respective linescan. Black dots are the experimental data obtained from Rabi fits and the error bars correspond to the error of the Rabi fits. The blue lines correspond to the fit with the analytical function $B'_{-,MW}(h_{NV}, J, \varphi, \theta)$ (see text). The extracted NV-to-sample distance and current density are indicated in blue. The red lines are the fits with a numerical simulation, which yield similar fitting parameters [17].

By imaging the MW magnetic field over a stripline using scanning NV magnetometry, we can estimate the MW current density in the stripline and determine the orientation of the NV spin within $2°$. Furthermore, we can estimate the distance between the NV and the MW current with an accuracy of a few nanometers (Fig. 4.7) [17]. This distance defines the resolution of scanning NV magnetometry, which is ~ 25 nm for the presented measurements. Moreover, h_{NV}, together with the magnetic field sensitivity of $\eta = 800\,\mathrm{nT}/\sqrt{\mathrm{Hz}}$ (see Appendix B), allows us to determine the MW current sensitivity of our NV magnetometer of $\sim 300\,\mathrm{nA}/\sqrt{\mathrm{Hz}}$ for an infinitely thin, current-carrying wire.

4.5 Conclusion

In conclusion, we have established scanning NV magnetometry as a valuable resource to sensitively detect and image MW magnetic fields on the nanoscale. Our results indicate an imaging resolution of ~ 25 nm together with a shot noise limited MW magnetic field sensitivity of $800\,\mathrm{nT}/\sqrt{\mathrm{Hz}}$. This results in a sensitivity to the generating currents of a few $\mathrm{nA}/\sqrt{\mathrm{Hz}}$ at frequencies $\sim 3\,\mathrm{GHz}$. Extending the bandwidth of detection to the range above $20\,\mathrm{GHz}$ can be achieved by placing our microscope in a sufficiently strong magnetic field [52]. Detection at such high frequencies would have a profound impact for applications in MW device characterization, as currently

available field imaging techniques cannot operate in this frequency range [157]. It should be noted that detection of microwave fields through Rabi oscillations has also been implemented for ^{87}Rb vapor cells [154, 151, 152, 153]. Such devices operate with tens of μm spatial resolution over a mm to cm detection window [158] and thus provide a complementary wide field imaging tool to our NV scanning magnetometers, which achieves nanoscale spatial resolution over a tens of μm detection window.

Chapter 5

Summary and Outlook

Scanning NV magnetometry is an emerging sensing technology which allows to probe magnetic fields on the nanoscale. In this thesis a highly sensitive scanning NV magnetometer was developed, characterized and its potential for probing magnetic fields was demonstrated in two applications. The excellent performance of our magnetometer enabled the study of the small stray field of an antiferromagnet and the imaging of microwave magnetic fields with unprecedented spatial resolution. Here, we summarize the major results of this thesis and outline research areas, where the sensing and imaging capabilities of NV magnetometry will allow to explore new physics.

In this work we implemented a procedure to fabricate single-crystal, all-diamond scanning probes with the NV center placed in close proximity ($\sim 9\,\mathrm{nm}$) to the apex of the probe in order to achieve highest performance of our magnetometer. We developed a highly efficient and robust method for integrating the scanning probes into our setup, which allows us to image magnetic fields on the nanoscale [16]. We characterized the state-of-the-art performance of our scanning probe based NV magnetometer, which yields excellent sensitivities of $\eta_{\mathrm{DC}} \sim 750\,\mathrm{nT}/\sqrt{\mathrm{Hz}}$ for DC and $\eta_{\mathrm{AC}} \sim 114\,\mathrm{nT}/\sqrt{\mathrm{Hz}}$ for AC-magnetic fields combined with a resolution of $50\pm32\,\mathrm{nm}$. These characteristics illustrates the excellent imaging capabilities NV magnetometry offers.

First, we used our sensitive scanning NV magnetometer to image the stray field emanating from antiferromagnetic Cr_2O_3. Antiferromagnets (AFs) offer attractive properties, which are currently under investigation and have the potential to improve or even create new functionalities for spintronics and data storage devices [109, 108, 104]. However, it has proven difficult to analyze their magnetic structure due to the absence of an overall magnetic moment. In this thesis, we demonstrated that the small stray field, created by an asymmetry between the AF sub lattices at the surface, can be measured using scanning NV magnetometry. By imaging the stray field of a Cr_2O_3 film, we captured the underlying AF domain pattern. Furthermore, the performance of our magnetometer allowed us to monitor its evolution through the AF-to-paramagnetic phase transition. The presented measurements provide

evidence of local variations in the critical temperature T_{crit}, which we here imaged for the first time. Moreover, the quantitative nature of NV magnetometry allowed us to measure the surface moment density of Cr_2O_3 in ambient conditions. The measured moment density is reduced from the projected bulk value, which indicates a rearrangement of the spin at the surface. The presented experiments establish scanning NV magnetometry as excellent, new technique for measuring the stray field of AFs. This technique reveals the nanoscopic magnetic structure of materials, which will allow for the development of new, efficient devices for data storage.

In a second application, we quantitatively imaged the magnetic field generated by a high frequency (GHz) microwave (MW) current with a resolution of $\sim 25\,\mathrm{nm}$. These experiments demonstrate our scanning NV magnetometer's ability to measure and image MW magnetic fields with a unprecedented spatial resolution, which may have a profound impact on MW device characterization. Moreover, this technique can in the future be applied to study excitations in nanomagnetic systems, such as spins waves, which in quantized description are referred to as magnons. Generally, Spin waves are considered as promising, new data carriers for next generation computing devices because of their nanometer wavelength, potentially high frequencies, dissipation free transfer of information and the variety of different linear and non-linear couplings in magnetic materials and interfaces [159]. In particular, spin waves at GHz frequencies are currently being investigated due to potential telecommunication applications [159, 160]. Recent experiments have demonstrated that spin waves at these frequencies can be addressed via the described MW detection [161] or using non-resonant detection schemes [161, 162]. In these first experiments, stationary bulk NV centers were employed, which restricts the achievable resolution. Thus, spin wave imaging with nanoscale resolution still remains an outstanding challenge. Combining these detection schemes with a scanning probe technique is therefore an exciting development that will allow for real space imaging of nanoscale spin waves with an unprecedented resolution. This will furthermore help to analyze and study the interaction of spin waves, enabling the development of new types of computing schemes [159].

These first applications already indicate the potential scanning NV magnetometry offers. However, there are many other emerging research areas in which NV magnetometry can act as a useful tool. For example, spin textures, such as domain walls and skyrmions, have recently attracted a lot of attention as tools to store information and due to possible applications in racetrack memories [145, 167, 168] and data processing [169, 170]. To exploit the full potential of these systems for next generation devices, understanding their dynamics is essential. Scanning NV magnetometry was recently used to reveal the internal structure of domain walls and skyrmions [23, 95] and study the dynamics of domain walls [171]. These first experiments illustrate the potential of scanning NV magnetometry for analyzing spin structures in ferromagnetic, ferrimagnetic or AF materials, which will help to identify the most suitable systems and thereby pave the way towards new devices for data storage and data processing.

(a) Spin Waves
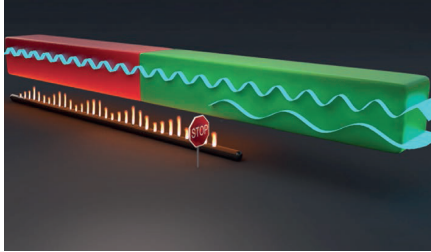
(b) Spin Textures
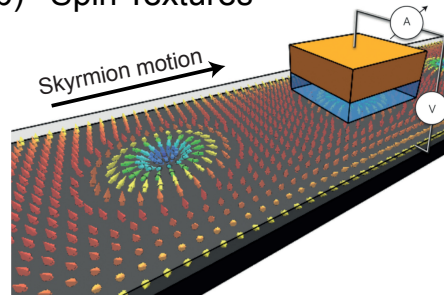
(c) Interface Magnetism
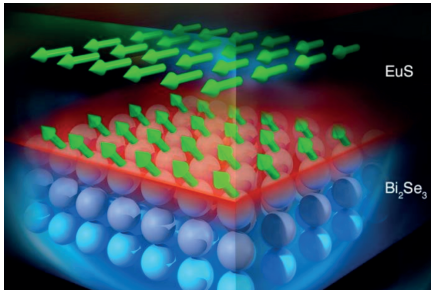
(d) Charge Transport
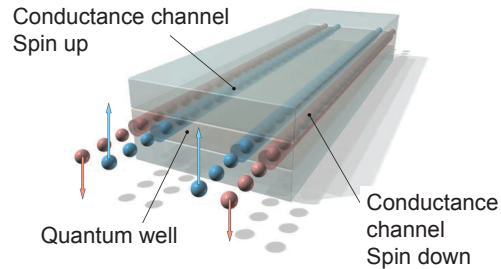
Figure 5.1: Potential future applications. (a) Scanning NV magnetometry offers a high sensitivity at $\sim$ GHz frequencies combined with a superior resolution, that can be applied to study spin waves. Figure shows the concept of a heated magnonic crystal. Reprinted by permission from Macmillan Publishers Ltd: Nature Physics [160], copyright (2015). (b) The dynamics of spin textures can be probed by measuring their stray fields, which will help to design next generation of dense storage devices. Figure represents a skyrmion racetrack. Reprinted by permission from Macmillan Publishers Ltd: Nature Nanotechnology [163], copyright (2015). (c) Interface interactions and interface states can be analyzed by studying their magnetic signatures. Figure illustrates the ferromagnetic topological insulating state of Bi_2Se_3-EuS bilayer [164, 165]. Image taken from [164], image credit: ORNL/Jill Hemman. (d) Sensitive stray field imaging allows to detect charge transport. By mapping the trajectory of the charge carriers, local transport properties can be probed. Figure illustrates edge states in topological insulator. From [166]. Reprinted with permission from AAAS.

Interface magnetism is another emerging area for which NV magnetometry is an attractive tool. Complex material interfaces can exhibit new types of interactions that lead to different phenomena and can ultimately result in new, exotic states. Examples include the recently observed high temperature ferromagnetic topological insulator state (see Fig. 5.1, [165]), high temperature superconductivity [172] and an exotic state, where superconductivity coexists with ferromagnetism [173]. Analyzing the magnetic signatures of these new phases using scanning NV magnetometry

provides new information that will help to control these new magnetic states by understanding their interactions.

A further research area is the imaging of stray fields resulting from charge transport. Exotic materials such as topological insulators or graphene are currently being investigated because their charge carriers can be transmitted along edge states [166] or snake trajectories [174]. The scattering properties along these trajectories are distinct from the bulk, which can result in spin selective, dissipation-less transmission [166, 175, 176]. Nanoscale detection of the current therefore has a profound impact on studying the scattering properties of these channels. Being able to externally control these trajectories [177, 178], promises new opportunities for efficient communication technologies that can be analyzed by non-invasively measuring the magnetic stray field using scanning NV magnetometry. Because most of these phenomena occur only in cryogenic conditions, we have also developed a scanning NV magnetometer, which can be operated in such environments, and proved its performance by imaging the stray field from vortices in a superconductor [15]. Thus, such cryogenic scanning NV magnetometry can in the future allow for local measurements of charge (and spin) transport in these exotic materials.

All of these future applications are enabled by the excellent sensing capabilities of scanning NV magnetometry. Sensing based on the NV center is quantitative, minimally invasive and can be performed over a wide range of temperatures and frequencies. Although the state-of-the-art performance already allows a variety of different physical problems to be probed, the performance of scanning NV magnetometry still allows for improvements. The resolution is currently limited by potential contamination of the scanning probe or additional forces at ambient conditions. Overcoming these limitations, as discussed in Chap. 2, will allow for imaging with a resolution that is defined by the depth of the NV center in the diamond scanning probe. New routes to improve the current depth of $\sim 9\,\mathrm{nm}$ by creating even more shallow NV centers without deteriorating the NV centers sensing capabilities are currently being investigated [93, 87, 25]. This may enable resolutions of $\sim 1\,\mathrm{nm}$ to be reached. Additionally, improved scanning probe geometries for highly efficient light extraction, that also optimize the sensitivity (see Chap. 2) are currently being investigated. This will potentially allow for imaging with sensitivities below $1\mathrm{nT}/\sqrt{\mathrm{Hz}}$, which will enable us to measure the magnetic moments of single electrons and atoms, flux quanta and magnons and thereby study the discussed phenomena on the quantum level.

Bibliography

[1] D. Rugar, R. Budakian, H. Mamin, and B. Chui, *Single spin detection by magnetic resonance force microscopy*, Nature **430**, 329 (2004).

[2] M. Grinolds, S. Hong, P. Maletinsky, L. Luan, M. Lukin, R. Walsworth, and A. Yacoby, *Nanoscale magnetic imaging of a single electron spin under ambient conditions*, Nature Phys. **9**, 2145 (2013).

[3] D. Vasyukov, Y. Anahory, L. Embon, D. Halbertal, J. Cuppens, L. Neeman, A. Finkler, Y. Segev, Y. Myasoedov, M. L. Rappaport *et al.*, *A scanning superconducting quantum interference device with single electron spin sensitivity*, Nature Nanotech. **8**, 639 (2013).

[4] C. Degen, *Microscopy with single spins*, Nature Nanotech. **3**, 643 (2008).

[5] E. O. Schäfer-Nolte, *Development of a diamond-based scanning probe spin sensor operating at low temperature in ultra high vacuum*, Ph.D. thesis, Universität Stuttgart (2014).

[6] G. Boero, M. Demierre, P.-A. Besse, and R. Popovic, *Micro-hall devices: performance, technologies and applications*, Sens. Actuat. A **106**, 314 (2003).

[7] J. Kirtley, M. Ketchen, K. Stawiasz, J. Sun, W. Gallagher, S. Blanton, and S. Wind, *High-resolution scanning squid microscope*, Appl. Phys. Lett. **66**, 1138 (1995).

[8] M. E. Huber, N. C. Koshnick, H. Bluhm, L. J. Archuleta, T. Azua, P. G. Björnsson, B. W. Gardner, S. T. Halloran, E. A. Lucero, and K. A. Moler, *Gradiometric micro-squid susceptometer for scanning measurements of mesoscopic samples*, Rev. Sci. Instrum. **79**, 053704 (2008).

[9] H. Mamin, R. Budakian, B. Chui, and D. Rugar, *Detection and manipulation of statistical polarization in small spin ensembles*, Phys. Rev. Lett. **91**, 207604 (2003).

[10] H. J. Mamin, M. Poggio, C. L. Degen, and D. Rugar, *Nuclear magnetic resonance imaging with 90-nm resolution*, Nature Nanotech. **2**, 301 (2007).

[11] H. J. Mamin, T. H. Oosterkamp, M. Poggio, C. L. Degen, C. T. Rettner, and D. Rugar, *Isotope-selective detection and imaging of organic nanolayers*, Nano Lett. **9**, 3020 (2009).

[12] K. C. Fong, M. R. Herman, P. Banerjee, D. V. Pelekhov, and P. C. Hammel, *Spin lifetime in small ensembles of electron spins measured by magnetic resonance force microscopy*, Phys. Rev. B **84**, 220405 (2011).

[13] B. K. Ofori-Okai, S. Pezzagna, K. Chang, M. Loretz, R. Schirhagl, Y. Tao, B. A. Moores, K. Groot-Berning, J. Meijer, and C. L. Degen, *Spin properties of very shallow nitrogen vacancy defects in diamond*, Phys. Rev. B **86**, 081406 (2012).

[14] H. J. Mamin, M. Kim, M. H. Sherwood, C. T. Rettner, K. Ohno, D. D. Awschalom, and D. Rugar, *Nanoscale nuclear magnetic resonance with a nitrogen-vacancy spin sensor*, Science **339**, 557 (2013).

[15] L. Thiel, D. Rohner, M. Ganzhorn, P. Appel, E. Neu, B. Müller, R. Kleiner, D. Koelle, and P. Maletinsky, *Quantitative nanoscale vortex imaging using a cryogenic quantum magnetometer*, Nature Nanotech. **11**, 677 (2016).

[16] P. Appel, E. Neu, M. Ganzhorn, A. Barfuss, M. Batzer, M. Gratz, A. Tschöpe, and P. Maletinsky, *Fabrication of all diamond scanning probes for nanoscale magnetometry*, Rev. Sci. Instrum. **87**, 063703 (2016).

[17] P. Appel, M. Ganzhorn, E. Neu, and P. Maletinsky, *Nanoscale microwave imaging with a single electron spin in diamond*, New J. Phys. **17**, 112001 (2015).

[18] D. Drung, C. Assmann, J. Beyer, A. Kirste, M. Peters, F. Ruede, and T. Schurig, *Highly sensitive and easy-to-use squid sensors*, IEEE Trans. Appl. Supercond. **17**, 699 (2007).

[19] G. Balasubramanian, P. Neumann, D. Twitchen, M. Markham, R. Kolesov, N. Mizuochi, J. Isoya, J. Achard, J. Beck, J. Tissler *et al.*, *Ultralong spin coherence time in isotopically engineered diamond*, Nature Mater. **8**, 383 (2009).

[20] P. Maletinsky, S. Hong, M. S. Grinolds, B. Haussmann, M. D. Lukin, R. L. Walsworth, M. Loncar, and A. Yacoby, *A robust scanning diamond sensor for nanoscale imaging with single nitrogen-vacancy centres*, Nature Nanotech. **7**, 320 (2012).

[21] L. Rondin, J.-P. Tetienne, P. Spinicelli, C. Dal Savio, K. Karrai, G. Dantelle, A. Thiaville, S. Rohart, J.-F. Roch, and V. Jacques, *Nanoscale magnetic field mapping with a single spin scanning probe magnetometer*, Appl. Phys. Lett. **100**, 153118 (2012).

[22] L. Rondin, J. Tetienne, S. Rohart, A. Thiaville, T. Hingant, P. Spinicelli, J.-F. Roch, and V. Jacques, *Stray-field imaging of magnetic vortices with a single diamond spin*, Nature Comm. **4**, 2279 (2013).

[23] J.-P. Tetienne, T. Hingant, L. Martinez, S. Rohart, A. Thiaville, L. H. Diez, K. Garcia, J.-P. Adam, J.-V. Kim, J.-F. Roch, J.-F. Miron, G. Gaudin, L. Vila, B. Ocker, D. Ravelosona, and V. Jacques, *The nature of domain walls in ultrathin ferromagnets revealed by scanning nanomagnetometry*, Nature Comm. **6**, 6733 (2015).

[24] P. Appel, B. J. Shields, T. Kosub, D. Makarov, and P. Maletinsky, *Real space stray field imaging of antiferromagnets*, to be published (2017).

[25] K. Ohno, F. J. Heremans, L. C. Bassett, B. A. Myers, D. M. Toyli, A. C. B. Jayich, C. J. Palmstrom, and D. D. Awschalom, *Engineering shallow spins in diamond with nitrogen delta-doping*, Appl. Phys. Lett. **101**, 082413 (2012).

[26] C. Schreyvogel, M. Wolfer, H. Kato, M. Schreck, and C. E. Nebel, *Tuned nv emission by in-plane al-Schottky junctions on hydrogen terminated diamond*, Sci. Rep. **4**, 03634 (2014).

[27] M. V. Hauf, B. Grotz, B. Naydenov, M. Dankerl, S. Pezzagna, J. Meijer, F. Jelezko, J. Wrachtrup, M. Stutzmann, F. Reinhard, and J. A. Garrido, *Chemical control of the charge state of nitrogen-vacancy centers in diamond*, Phys. Rev. B **83**, 081304 (2011).

[28] B. Grotz, M. V. Hauf, M. Dankerl, B. Naydenov, S. Pezzagna, J. Meijer, F. Jelezko, J. Wrachtrup, M. Stutzmann, F. Reinhard, and J. A. Garrido, *Charge state manipulation of qubits in diamond*, Nature Comm. **3**, 729 (2012).

[29] N. Aslam, G. Waldherr, P. Neumann, F. Jelezko, and J. Wrachtrup, *Photo-induced ionization dynamics of the nitrogen vacancy defect in diamond investigated by single-shot charge state detection*, New J. Phys. **15**, 013064 (2013).

[30] B. J. Shields, Q. P. Unterreithmeier, N. P. de Leon, H. Park, and M. D. Lukin, *Efficient readout of a single spin state in diamond via spin-to-charge conversion*, Phys. Rev. Lett. **114**, 136402 (2015).

[31] V. Acosta, *Optical magnetometry with nitrogen-Vacancy centers in diamond*, Ph.D. thesis, University of California, Berkeley (2011).

[32] A. Gruber, A. Dräbenstedt, C. Tietz, L. Fleury, J. Wrachtrup, and C. von Borczyskowski, *Scanning confocal optical microscopy and magnetic resonance on single defect centers*, Science **276**, 2012 (1997).

[33] J. Maze, A. Gali, E. Togan, Y. Chu, A. Trifonov, E. Kaxiras, and M. Lukin, *Properties of nitrogen-vacancy centers in diamond: the group theoretic approach*, New J. Phys. **13**, 025025 (2011).

[34] A. Gali, M. Fyta, and E. Kaxiras, *Ab initiosupercell calculations on nitrogen-vacancy center in diamond: Electronic structure and hyperfine tensors*, Phys. Rev. B **77**, 155206 (2008).

[35] M. W. Doherty, N. B. Manson, P. Delaney, F. Jelezko, J. Wrachtrup, and L. C. Hollenberg, *The nitrogen-vacancy colour centre in diamond*, Phys. Rep. **528**, 1 (2013).

[36] L. Robledo, H. Bernien, I. van Weperen, and R. Hanson, *Control and coherence of the optical transition of single nitrogen vacancy centers in diamond*, Phys. Rev. Lett. **105**, 177403 (2010).

[37] J.-P. Tetienne, L. Rondin, P. Spinicelli, M. Chipaux, T. Debuisschert, J.-F. Roch, and V. Jacques, *Magnetic-field-dependent photodynamics of single nv defects in diamond: an application to qualitative all-optical magnetic imaging*, New J. Phys. **14**, 103033 (2012).

[38] L. Rondin, J.-P. Tetienne, T. Hingant, J.-F. Roch, P. Maletinsky, and V. Jacques, *Magnetometry with nitrogen-vacancy defects in diamond*, Rep. Prog. Phys. **77**, 056503 (2014).

[39] V. M. Acosta, A. Jarmola, E. Bauch, and D. Budker, *Optical properties of the nitrogen-vacancy singlet levels in diamond*, Phys. Rev. B **82**, 201202 (2010).

[40] J. Wrachtrup and F. Jelezko, *Processing quantum information in diamond*, Journ. Phys.: Cond. Matter **18**, S807 (2006).

[41] G. D. Fuchs, V. V. Dobrovitski, R. Hanson, A. Batra, C. D. Weis, T. Schenkel, and D. D. Awschalom, *Excited-state spectroscopy using single spin manipulation in diamond*, Phys. Rev. Lett. **101**, 117601 (2008).

[42] C. P. Slichter, *Principles of Magnetic Resonance*, (Springer-Verlag Berlin Heidelberg) (1990).

[43] I. Jakobi, P. Neumann, Y. Wang, D. B. R. Dasari, F. El Hallak, M. A. Bashir, M. Markham, A. Edmonds, D. Twitchen, and J. Wrachtrup, *Measuring broadband magnetic fields on the nanoscale using a hybrid quantum register*, Nature Nanotech. **12**, 67 (2016).

[44] A. Dréau, M. Lesik, L. Rondin, P. Spinicelli, O. Arcizet, J.-F. Roch, and V. Jacques, *Avoiding power broadening in optically detected magnetic resonance of single NV defects for enhanced dc magnetic field sensitivity*, Phys. Rev. B **84**, 195204 (2011).

[45] J. Taylor, P. Cappellaro, L. Childress, L. Jiang, D. Budker, P. Hemmer, A. Yacoby, R. Walsworth, and M. Lukin, *High-sensitivity diamond magnetometer with nanoscale resolution*, Nature Phys. **4**, 810 (2008).

[46] T. Rosskopf, A. Dussaux, K. Ohashi, M. Loretz, R. Schirhagl, H. Watanabe, S. Shikata, K. Itoh, and C. Degen, *Investigation of surface magnetic noise by shallow spins in diamond*, Phys. Rev. Lett. **112**, 147602 (2014).

[47] Y. Romach, C. Müller, T. Unden, L. J. Rogers, T. Isoda, K. M. Itoh, M. Markham, A. Stacey, J. Meijer, S. Pezzagna, B. Naydenov, L. McGuinness, N. Bar-Gill, and F. Jelezko, *Spectroscopy of surface-induced noise using shallow spins in diamond*, Phys. Rev. Lett. **114**, 017601 (2015).

[48] A. Jarmola, V. M. Acosta, K. Jensen, S. Chemerisov, and D. Budker, *Temperature- and magnetic-field-dependent longitudinal spin relaxation in nitrogen-vacancy ensembles in diamond*, Phys. Rev. Lett. **108**, 197601 (2012).

[49] B. A. Myers, A. Das, M. C. Dartiailh, K. Ohno, D. D. Awschalom, and A. C. Bleszynski Jayich, *Probing surface noise with depth-calibrated spins in diamond*, Phys. Rev. Lett. **113**, 027602 (2014).

[50] A. Barfuss, J. Teissier, E. Neu, A. Nunnenkamp, and P. Maletinsky, *Strong mechanical driving of a single electron spin*, Nature Phys. **11**, 820 (2015).

[51] L. Childress, M. Dutt, J. Taylor, A. Zibrov, F. Jelezko, J. Wrachtrup, P. Hemmer, and M. Lukin, *Coherent dynamics of coupled electron and nuclear spin qubits in diamond*, Science **314**, 281 (2006).

[52] V. Stepanov, F. H. Cho, C. Abeywardana, and S. Takahashi, *High-frequency and high-field optically detected magnetic resonance of nitrogen-vacancy centers in diamond*, Appl. Phys. Lett. **106**, 063111 (2015).

[53] L. M. Pham, D. Le Sage, P. L. Stanwix, T. K. Yeung, D. Glenn, A. Trifonov, P. Cappellaro, P. Hemmer, M. D. Lukin, H. Park, A. Yacoby, and R. Walsworth, *Magnetic field imaging with nitrogen-vacancy ensembles*, New J. Phys. **13**, 045021 (2011).

[54] S. Steinert, F. Ziem, L. T. Hall, A. Zappe, M. Schweikert, N. Götz, A. Aird, G. Balasubramanian, L. Hollenberg, and J. Wrachtrup, *Magnetic spin imaging under ambient conditions with sub-cellular resolution*, Nature Comm. **4**, 1607 (2013).

[55] D. A. Simpson, J.-P. Tetienne, J. M. McCoey, K. Ganesan, L. T. Hall, S. Petrou, R. E. Scholten, and L. C. L. Hollenberg, *Magneto-optical imaging of thin magnetic films using spins in diamond*, Sci. Rep. **6**, 22797 (2016).

[56] M. Pelliccione, B. A. Myers, L. M. A. Pascal, A. Das, and A. C. Bleszynski Jayich, *Two-dimensional nanoscale imaging of gadolinium spins via scanning probe relaxometry with a single spin in diamond*, Phys. Rev. Appl. **2**, 054014 (2014).

[57] D. Schmid-Lorch, T. Häberle, F. Reinhard, A. Zappe, M. Slota, L. Bogani, A. Finkler, and J. Wrachtrup, *Relaxometry and dephasing imaging of superparamagnetic magnetite nanoparticles using a single qubit*, Nano Lett. **15**, 4942 (2015).

[58] G. Balasubramanian, I. Chan, R. Kolesov, M. Al-Hmoud, J. Tisler, C. Shin, C. Kim, A. Wojcik, P. Hemmer, A. Krueger, T. Hanke, A. Leitenstorfer, R. Bratschitsch, F. Jelezko, and J. Wrachtrup, *Nanoscale imaging magnetometry with diamond spins under ambient conditions*, Nature **455**, 648 (2008).

[59] C. Bradac, T. Gaebel, N. Naidoo, M. J. Sellars, J. Twamley, L. J. Brown, A. S. Barnard, T. Plakhotnik, A. V. Zvyagin, and J. R. Rabeau, *Observation and control of blinking nitrogen-vacancy centres in discrete nanodiamonds*, Nature Nanotech. **5**, 345 (2010).

[60] S. Morita, F. J. Giessibl, and R. Wiesendanger, *Noncontact Atomic Force Microscopy, Volume 2*, (Springer International Publishing) (2009).

[61] S. Morita, F. J. Giessibl, E. Meyer, and R. Wiesendanger, *Noncontact Atomic Force Microscopy, Volume 3*, (Springer International Publishing) (2015).

[62] K. Karrai and R. D. Grober, *Piezoelectric tip-sample distance control for near field optical microscopes*, Appl. Phys. Lett. **66**, 1842 (1995).

[63] *See http://www.e6cvd.com/ for more information.*

[64] *See www.ddk.com or www.almax-easylab.com for more information.*

[65] J. Hird and J. Field, *Diamond polishing*, Proc. R. Soc. Lond. A **460**, 3547 (2004).

[66] T. Schuelke and T. A. Grotjohn, *Diamond polishing*, Diam. Relat. Mater. **32**, 17 (2013).

[67] P.-N. Volpe, P. Muret, F. Omnes, J. Achard, F. Silva, O. Brinza, and A. Gicquel, *Defect analysis and excitons diffusion in undoped homoepitaxial diamond films after polishing and oxygen plasma etching*, Diam. Relat. Mater. **18**, 1205 (2009).

[68] I. Friel, S. Clewes, H. Dhillon, N. Perkins, D. Twitchen, and G. Scarsbrook, *Control of surface and bulk crystalline quality in single crystal diamond grown by chemical vapour deposition*, Diam. Relat. Mater. **18**, 808 (2009).

[69] M. Naamoun, A. Tallaire, F. Silva, J. Achard, P. Doppelt, and A. Gicquel, *Etch-pit formation mechanism induced on HPHT and CVD diamond single crystals by H_2/O_2 plasma etching treatment*, Phys. Status Solidi A **209**, 1715 (2012).

[70] Y. Tao, J. Boss, B. Moores, and C. Degen, *Single-crystal diamond nanomechanical resonators with quality factors exceeding one million*, Nature Commun. **5**, 3638 (2014).

[71] *Estimated using the software SRIM - the stopping range of ions in matter http://www.srim.org/.*

[72] Y. Chu, N. de Leon, B. Shields, B. Hausmann, R. Evans, E. Togan, M. J. Burek, M. Markham, A. Stacey, A. Zibrov, A. Yacoby, D. J. Twitchen, M. Loncar, H. Park, P. Maletinsky, and M. Lukin, *Coherent optical transitions in implanted nitrogen vacancy centers*, Nano Lett. **14**, 1982 (2014).

[73] S. Pezzagna, B. Naydenov, F. Jelezko, J. Wrachtrup, and J. Meijer, *Creation efficiency of nitrogen-vacancy centres in diamond*, New J. Phys. **12**, 065017 (2010).

[74] R. J. Hoekstra, M. J. Kushner, V. Sukharev, and P. Schoenborn, *Microtrenching resulting from specular reflection during chlorine etching of silicon*, J. Vac. Sci. Technol. B **16**, 2102 (1998).

[75] T. Babinec, B. Hausmann, M. Khan, Y. Zhang, J. Maze, P. Hemmer, and M. Loncar, *A diamond nanowire single-photon source*, Nature Nanotech. **5**, 195 (2010).

[76] E. Neu, P. Appel, M. Ganzhorn, J. Miguel-Sanchez, M. Lesik, V. Mille, V. Jacques, A. Tallaire, J. Achard, and P. Maletinsky, *Photonic nanostructures on (111)-oriented diamond*, Appl. Phys. Lett. **104**, 153108 (2014).

[77] C. Kurtsiefer, S. Mayer, P. Zarda, and H. Weinfurter, *Stable solid-state source of single photons*, Phys. Rev. Lett. **85**, 290 (2000).

[78] T. Klein, A. Laptev, A. Günther, P. Bender, A. Tschöpe, and R. Birringer, *Magnetic-field-dependent optical transmission of nickel nanorod colloidal dispersions*, J. Appl. Phys. **106**, 114301 (2009).

[79] S. Schrittwieser, F. Ludwig, J. Dieckhoff, T. Andreas, A. Günther, M. Richter, A. Huetten, H. Brueckl, and J. Schotter, *Direct protein detection in the sample solution by monitoring rotational dynamics of nickel nanorods*, Small **10**, 407 (2013).

[80] A. Tschöpe, K. Birster, B. Trapp, P. Bender, and R. Birringer, *Nanoscale rheometry of viscoelastic soft matter by oscillating field magneto-optical transmission using ferromagnetic nanorod colloidal probes*, J. Appl. Phys. **116**, 184305 (2014).

[81] T. Hingant, J.-P. Tetienne, L. J. Martínez, K. Garcia, D. Ravelosona, J.-F. Roch, and V. Jacques, *Measuring the magnetic moment density in patterned ultrathin ferromagnets with submicrometer resolution*, Phys. Rev. Appl. **4**, 014003 (2015).

[82] P. Anger, P. Bharadwaj, and L. Novotny, *Enhancement and quenching of single-molecule fluorescence*, Phys. Rev. Lett. **96** (2006).

[83] J. Tisler, T. Oeckinghaus, R. J. Söhr, R. Kolesov, R. Reuter, F. Reinhard, and J. Wrachtrup, *Single defect center scanning near-field optical microscopy on graphene*, Nano Lett. **13**, 3152 (2013).

[84] R. S. Schoenfeld and W. Harneit, *Real time magnetic field sensing and imaging using a single spin in diamond*, Phys. Rev. Lett. **106**, 030802 (2011).

[85] T. Häberle, D. Schmid-Lorch, K. Karrai, F. Reinhard, and J. Wrachtrup, *High-dynamic-range imaging of nanoscale magnetic fields using optimal control of a single qubit*, Phys. Rev. Lett **111**, 170801 (2013).

[86] S. Momenzadeh, R. Stoehr, F. Fávaro de Oliveira, A. Brunner, A. Denisenko, S. Yang, F. Reinhard, and J. Wrachtrup, *Nanoengineered diamond waveguide as a robust bright platform for nanomagnetometry using shallow nitrogen vacancy centers*, Nano Lett. **15**, 165 (2015).

[87] F. Fávaro de Oliveira, S. A. Momenzadeh, Y. Wang, M. Konuma, M. Markham, A. M. Edmonds, A. Denisenko, and J. Wrachtrup, *Effect of low-damage inductively coupled plasma on shallow nitrogen-vacancy centers in diamond*, Appl. Phys. Lett. **107**, 073107 (2015).

[88] I. Lovchinsky, A. O. Sushkov, E. Urbach, N. P. de Leon, S. Choi, K. De Greve, R. Evans, R. Gertner, E. Bersin, C. Müller, L. McGuinness, F. Jelezko, R. Walsworth, H. Park, and M. Lukin, *Nuclear magnetic resonance detection and spectroscopy of single proteins using quantum logic*, Science **351**, 836 (2016).

[89] S. Cui and E. L. Hu, *Increased negatively charged nitrogen-vacancy centers in fluorinated diamond*, Appl. Phys. Lett. **103**, 051603 (2013).

[90] C. Osterkamp, J. Scharpf, S. Pezzagna, J. Meijer, T. Diemant, R. Jürgen Behm, B. Naydenov, and F. Jelezko, *Increasing the creation yield of shallow single defects in diamond by surface plasma treatment*, Appl. Phys. Lett. **103**, 193118 (2013).

[91] M. Kaviani, P. Deák, B. Aradi, T. Frauenheim, J.-P. Chou, and A. Gali, *Proper surface termination for luminescent near-surface NV centers in diamond*, Nano Lett. **14**, 4772 (2014).

[92] K. Ohno, F. Joseph Heremans, C. F. de las Casas, B. A. Myers, B. J. Aleman, A. C. Bleszynski Jayich, and D. D. Awschalom, *Three-dimensional localization of spins in diamond using ^{12}C implantation*, Appl. Phys. Lett. **105**, 052406 (2014).

[93] F. Fávaro de Oliveira, S. A. Momenzadeh, D. Antonov, J. Scharpf, C. Osterkamp, B. Naydenov, F. Jelezko, A. Denisenko, and J. Wrachtrup, *Toward optimized surface delta-profiles of nitrogen-vacancy centers activated by helium irradiation in diamond*, Nano Lett. **16**, 2228 (2016).

[94] J. D. Jackson, *Classical Electrodynamics* (J. Wiley & Sons,), 3rd edition (1999).

[95] Y. Dovzhenko, F. Casola, S. Schlotter, T. X. Zhou, F. Büttner, R. L. Walsworth, G. S. D. Beach, and A. Yacoby, *Imaging the spin texture of a skyrmion under ambient conditions using an atomic-sized sensor*, Arxiv preprint arxiv: 1611.00673 (2016).

[96] M. Pelliccione, A. Jenkins, P. Ovartchaiyapong, C. Reetz, E. Emmanouilidou, N. Ni, and A. C. Bleszynski Jayich, *Scanned probe imaging of nanoscale magnetism at cryogenic temperatures with a single-spin quantum sensor*, Nature Nanotech. **11**, 700 (2016).

[97] M. Grinolds, M. Warner, K. De Greve, Y. Dovzhenko, L. Thiel, R. Walsworth, S. Hong, P. Maletinsky, and A. Yacoby, *Sub-nanometer resolution in three dimensional magnetic resonance imaging of individual dark spins*, Nature Nanotech. **9**, 279 (2014).

[98] F. Lo Iacono, N. Bologna, M. V. Diamanti, Y.-H. Chang, S. Santos, and M. Chiesa, *General parametrization of persisting long-range nanoscale phenomena in force measurements emerging under ambient conditions*, Journ. Phys. Chem. C **119**, 13062 (2015).

[99] J. N. Israelachvili, *Intermolecular and Surface Forces* (Elsevier), 2nd edition (1991).

[100] D. S. Wastl, A. J. Weymouth, and F. J. Giessibl, *Atomically resolved graphitic surfaces in air by atomic force microscopy*, ACS Nano **8**, 5233 (2014).

[101] O. Lehtinen, B. Naydenov, P. Börner, K. Melentjevic, C. Müller, L. P. McGuinness, S. Pezzagna, J. Meijer, U. Kaiser, and F. Jelezko, *Molecular dynamics simulations of shallow nitrogen and silicon implantation into diamond*, Phys. Rev. B **93**, 035202 (2016).

[102] T. Lottermoser, T. Lonkai, U. Amann, D. Hohlwein, J. Ihringer, and M. Fiebig, *Magnetic phase control by an electric field*, Nature **430**, 541 (2004).

[103] X. He, Y. Wang, N. Wu, A. N. Caruso, E. Vescovo, K. D. Belashchenko, P. A. Dowben, and C. Binek, *Robust isothermal electric control of exchange bias at room temperature*, Nature Mat. **9**, 579 (2010).

[104] T. Kosub, M. Kopte, R. Hühne, P. Appel, B. Shields, P. Maletinsky, R. Hübner, M. O. Liedke, J. Fassbender, O. G. Schmidt, and D. Makarov,

Purely antiferromagnetic magnetoelectric random access memory, Nature Comm. **8**, 13985 (2017).

[105] W. Zhang, W. Han, S.-H. Yang, Y. Sun, Y. Zhang, B. Yan, and S. S. P. Parkin, *Giant facet-dependent spin-orbit torque and spin hall conductivity in the triangular antiferromagnet IrMn$_3$*, Sci. Adv. **2**, 1600759 (2016).

[106] E. V. Gomonay and V. M. Loktev, *Spintronics of antiferromagnetic systems*, Low Temp. Phys. **40**, 17 (2014).

[107] T. Jungwirth, X. Marti, P. Wadley, and J. Wunderlich, *Antiferromagnetic spintronics*, Nature Nanotech. **11**, 231 (2016).

[108] P. Wadley, B. Howells, J. Železnỳ, C. Andrews, V. Hills, R. P. Campion, V. Novak, K. Olejník, F. Maccherozzi, S. Dhesi, S. Martin, T. Wagner, J. Wunderlich, F. Freimuth, Y. Mokrousov, J. Kunes, J. Chauhan, M. Grzybowski, A. Rushforth, K. W. Edmonds, B. Gallagher, and T. Jungwirth, *Electrical switching of an antiferromagnet*, Science **351**, 587 (2016).

[109] I. Fina and X. Marti, *Electric control of antiferromagnets*, IEEE Trans Mag. **53**, 2500107 (2016).

[110] R. Wiesendanger, *Spin mapping at the nanoscale and atomic scale*, Rev. Mod. Phys. **81**, 1495 (2009).

[111] F. Nolting, A. Scholl, J. Stöhr, J. W. Seo, J. Fompeyrine, H. Siegwart, J. . Locquet, S. Anders, J. Lüning, E. E. Fullerton, M. F. Toney, M. R. Scheinfein, and H. A. Padmore, *Direct observation of the alignment of ferromagnetic spins by antiferromagnetic spins*, Nature **405**, 767 (2000).

[112] A. Scholl, J. Stöhr, J. Lüning, J. Seo, J. Fompeyrine, H. Siegwart, J.-P. Locquet, F. Nolting, S. Anders, E. Fullerton, M. R. Scheinfein, and H. Padmor, *Observation of antiferromagnetic domains in epitaxial thin films*, Science **287**, 1014 (2000).

[113] N. Wu, X. He, A. L. Wysocki, U. Lanke, T. Komesu, K. D. Belashchenko, C. Binek, and P. A. Dowben, *Imaging and control of surface magnetization domains in a magnetoelectric antiferromagnet*, Phys. Rev. Lett. **106**, 087202 (2011).

[114] K. D. Belashchenko, *Equilibrium magnetization at the boundary of a magnetoelectric antiferromagnet*, Phys. Rev. Lett. **105**, 147204 (2010).

[115] S. Cao, N. Wu, W. Echtenkamp, V. Lauter, H. Ambaye, T. Komesu, C. Binek, and P. A. Dowben, *The surface stability of Cr$_2$O$_3$ (0001)*, J. Phys.: Condens. Matter **27**, 255003 (2015).

[116] E. Meyer, H. J. Hug, and R. Bennewitz, *Scanning Probe Microscopy*, (Springer-Verlag Berlin Heidelberg) (2004).

[117] B. J. Roth, N. G. Sepulveda, and J. P. Wikswo, *Using a magnetometer to image a two dimensional current distribution*, Journ. Appl. Phys. **65**, 361 (1989).

[118] M. Al-Mahdawi, Y. Shiokawa, S. P. Pati, S. Ye, T. Nozaki, and M. Sahashi, *Apparent critical behavior of sputter-deposited magnetoelectric antiferromagnetic Cr_2O_3 films near neel temperature*, J. Phys. D: Appl. Phys **50**, 155004 (2016).

[119] U. Köbler and A. Hoser, *Renormalization Group Theory*, (Springer-Verlag Berlin Heidelberg) (2010).

[120] L. Fallarino, A. Berger, and C. Binek, *Magnetic field induced switching of the antiferromagnetic order parameter in thin films of magnetoelectric chromia*, Phys. Rev. B **91**, 054414 (2015).

[121] P. Wadley, V. Hills, M. R. Shahedkhah, K. W. Edmonds, R. P. Campion, V. Novák, B. Ouladdiaf, D. Khalyavin, S. Langridge, V. Saidl, P. Nemec, A. Rushforth, B. Gallagher, S. Dhesi, F. Maccherozzi, J. Železnỳ, and T. Jungwirth, *Antiferromagnetic structure in tetragonal CuMnAs thin films*, Sci. Rep. **5**, 17079 (2015).

[122] K. O'Grady, L. Fernandez-Outon, and G. Vallejo-Fernandez, *A new paradigm for exchange bias in polycrystalline thin films*, Journ. Magn. and Magn.Mater. **322**, 883 (2010).

[123] M. Charilaou and F. Hellman, *Roughness effects in uncompensated antiferromagnets*, Journ. Appl. Phys. **117**, 083907 (2015).

[124] F. Hellman, A. Hoffmann, Y. Tserkovnyak, G. Beach, E. Fullerton, C. Leighton, A. MacDonald, D. Ralph, D. Arena, H. Durr, P. Fischer, J. Grollier, J. Heremans, T. Jungwirth, A. Kimmel, B. Koopmans, I. Krivorotov, S. May, A. Petford-Long, J. Rondinelli, N. Samarth, I. Schuller, A. Slavin, M. Stiles, O. Tchernyshyov, A. Thiaville, and B. Zink, *Interface-induced phenomena in magnetism*, ArXiv prepints: arXiv:1607.00439 (2016).

[125] A. Barbier, C. Mocuta, W. Neubeck, M. Mulazzi, F. Yakhou, K. Chesnel, A. Sollier, C. Vettier, and F. de Bergevin, *Surface and bulk spin ordering of antiferromagnetic materials: NiO(111)*, Phys. Rev. Lett. **93**, 257208 (2004).

[126] B. Hermsmeier, J. Osterwalder, D. J. Friedman, B. Sinkovic, T. Tran, and C. S. Fadley, *Spin-polarized photoelectron diffraction and valence-band photoemission from MnO(001)*, Phys. Rev. B **42**, 11895 (1990).

[127] E. Schierle, E. Weschke, A. Gottberg, W. Söllinger, W. Heiss, G. Springholz, and G. Kaindl, *Antiferromagnetic order with atomic layer resolution in EuTe(111) films*, Phys. Rev. Lett. **101**, 267202 (2008).

[128] L. M. Corliss, J. M. Hastings, R. Nathans, and G. Shirane, *Magnetic structure of Cr$_2$O$_3$*, Journ. Appl. Phys. **36**, 1099 (1965).

[129] C. Rehbein, N. M. Harrison, and A. Wander, *Structure of the α-Cr$_2$O$_3$ (0001) surface: An and ab initio total-energy study*, Phys. Rev. B **54**, 14066 (1996).

[130] O. Bikondoa, W. Moritz, X. Torrelles, H. J. Kim, G. Thornton, and R. Lindsay, *Impact of ambient oxygen on the surface structure of Cr$_2$O$_3$*, Phys. Rev. B **81**, 205439 (2010).

[131] P. Borisov, T. Ashida, T. Nozaki, M. Sahashi, and D. Lederman, *Magneto-electric properties of* 500 *nm Cr$_2$O$_3$ films*, Phys. Rev. B **93**, 174415 (2016).

[132] T. Gloege, H. Meyerheim, W. Moritz, and D. Wolf, *X-ray structure analysis of the Cr$_2$O$_3$ (0001)-(1x1) surface: evidence for Cr interstitial*, Surf. Sci. **441**, L917 (1999).

[133] M. Marynowski, W. Franzen, and M. El-Batanouny, *Observation of an extraordinary antiferromagnetic transition on the NiO (100) surface by metastable helium atom diffraction*, Phys. Rev. B **60**, 6053 (1999).

[134] I. Gross, W. Akhtar, V. Garcia, L. Martinez, S. Chouaieb, K. Garcia, C. Carrétéro, A. Barthélémy, P. Appel, P. Maletinsky, J.-V. Kim, J. Y. Chauleau, N. Jaouen, M. Viret, M. Bibes, S. Fusil, and V. Jacques, *Real-space imaging of non-collinear antiferromagnetic order with a single spin magnetometer*, submitted (2017).

[135] Y. Kaluzny, P. Goy, J. Raimond, and S. Haroche, *Observation of self-induced rabi oscillations in two-level atoms excited inside a resonant cavity: Ringing regime of superradiance*, Phys. Rev. Lett. **51**, 1175 (1983).

[136] J. Raimond, M. Brune, and S. Haroche, *Manipulating quantum entanglement with atoms and photons in a cavity*, Rev. Mod. Phys. **73**, 565 (2001).

[137] A. Walraff, D. Schuster, A. Blais, L. Frunzie, R.-S. Huang, J. Majer, S. Kumar, S. Girvin, and R. Schoelkopf, *Strong coupling of a single photon to a superconducting qubit using circuit quantum electrodynamics*, Nature **431**, 162 (2004).

[138] J. You and F. Nori, *Atomic physics and quantum optics using superconducting circuits*, Nature **474**, 589 (2011).

[139] S. Thiele, F. Balestro, R. Ballou, S. Klyatskaya, M. Ruben, and W. Wernsdorfer, *Electrically driven nuclear spin resonance in single-molecule magnets*, Science **344**, 1135 (2014).

[140] F. Koppens, C. Buizert, K. Tielrooij, I. Vink, K. Nowack, T. Meunier, L. Kouwenhoven, and L. Vandersypen, *Driven coherent oscillations of a single electron spin in a quantum dot*, Nature **442**, 766 (2006).

[141] M. Sparks, *Ferromagnetic-Relaxation Theory* (McGraw-Hill) (1964).

[142] U. Schollwöck, J. Richter, D. Farnell, and R. Bishop, *Quantum Magnetism* (Springer Berlin Heidelberg) (2004).

[143] L. Balents, *Spin liquids in frustrated magnets*, Nature **464**, 199 (2010).

[144] F. Garcia-Sanchez, P. Borys, R. Soucaille, J.-P. Adam, R. L. Stamps, and J.-V. Kim, *Narrow magnonic waveguides based on domain walls*, Phys. Rev. Lett. **114**, 247206 (2015).

[145] S. Parkin, M. Hayashi, and L. Thomas, *Magnteic domain wall racetrack memory*, Science **320**, 190 (2008).

[146] V. Agrawal, P. Neuzil, and D. W. van der Weide, *A microfabricated tip for simultaneous acquisition of sample topography and high-frequency magnetic field*, Appl. Phys. Lett. **71**, 2343 (1997).

[147] S.-C. Lee, C. P. Vlahacos, B. J. Feenstra, A. Schwartz, D. E. Steinhauer, F. C. Wellstood, and S. M. Anlage, *Magnetic permeability imaging of metals with a scanning near-field microwave microscope*, Appl. Phys. Lett. **77**, 4404 (2000).

[148] B. Rosner and D. W. van der Weide, *High frequency near-field microscopy*, Rev. Sci. Instrum. **73**, 2505 (2003).

[149] T. Sebastian, K. Schultheiss, B. Obry, B. Hillebrands, and H. Schultheiss, *Microfocuassed brillouin light scattering: imaging spin waves at the nanoscale*, Front. Phys. **3**, 35 (2015).

[150] R. C. Black, F. C. Wellstood, E. Dantsker, A. H. Miklich, D. Koelle, F. Ludwig, and J. Clarke, *Imaging radio-frequency fields using a scanning squid microscope*, Appl. Phys. Lett. **66**, 1267 (1995).

[151] P. Boehi and P. Treutlein, *Simple microwave field imaging technique using hot atomic vapor cells*, Appl. Phys. Lett. **101**, 181107 (2012).

[152] A. Horsley, G. Du, M. Pellaton, C. Affolderbach, G. Mileti, and P. Treutlein, *Imaging of relaxation times and microwave field strength in a microfabricated vapor cell*, Phys. Rev. A **88**, 063407 (2013).

[153] C. Affolderbach, G.-X. Du, T. Bandi, A. Horsley, P. Treutlein, and G. Mileti, *Imaging microwave and dc magnetic fields in a vapor-cell Rb atomic clock*, IEEE Trans. Instr. Meas. **64**, 3629 (2015).

[154] P. Boehi, M. Riedel, T. Haensch, and P. Treutlein, *Imaging of microwave fields using ultracold atoms*, Appl. Phys. Lett. **97**, 051101 (2010).

[155] P. Wang, Z. Yuan, P. Huang, X. Rong, M. Wang, X. Xu, C. Duan, C. Ju, F. Shi, and J. Du, *High-resolution vector microwave magnetometry based on solid state spins in diamond*, Nature Comm. **6**, 6631 (2015).

[156] H. Haus and J. Melcher, *Electromagnetic fields and energy*, Massachusetts Insitute of Technology: MIT OpenCourse Ware) (accessed 07.03.2017).

[157] S. Sayil, D. Kerns, and K. S., *Comparison of contactless measurement and mesting techniques to a new all-silicon optical test and characterization method*, IEEE Trans. Instr. Meas. **54**, 2082 (2005).

[158] A. Horsley, G. Du, and P. Treutlein, *Widefield microwave imaging in alkali vapor cells with sub-100 μm resolution*, New J. Phys. **17**, 112002 (2015).

[159] A. V. Chumak, V. Vasyuchka, A. Serga, and B. Hillebrands, *Magnon spintronics*, Nature Phys. **11**, 453 (2015).

[160] D. Grundler, *Reconfigurable magnonics heats up*, Nature Phys. **11**, 438 (2015).

[161] T. van der Sar, F. Casola, R. Walsworth, and A. Yacoby, *Nanometre-scale probing of spin waves using single-electron spins*, Nature Comm. **6**, 7886 (2015).

[162] C. Du, T. V. der Sar, T. X. Zhou, P. Upadhyaya, Francesco, Casola, H. Zhang, M. C. Onbasli, C. A. Ross, R. L. Walsworth, Y. Tserkovnyak, and A. Yacoby, *Control and local measurement of the spin chemical potential in a magnetic insulator*, Arxiv preprint arxiv: arXiv:1611.07408 (2016).

[163] T. L. Monchesky, *Detection with unpolarized currents*, Nature Nanotech. **10**, 1008 (2015).

[164] *Neutrons tap into magnetism in topological insulators at high temperatures*, Technical report, Oak Ridge National Laboratory, ScienceDaily, 9 May 2016, www.sciencedaily.com/releases/2016/05/160509132835.htm (2016).

[165] F. Katmis, V. Lauter, F. S. Nogueira, B. A. Assaf, M. E. Jamer, P. Wei, B. Satpati, J. W. Freeland, I. Eremin, D. Heiman, and et al., *A high-temperature ferromagnetic topological insulating phase by proximity coupling*, Nature **533**, 513 (2016).

[166] M. König, S. Wiedmann, C. Brüne, A. Roth, H. Buhmann, L. Molenkamp, X.-L. Qi, and S.-C. Zhang, *Quantum spin hall insulator state in HgTe quantum wells*, Science **318**, 766 (2007).

[167] A. Fert, V. Cros, and J. Sampaio, *Skyrmions on the track*, Nature Nanotech. **8**, 152 (2013).

[168] R. Tomasello, E. Martinez, R. Zivieri, L. Torres, M. Carpentieri, and G. Finocchio, *A strategy for the design of skyrmion racetrack memories*, Sci. Rep. **4**, 6784 (2014).

[169] X. Zhang, M. Ezawa, and Y. Zhou, *Magnetic skyrmion logic gates: conversion, duplication and merging of skyrmions*, Sci. Rep. **5**, 9400 (2015).

[170] X. Zhang, Y. Zhou, M. Ezawa, G. P. Zhao, and W. Zhao, *Magnetic skyrmion transistor: skyrmion motion in a voltage-gated nanotrack*, Sci. Rep. **5**, 11369 (2015).

[171] J.-P. Tetienne, T. Hingant, J.-V. Kim, L. H. Diez, J.-P. Adam, K. Garcia, J.-F. Roch, S. Rohart, A. Thiaville, D. Ravelosona, and V. Jacques, *Nanoscale imaging and control of domain-wall hopping with a nitrogen-vacancy center microscope*, Science **344**, 1366 (2014).

[172] A. Gozar, G. Logvenov, L. F. Kourkoutis, A. T. Bollinger, L. A. Giannuzzi, D. A. Muller, and I. Bozovic, *High-temperature interface superconductivity between metallic and insulating copper oxides*, Nature **455**, 782 (2008).

[173] J. A. Bert, B. Kalisky, C. Bell, M. Kim, Y. Hikita, H. Y. Hwang, and K. A. Moler, *Direct imaging of the coexistence of ferromagnetism and superconductivity at the $LaAlO_3$ - $SrTiO_3$ interface*, Nature Phys. **7**, 767 (2011).

[174] P. Rickhaus, P. Makk, M.-H. Liu, E. Tovari, M. Weiss, R. Maurand, K. Richter, and C. Schönenberger, *Snake trajectories in ultraclean graphene p–n junctions*, Nature Comm. **6**, 6470 (2015).

[175] M. Z. Hasan and C. L. Kane, *Colloquium: Topological insulators*, Rev. Mod. Phys. **82**, 3045 (2010).

[176] S. Bauer and C. A. Bobisch, *Nanoscale electron transport at the surface of a topological insulator*, Nature Comm. **7**, 11381 (2016).

[177] T. Taychatanapat, K. Watanabe, T. Taniguchi, and P. Jarillo-Herrero, *Electrically tunable transverse magnetic focusing in graphene*, Nature Phys. **9**, 225 (2013).

[178] J. R. Williams, T. Low, M. S. Lundstrom, and C. M. Marcus, *Gate-controlled guiding of electrons in graphene*, Nature Nanotech. **6**, 222 (2011).

[179] C. L. Degen, F. Reinhard, and P. Cappellaro, *Quantum sensing*, Arxiv preprint arxiv: 1611.02427v1 (2016).

[180] J. Medford, . Cywiński, C. Barthel, C. M. Marcus, M. P. Hanson, and A. C. Gossard, *Scaling of dynamical decoupling for spin qubits*, Phys. Rev. Lett. **108** (2012).

[181] S. Rohr, *Hybrid spin-nanomechanical systems in parametric interaction.*, Ph.D. thesis, Grenoble University (2015).

Appendix A

Weighting Function

The weighting function describes the strength of a signal at a given frequency and thereby characterizes the sensitive frequency range of the different coherent detection schemes presented in Chap. 1 [45, 179]. In this Appendix, we deduce the weighting functions for the sensing schemes, which are plotted in Fig. 1.9.

A.1 Ramsey interferometry

The signal of a Ramsey measurement is given by the phase collected during the free evolution time τ, which can be described by (see Chap. 1 and Appendix B)

$$\phi = 2\pi\gamma_{\mathrm{NV}} \int_0^\tau B(t)dt. \tag{A.1}$$

As Ramsey measurements are applied to study DC magnetic fields, the magnetic field when starting the sequence is typically $B(t = 0) \neq 0$. Furthermore, we can assume $B(t)$ to be an even function as we are only interested in $B(t)$ for $t > 0$. We can therefore represent $B(t)$ by the following Fourier series

$$B(t) = \int_{-\infty}^\infty B(\omega) \cos(\omega t)d\omega. \tag{A.2}$$

The phase can thus be written as

$$\phi = 2\pi\gamma_{\mathrm{NV}} \int_{-\infty}^\infty \int_0^\tau B(\omega) \cos(\omega t)dt d\omega. \tag{A.3}$$

We finally first integrate over the time which results in

$$\phi = \int_{-\infty}^\infty B(\omega) \left(\frac{2\pi\gamma_{\mathrm{NV}}}{\omega} \sin(\omega\tau) \right) d\omega = \int_{-\infty}^\infty B(\omega)W_{\mathrm{Ramsey}}(\tau)d\omega, \tag{A.4}$$

where we introduced the weighting function $W_{\mathrm{Ramsey}}(\tau)$. This function describes the sensitive frequency range of a Ramsey measurement with a particular evolution

time τ. Because the signal of Ramsey interferometry is proportional to the phase (assuming small magnetic fields, see Appendix B), the value of the weighting function describes the weighted signal at a specific frequency. If normalized, as depicted in Fig. 1.9, the function describes the percentage of the signal at a certain frequency in comparison to the maximal obtained signal for a particular measurement technique and can thereby also be related to the sensitivity at a certain frequency. Note that the weighting function describes the response to a magnetic field, which has a certain synchronization to the Ramsey measurement. We here chose a synchronization that results in a description of the magnetic field by pure cosinus functions. For a different synchronization the weighting function can analogously be deduced.

A.2   Spin Echo spectroscopy

The signal of a Spin Echo measurement is given by the phase

$$\phi = 2\pi\gamma_{\text{NV}} \left(\int_0^{\tau/2} B(t)dt + \int_{\tau/2}^{\tau} B(t)dt \right). \tag{A.5}$$

Similar to Ramsey measurements, we can describe the signal by a Fourier series, which in a more general form can be described by

$$B(t) = \int_{-\infty}^{\infty} B(\omega)\cos(\omega t + \phi)d\omega. \tag{A.6}$$

The representation (we can choose a certain phase as we are only interested in $B(t)$ for $t > 0$ and $t < \tau$) corresponds to synchronization of the AC magnetic field to the measurement sequence. For Spin Echo measurements, the signal is often considered to be synchronized with a phase of $\phi = -\pi/2$ [45], which we also consider here and which results in

$$\phi = 2\pi\gamma_{\text{NV}} \left(\int_0^{\tau/2} \int_{-\infty}^{\infty} B(\omega)\sin(\omega t)d\omega dt - \int_{\tau/2}^{\tau} \int_{-\infty}^{\infty} B(\omega)\sin(\omega t)d\omega dt \right). \tag{A.7}$$

By solving the time integral we finally obtain

$$\phi = \int_{-\infty}^{\infty} B(\omega) \left(-2\pi\gamma_{\text{NV}} \frac{4}{\omega} \sin^2(\frac{\omega\tau}{4}) \cos(\frac{\omega\tau}{2}) \right) d\omega = \int_{-\infty}^{\infty} B(\omega)W_{\text{Spin Echo}}(\tau)d\omega, \tag{A.8}$$

where we define the weighting function $W_{\text{Spin Echo}}$ for Spin Echo spectroscopy. Note that a different synchronization results in modifications of the resulting weighting functions.

A.3   Rabi oscillations

To deduce Rabi oscillations in Chap. 1 we used a spectral ansatz similar to the Fourier series presented in the previous sections. Because the weighting function defines the weighted signal obtained for a certain frequency, we have to consider the impact of a detuning of our driving MW fields with the NV transition. Using the Hamiltonian in Eq. 1.15, which is not in resonance ($\omega_1 \neq \omega$) with the transition, we can deduce the two coupled differential equations

$$\frac{\delta c_0}{\delta t} = -i\,\frac{\Omega}{2}e^{i\omega_1 t}c_1 \tag{A.9}$$

$$\frac{\delta c_1}{\delta t} = -i\omega c_1 - i\,\frac{\Omega}{2}e^{-i\omega_1 t}c_0. \tag{A.10}$$

Using the ansatz

$$C_1 = c_1 e^{i\omega_1 t} \tag{A.11}$$

we can rewrite the equations into the two coupled differential equations

$$\frac{\delta c_0}{\delta t} = -i\,\frac{\Omega}{2}C_1 \tag{A.12}$$

$$\frac{\delta C_1}{\delta t} = i\Delta C_1 - i\,\frac{\Omega}{2}c_0, \tag{A.13}$$

where $\Delta = (\omega_1 - \omega)$ corresponds to the detuning of the MW field. The general solution for these coupled differential equations is given by:

$$c_0 = e^{i\Delta t/2}\left[a_0(0)\cos(\frac{\widetilde{\Omega}}{2}t) - \frac{i}{\widetilde{\Omega}}\left[\Delta a_0(0) + \Omega a_1(0)\right]\sin(\frac{\widetilde{\Omega}}{2}t)\right] \tag{A.14}$$

$$C_1 = e^{i\Delta t/2}\left[a_1(0)\cos(\frac{\widetilde{\Omega}}{2}t) + \frac{i}{\widetilde{\Omega}}\left[\Delta a_1(0) + \Omega a_0(0)\right]\sin(\frac{\widetilde{\Omega}}{2}t)\right], \tag{A.15}$$

where we defined the generalized Rabi frequency $\widetilde{\Omega} = \sqrt{\Omega^2 + \Delta^2}$. The constants $a_0(0)$ and $a_1(0)$ have to be defined from the boundary conditions. Assuming the system to be initialized in its ground state ($a_1(0) = 0$, $a_0(0) = 1$) results in an excited state probability given by

$$P_1(t) = |C_1|^2 = |\frac{\Omega^2}{\widetilde{\Omega}^2}\sin(\frac{\widetilde{\Omega}}{2}t)|^2 = \frac{1}{2}\frac{\Omega^2}{\widetilde{\Omega}^2}\left(1 - \cos(\widetilde{\Omega}t)\right). \tag{A.16}$$

The measured fluorescence signal I during Rabi oscillations is proportional to this excited state population. The maximal magnetic field signal can be defined as $S = \partial I/\partial B|_{\text{max}}B$ (see Appendix B). Hence, the signal is proportional to

$$S \sim \partial P_1(t)/\partial B|_{\max} B \approx \left(\frac{1}{2} \frac{\Omega^2}{\widetilde{\Omega}^2} \sin(\widetilde{\Omega}t) \frac{\partial \widetilde{\Omega}}{\partial B} t \right) B = W_{\mathrm{Rabi}}(t)B, \qquad (A.17)$$

where we define the weighting function $W_{\mathrm{Rabi}}(t)$ which is given by

$$W_{\mathrm{Rabi}}(t) = \quad \frac{1}{2} \frac{(2\pi\gamma_{\mathrm{NV}}B)^2}{(2\pi\gamma_{\mathrm{NV}}B)^2 + (\omega_1 - \omega)^2} \qquad (A.18)$$
$$\left(\sin(\sqrt{(2\pi\gamma_{\mathrm{NV}}B)^2 + (\omega_1 - \omega)^2}t) \frac{(2\pi\gamma_{\mathrm{NV}})^2 Bt}{\sqrt{(2\pi\gamma_{\mathrm{NV}}B)^2 + (\omega_1 - \omega)^2}} \right).$$

Equation A.18 shows that the filter function for Rabi measurements depends on the driving MW field B. The first term describes the amplitude of the Rabi oscillations for a given detuning while the second part describes the slope of the Rabi oscillations for a given measurement time t. We here define a simplified weighting function $\widetilde{W}_{\mathrm{Rabi}}(B)$ describing the maximal signal that can be measured at a certain frequency, which is given by the amplitude of the Rabi oscillations:

$$\widetilde{W}_{\mathrm{Rabi}}(B) = \frac{1}{2} \frac{(2\pi\gamma_{\mathrm{NV}}B)^2}{(2\pi\gamma_{\mathrm{NV}}B)^2 + (\omega_1 - \omega)^2}, \qquad (A.19)$$

which is a Lorentzian with a width given by the magnetic field strength B. A strong MW magnetic field lead to broadening of the simplified weighting function $\widetilde{W}_{\mathrm{Rabi}}(B)$. In the limit of small magnetic fields the Lorentzian function becomes a delta-like line shape. In this case the inhomogeneously broadened line shape of the NV center, which can be described by a Gaussian, whose width is limited by T_2^* [44], can be resolved. In Figure 1.9 we therefore illustrate the weighting function with Gaussian profile with $T_2^* = 1\,\mu$s.

Appendix B

Sensitivity

The sensitivity defines the magnetic field that can be detected in a given measurement time T

$$\eta = \delta B \sqrt{T}, \tag{B.1}$$

where δB is the smallest magnetic field obtained for a SNR of 1. Assuming a magnetic field-dependent signal $S(B)$ with a noise N the minimal sensitivity can be written as

$$\eta = \frac{N}{\partial S/\partial B|_{\mathrm{max}}} \sqrt{T}. \tag{B.2}$$

For a spin-based magnetometer the noise is fundamentally limited by quantum noise associated with projecting the spin onto the fluorescence states. For the NV center photon shot-noise dominates the noise and can be used to derive the sensitivity [45]. The signal on the other hand depends on the measurement applied. In this section, the signal of the different sensing schemes will be discussed and the explicit formula for their sensitivities will be deduced.

B.1 Electron spin resonance

In electron spin resonance (ESR) measurements the signal (in counts per second, cps) can be described by the formula [44]

$$I(f) = I_0 \left[1 - C_{\mathrm{ESR}} F \left(\frac{f - f_{\mathrm{NV}}}{\Delta f} \right) \right], \tag{B.3}$$

where I_0 is the average count rate of the NV, C_{ESR} is the ESR contrast and F is the line shape profile. Under low driving conditions (weak optical pumping and weak MW fields) the ESR of the NV center is described by a Gaussian. Under strong driving conditions, a Lorentzian profile needs to be considered [44]. All profiles depend on the MW driving frequency f, the NV-transition frequency f_{NV} and the linewidth Δf (defined as the Full Width at Half Maximum (FWHM)). In Fig. B.1
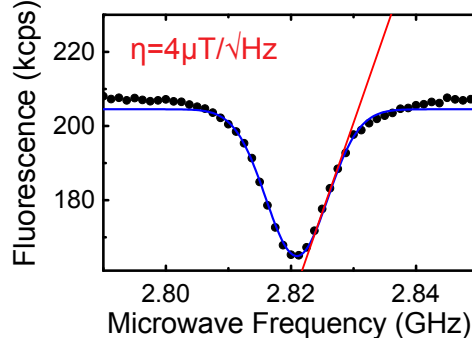
Figure B.1: ESR measurements. Data are plotted in black and a Gaussian fit (see main text) is depicted in blue. The red line indicates the maximum signal response at the optimal working point, which is used to deduce the sensitivity of $\eta = 4\,\mu\mathrm{T}/\sqrt{\mathrm{Hz}}$ (data taken from [16]).

we used a Gaussian fit to describe the ESR

$$I = I_0 \left[1 - C_{\mathrm{ESR}} e^{\left(-\frac{(f-f_{\mathrm{NV}})^2}{2\sigma^2} \right)} \right]. \tag{B.4}$$

The fit yields $I_0 = 205\,\mathrm{kcps}$, $C_{\mathrm{ESR}} = 0.19$, $f_{\mathrm{NV}} = 2.821\,\mathrm{GHz}$ and $\sigma = 4.96\,\mathrm{MHz}$. Note that the depicted ESR spectrum was measured under moderate driving conditions, which can be approximated by the Gaussian profile for small detuning.

The maximum, magnetic field-dependent signal is illustrated by the red line in Fig. B.1 and can be deduced from the maximum slope of the ESR spectrum as follows

$$S = \left. \frac{\partial I}{\partial B} \right|_{\mathrm{max}} B = \gamma_{\mathrm{NV}} \left. \frac{\partial I}{\partial f} \right|_{\mathrm{max}} B = \gamma_{\mathrm{NV}} I_0 C_{\mathrm{ESR}} \frac{B}{\sqrt{e}\sigma}. \tag{B.5}$$

Here, the frequency is given by $f = \gamma_{\mathrm{NV}} B$, with $\gamma_{\mathrm{NV}} = 28\,\mathrm{kHz}\,\mu\mathrm{T}^{-1}$ being the NV centers gyro magnetic ratio. Assuming a shot noise of $N = \sqrt{I_0}$, we can deduce the sensitivity using equation B.2

$$\eta_{\mathrm{DC,ESR}} = \frac{\sqrt{e}}{\gamma_{\mathrm{NV}}} \frac{\sigma}{C_{\mathrm{ESR}}\sqrt{I_0}}. \tag{B.6}$$

Analogously to the Gaussian profile a sensitivity for a Lorentzian profile can be calculated. We define the general sensitivity as

$$\eta_{\mathrm{DC,ESR}} = \frac{1}{\gamma_{\mathrm{NV}}} \frac{\sqrt{I}}{\delta I/\delta f_{\mathrm{MW}}} = P_F \frac{1}{\gamma_{\mathrm{NV}}} \frac{\Delta f}{C_{\mathrm{ESR}}\sqrt{I}}, \tag{B.7}$$

where P_F is a numerical parameter for the specific profile [44]. This parameter is given by $P_G = \sqrt{e/8\ln 2} \approx 0.70$ for a Gaussian and $P_L = 4/3\sqrt{3} \approx 0.77$ for a Lorentzian profile. The FWHM Δf depends on the optical and MW excitation

power employed to measure the ESR and is fundamentally limited by the dephasing rate $\Delta f = \Gamma_2^* \sim 1/T_2^*$ [44]. The dephasing rate can alternatively be measured with Ramsey measurements. For the depicted NV center in a scanning probe we obtain a sensitivity of $\eta_{\text{ESR}} = 4\,\mu\text{T}/\sqrt{\text{Hz}}$.

B.2 Ramsey interferometry

The Ramsey signal (in counts per shot), in the typical case of an NV center consisting of a ^{14}N atom, can be described by a beating of three different frequencies

$$I = I_{\text{avg}} \left[1 + C_{\text{pulsed}} \exp\left[-\left(\frac{\tau}{T_2^*} \right)^n \right] \left(\sum_1^3 a_i \cos\left(\omega_i \tau + \phi_i \right) \right) \right]. \qquad (B.8)$$

Here, I_{avg} is the average count rate ($I_{\text{avg}} = 1/2(I_0 + I_1)$), where I_0 and I_1 are the count rates from the $m_s = 0$ and $m_s = 1$ state respectively. C_{pulsed} is the contrast for pulsed experiments and is defined as $C_{\text{pulsed}} = \frac{1}{2} \frac{I_0 - I_1}{I_{\text{avg}}}$. T_2^* is the dephasing time and n depends on the detail of the noise spectrum. In this Appendix we assume a $1/f$ noise, which results in an n=2 [180]. The three oscillations stem from the three hyperfine states induced by the ^{14}N. Each frequency is given by the detuning to one hyperfine state. The different amplitudes and phases arise from the different detunings during the preparation of the superposition state [181]. We used Eq. B.8 to fit the data yielding $I_{\text{avg}} = 0.0116$ counts per shot, $C_{\text{pulsed}} = 0.097$ and $T_2^* = 3.6\,\mu\text{s}$. The three oscillations have an amplitude of $a_1 = -0.39$, $a_2 = -0.34$, $a_3 = -0.27$, a frequency $\omega_1/2\pi = 2.315\,\text{MHz}$, $\omega_2/2\pi = 4.480\,\text{MHz}$, $\omega_3/2\pi = 6.628\,\text{MHz}$, and a phase $\phi_1 = 0.813$, $\phi_2 = 1.586$, $\phi_3 = 2.23$ respectively.
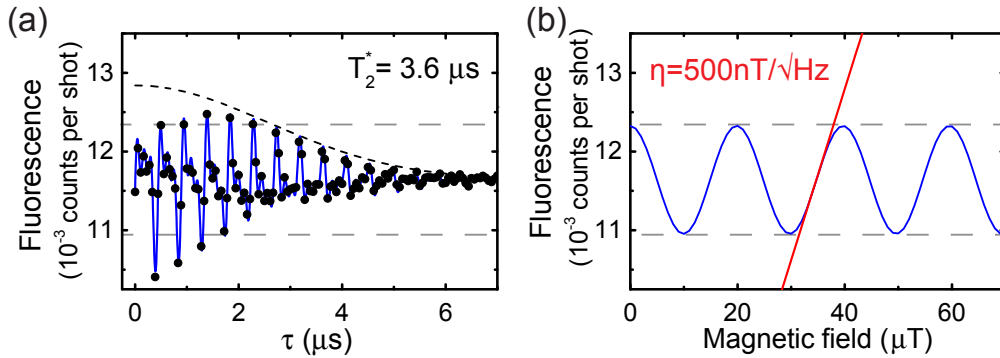
Figure B.2: (a) Ramsey interferometry. Data are plotted in black and a fit (see main text) is depicted in blue. (b) Signal under strong driving condition for a fixed evolution time indicated by the gray dashed line. The red line indicates the maximum signal response at the optimal working point, which is used to deduce a sensitivity of $\eta = 700\,\text{nT}\sqrt{\text{Hz}}$ (data taken from [50]).

The frequencies depend on the MW detuning, which can be interpreted as a magnetic field with a frequency $\omega_{\text{central}} = 2\pi\gamma_{\text{NV}}B_\Delta$ for the central frequency and $\omega_\pm = \omega_{\text{central}} \pm 2\pi\Delta_N$ for the other frequencies. Here, Δ_N is the hyperfine coupling strength of $2.2\,\text{MHz}$ [35].

To determine the sensitivity, we consider a Ramsey signal obtained under strong driving conditions (strong MW pulses, where $\pi/2$-MW pulse length $<< 1/4\Delta_N$). Under these conditions all oscillations have no phase and the same amplitude of $a_i = 1/3$ [181], which allows us to simplify equation B.8 to

$$I(B_\Delta, \tau) = I_{\text{avg}}\left[1 - C_{\text{pulsed}}\exp\left[-\left(\frac{\tau}{T_2^*}\right)^n\right]\left(\frac{2\cos(2\pi\Delta_N\tau) + 1}{3}\cos(2\pi\gamma_{\text{NV}}B_\Delta\tau)\right)\right].$$
(B.9)

Setting the evolution time to a τ, where the envelope phase is $\Phi_2 = 2\pi\Delta_N\tau \approx N2\pi$ with $N \in \mathbb{Z}$, results in a field-dependent signal as depicted in Fig B.2 (b) and can be described by

$$I = I_{\text{avg}}\left[1 - C_{\text{pulsed}}\cos(2\pi\gamma_{\text{NV}}B_\Delta\tau)\exp\left[-\left(\frac{\tau}{T_2^*}\right)^n\right]\right].$$
(B.10)

The signal can be approximated by

$$S = \frac{\partial I_0}{\partial B}\bigg|_{\text{max}} B = I_{\text{avg}}C_{\text{pulsed}}\ (2\pi\gamma_{\text{NV}}B_\Delta\tau)\exp\left[-\left(\frac{\tau}{T_2^*}\right)^n\right],$$
(B.11)

which is illustrated by the red line in Fig. B.2 (b) and corresponds to phase of $\Phi_1 = 2\pi\gamma_{\text{NV}}B_\Delta\tau \approx (1/2 + N)\pi$ for $N \in \mathbb{Z}$. From this signal combined with the shot noise $N = \sqrt{I_{\text{avg}}}$ we can deduces the smallest magnetic field $\delta B_\Delta|_{\text{shot}}$ that can be resolved with an SNR of 1 as

$$\delta B_\Delta|_{\text{shot}} = \frac{1}{2\pi\gamma_{\text{NV}}\sqrt{I_{\text{avg}}}C_{\text{pulsed}}}\left[\frac{1}{\tau}\exp\left(\frac{\tau}{T_2^*}\right)^n\right].$$
(B.12)

The measurement time for a single shot experiments can be approximated by the evolution time τ. During a total measurement time of T, T/τ repetitions of a single shot measurement can be performed. In this case, the fluorescence in I_{avg} (in counts per shot) scales as $I_{\text{avg}}T/\tau$ and we finally obtain the shot noise-limited sensitivity

$$\eta_{\text{Ramsey}} = \delta B_\Delta\sqrt{T} = \frac{1}{2\pi\gamma_{\text{NV}}\sqrt{I_{\text{avg}}}C_{\text{pulsed}}}\left[\frac{1}{\sqrt{\tau}}\exp\left(\frac{\tau}{T_2^*}\right)^n\right].$$
(B.13)

The optimal τ can be deduced from the last term in Eq. B.13. For $n = 2$, as assumed in this Appendix, the optimal working point is $\tau = T_2^*/2$. Under these conditions, the maximum achievable sensitivity is given by

$$\eta_{\text{Ramsey}} = \frac{\sqrt{2}e^{\frac{1}{4}}}{2\pi\gamma_{\text{NV}}C_{\text{pulsed}}\sqrt{I_{\text{avg}}}\sqrt{T_2^*}}.$$
(B.14)

For the depicted measurement, we obtain a sensitivity of $\eta_{\text{Ramsey}} = 500 \text{ nT}/\sqrt{\text{Hz}}$, which forms the maximum achievable DC sensitivity for the measured single NV center. Note, that the depicted Ramsey signal was measured for an NV center implanted 17 nm below the surface, which was not placed in a scanning probe. This explains the smaller count rates and a possible longer dephasing time.

B.3 Spin Echo spectroscopy

The spin echo signal is described by the following formula [51]

$$I = I_{\text{avg}}\left[1 - C_{\text{pulsed}}\exp\left[-\left(\frac{\tau}{T_2}\right)^n\right]\sum_j \exp\left[-\left(\frac{\tau - j\tau_{\text{rev}}}{T_{\text{dec}}}\right)^2\right]\cos\left(2\pi\gamma_{\text{NV}}B_{\text{AC}}\tau\right)\right].$$

(B.15)

I_{avg} is the average count rate, C_{pulsed} is the contrast for pulsed experiments and T_2 is the decoherence time. The exponent n depends on details of the decoherence process and is here set to $n = 2$ (see Sec. B.2). τ_{rev} indicates the revival period associated with the Larmor precession of the ^{13}C nuclear spins and T_{dec} is the correlation time of the ^{13}C nuclear spin bath [51]. For the depicted spin echo measurement, we derive $I_{\text{avg}} = 0.0365$ counts per shot, $C_{\text{pulsed}} = 0.199$, $T_2 = 94\,\mu\text{s}$, $\tau_{\text{rev}} = 19.8\,\mu\text{s}$ and $T_{\text{dec}} = 6.0\,\mu\text{s}$. Note that $1/\tau_{\text{rev}} = g_{\text{n}}\mu_{\text{n}}B_{\text{DC}}$, where B_{DC} is the DC magnetic field strength and $g_{\text{n}}\mu_{\text{n}} = 1.071\text{kHz/G}$ is the gyro magnetic ratio of the ^{13}C spins. Also note that typically no AC magnetic field is applied ($B_{\text{AC}} = 0$) and the last term can be neglected for fitting.
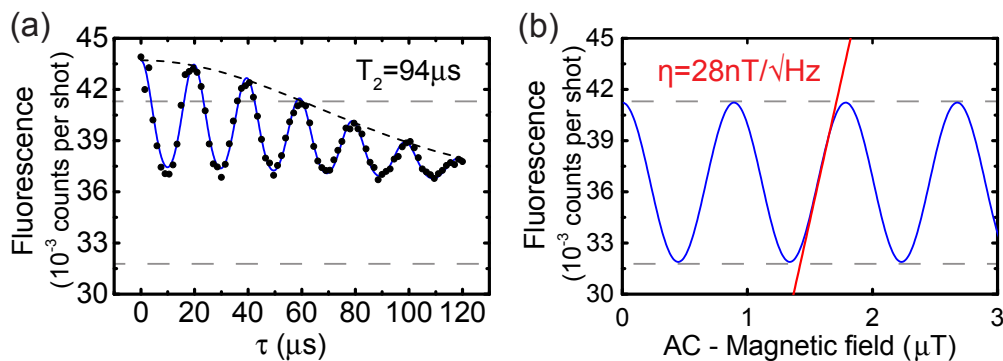
Figure B.3: (a) Spin echo spectroscopy: Data are plotted in black and a fit (see main text) is depicted in blue. (b) Signal for a fixed evolution time and a varying AC magnetic field strength at the frequency given by the evolution time. The red line indicates the maximum signal response at the optimal working point, which is used to deduce the sensitivity of $\eta = 28\,\text{nT}\sqrt{\text{Hz}}$ (data taken from [16]).

In order to achieve the maximum sensitivity, the evolution time will be set to a revival nearest to $T_2/2$. The resulting magnetic field dependent signal is depicted in Fig. B.3 (b) and can be described by:

$$I = I_{\text{avg}} \left[1 - \frac{C_{\text{pulsed}}}{e^{\frac{1}{4}}} \cos\left(2\pi\gamma_{\text{NV}} B_{\text{AC}} \frac{T_2}{2} \right) \right]. \tag{B.16}$$

Analogously to the sensitivity for Ramsey experiments the maximum signal (depicted in red in Fig. 1.8 (b)) can be deduced and the sensitivity for ac magnetometry can be described by

$$\eta_{\text{Spin Echo}} = \frac{\sqrt{2}e^{\frac{1}{4}}}{2\pi\gamma_{\text{NV}} C_{\text{pulsed}} \sqrt{I_{\text{avg}}} \sqrt{T_2}}. \tag{B.17}$$

For the depicted spin echo measurement of an NV center in a scanning probe, we obtain a sensitivity to AC-magnetic fields of $\eta_{\text{Spin Echo}} = 28\text{nT}/\sqrt{\text{Hz}}$, describing the NV centers ability to measure AC-magnetic fields.

B.4   Rabi oscillations

The Rabi signal (in counts per shot) is defined as:

$$I = I_{\text{avg}} \left[1 - C_{\text{pulsed}} \exp\left[-\left(\frac{\tau}{T_{\text{Rabi}}} \right)^n \right] \cos\left(2\pi\gamma_{\text{NV}} B_{\text{MW}}\tau \right) \right] \tag{B.18}$$

where I_{avg} is the average count rate, C_{pulsed} is the contrast for pulsed experiments, T_{Rabi} is the decay time in Rabi experiments and n is value that depends on the detail of the decoherence process and is set to 2. Note that some Rabi signals exhibits an $n \approx 1$, which can result from different noise and results in minor modifications of the sensitvity (see Sec.B.2). The fit to data yields $I_{\text{avg}} = 0.0434$ counts per shot, $C_{\text{pulsed}} = 0.0359$, $T_{\text{Rabi}} = 5.2\,\mu\text{s}$ and $B_{\text{MW}} = 88\,\mu\text{T}$. Also note that the decoherence time T_{Rabi} depends on the driving conditions [42, 181]. Under low driving conditions ($\gamma_{\text{NV}} B_{\text{MW}} << 1/T_{\text{Rabi}}$), T_{Rabi} is given by T_2^*, whereas under strong driving conditions ($\gamma_{\text{NV}} B_{\text{MW}} >> 1/T_{\text{Rabi}}$), the decay T_{Rabi} is given by T_1.

For the deduction of the sensitivity the formula introduced for Ramsey measurements can be applied. The optimal sensitivity for an exponential decay with $n = 2$ can be achieved for a MW pulse duration of $T_{\text{Rabi}}/2$. The signal is depicted in Fig. B.4 (b) and results in a sensitivity

$$\eta_{\text{Rabi}} = \frac{\sqrt{2}e^{\frac{1}{4}}}{2\pi\gamma_{\text{NV}} C_{\text{pulsed}} \sqrt{I_{\text{avg}}} \sqrt{T_{\text{Rabi}}}}. \tag{B.19}$$

For the depicted Rabi measurement of an NV center in a scanning probe, we obtain a sensitivity of $\eta_{\text{Rabi}} = 800\,\text{nT}/\sqrt{\text{Hz}}$ describing the NV centers ability to measure AC-magnetic fields in the GHz frequency range. Note that the contrast and coherence time of this NV center are small, which results in a small sensitivity. Assuming the
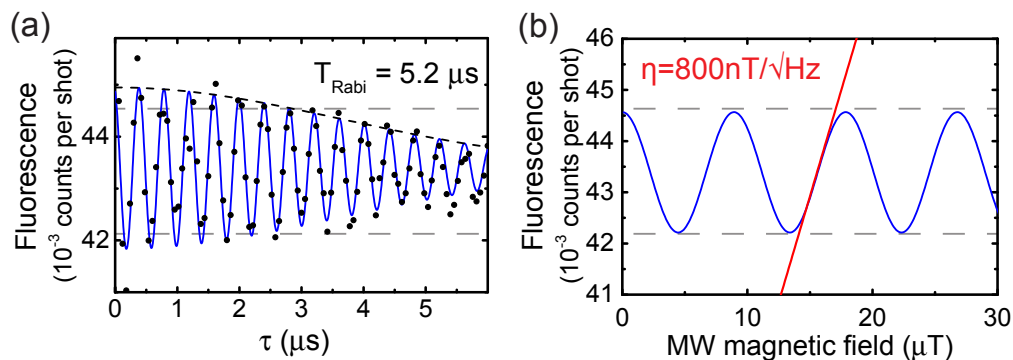
Figure B.4: (a) Rabi oscillations. Data are plotted in black and a fit (see main text) is depicted in blue. (b) Signal for a fixed evolution time and a varying MW magnetic field strength. The red line indicates the maximum signal response at the optimal working point, which is used to deduce a sensitivity of $\eta = 800\,\text{nT}\sqrt{\text{Hz}}$ (data taken from [17]).

optical properties of the NV center in Section B.3 increases the sensitivity by a factor of 4, which, combined with a coherence time under strong MW driving of $T_{\text{Rabi}} = T_1 \approx 1\,\text{ms}$, would result in an excellent sensitivity of $\eta_{\text{Spin Echo}} = 9\,\text{nT}/\sqrt{\text{Hz}}$. This sensitivity represents the maximum achievable sensitivity for measuring magnetic fields using Rabi oscillations.

Appendix C

Antiferromagnetic Stripe Fitting

In this appendix, we describe in detail the fitting routine applied to determine the moment density of the Cr_2O_3 stripes and discuss the fitting uncertainties. The fitting routine is adapted from the determination of the moment density of ferromagnetic stripes presented in Ref. [81].

C.1   Description of the fitting model

The stray field of Cr_2O_3 can be described by its boundary magnetization. Consequently, the stray field of tapered Cr_2O_3 stripes, which are uniformly magnetized perpendicular to the surface, can be modeled as the stray field of stairs carrying opposite currents. The strength of these currents is given by the moment density σ (see Chap. 3). The magnetic field of each current $B_{NV}^{(i)}$ can be calculated using the Biot Savart law (see Chap. 3), such that the overall magnetic field of the stripe is

$$B_{NV}(x, z) = \sum_{i=1}^{4n_{stairs}} B_{NV}^{(i)}(x + x_i, z + z_i). \tag{C.1}$$

The coordinates x_i, z_i are calculated using the AF film thickness t, the number of stairs n_{stairs} and the taper angle α_{right} and α_{left} for the right and left side of the stripe.

Using scanning NV magnetometry, the magnetic field is evaluated at the position of the NV center while the scanning probe is moved across the sample. Using atomic force feedback, the NV center is locked to a constant distance d_{NV} to the surface. Thus, the magnetic field is measured along a trajectory

$$\vec{r} = \begin{pmatrix} x \\ 0 \\ z \end{pmatrix} = \begin{pmatrix} x \\ 0 \\ d_{NV} + \text{topo(x)} \end{pmatrix}, \tag{C.2}$$
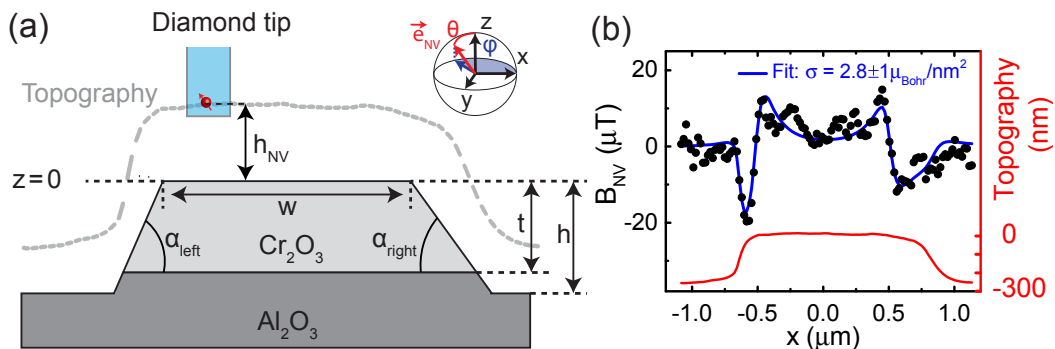
Figure C.1: (a) Schematic of the AF stripe used for determining the moment density. The NV center incorporated in the diamond tip is scanned along a trajectory given by the topography, while the magnetic field is evaluated. The NV center measures the magnetic field along its orientation $\vec{e}_{NV}$ $(\theta_{NV}, \varphi_{NV})$. (c) Measured topography (red) and magnetic field (black circles). Fitting a model for the magnetic field (blue) yields $\sigma = 2.8 \pm 1 \,\mu_{Bohr}/nm^2$ and $h_{NV} = 89 \pm 23 \,nm$.

where topo(x) is the measured topography. The average value of $\langle topo(x) \rangle_{stripe}$, when the scanning probe is on top of the stripe, is set to 0 and it becomes negative next to the stripe as illustrated in Fig. C.1. Note that we rescaled the coordinates of the measured topography, in order to correct for a scanning direction which is not orthogonal to the stripe (not along x in Fig. C.1) and possible wrong calibration of the scanner. For rescaling, we used the width ($w = 1 \,\mu m$) and the height ($h = 250 \,nm$) of the stripe as determined through calibrated atomic force measurements. As the NV center is incorporated in the scanning probe, the real position of the NV center can be shifted with respect to the measured topography. Hence, we integrated such a displacement, δx. The final formula of the magnetic field along the measured trajectory $\vec{r}(x)$ is a function $B_{NV}(\sigma, d_{NV}, \theta_{NV}, \varphi_{NV}, \delta x, w, h, t, \alpha_{right}, \alpha_{left})$, which depends on the moment density σ, the NV-to-surface distance d_{NV}, the NV orientation given by $\theta_{NV}, \varphi_{NV}$, the NV displacement δx and the parameters of the stripe, which are the width w and height h of the stripe, the real thickness of the AFM film t and the angles of the taper, α_{right} and α_{left}.

For precise determination of the moment density, we characterized several parameters, whose value we then fixed before performing the least square fitting. First of all, we performed calibrated atomic force measurements to determine t and geometrical parameters of the stripe ($w, h, \alpha_{right}, \alpha_{left}$), as summarized in table C.2. The taper angles, however, changed along the stripes (see Fig. 3.1) and we therefore determined these values using the least square fitting routine of the measured magnetic field. An additional parameter that can also be predefined is the NV orientation ($\theta_{NV}, \varphi_{NV}$). An NV center is aligned along one of the $\langle 111 \rangle$ crystal axis of the diamond. In previous measurements, we identified that our scanning probes

have a (100) top surface and the edges are aligned along the (110) crystal orientation (for the scanning probes used in this experiment). Hence, the possible NV alignments in our experiments are $\theta_{\mathrm{NV}} = \pm 54, \pm(180 - 54)\,^\circ$ and $\varphi_{\mathrm{NV}} = 0, \pm 90, 180\,^\circ$. As the y-component of our magnetic field of the stripes is 0 the magnetic field is independent of the sign of φ_{NV} and θ_{NV}. Furthermore, because the measured stray field on top of the stripe is symmetric, we can identify that the NV center must be aligned along the stripe axis $\varphi_{\mathrm{NV}} = 90\,^\circ$ (or $\varphi_{\mathrm{NV}} = -90\,^\circ$). Finally, we assume $\theta_{\mathrm{NV}} = 54\,^\circ$, which results in a positive current, corresponding to a magnetization state of spin up at the top surface. Note that $\theta_{\mathrm{NV}} = 180 - 54\,^\circ$ and a negative current would result in exactly the same magnetic field. Thus, for a definite determination θ_{NV} would need to be characterized externally. The exact angles of the scanning probes with respect to the sample can be altered by the alignment of the sample and the scanning probes. We apply a stereo microscope for transferring the scanning probes to our atomic force head, which allows for an alignment of the scanning probes within a few degrees to the horizontal plane of the setup as characterized by previous measurements (see Chap. 2). Moreover, we expect only minor contribution from the alignment of sample and assumed an uncertainty of $\pm 10\,^\circ$.

C.2 Determination and fitting uncertainties

We fitted the described model to the stray field of 16 lines across the stripes in order to average over possible variations in the moment density. This averaging allows for a precise determination of the average moment density. The overall error cited in Chap. 3.1 consists of a statistical error and a systematic error, which is described by the uncertainty of the predefined parameter and the uncertainty of the fit.

   We independently fitted each line and extracted the free fitting parameters that best reproduce the measurement. Afterwards, we determined the statistical error given by the standard error of each fit parameter, as summarized in table C.1.

Table C.1: Overview of the free fitting parameters. The moment density σ, the NV-to-sample distance h_{NV}, the displacement δx and the angles of the taper of the stripes $(\alpha_{\mathrm{right}}, \alpha_{\mathrm{left}})$ are determined using a least squares fitting algorithm. The average value of each parameter over 16 linecuts as well as the statistical and fitting error are summarized.

Parameter	Average $\langle X_i \rangle$	Fitting error $P_{i,\mathrm{fit}}$ (%)	Statistical error $P_{i,\mathrm{stat}}$ (%)
σ	$2.76\mu_{\mathrm{Bohr}}/\mathrm{nm}^2$	23.0	9.6
h_{NV}	$89.0\,\mathrm{nm}$	22.6	6.7
δx	$60.6\,\mathrm{nm}$	65.8	12.5
α_{right}	$94.8\,^\circ$	28.3	5.9
α_{left}	$46.0\,^\circ$	36.8	5.8

The fitting error given in table C.1 is the average value of least squares fit.

Next, we consider the uncertainties of the fit parameters P_{i,p_j}, which are induced by the uncertainty of the predefined constants [23]. We set one of the characterized values to $x_{\pm j} = (1 \pm p_j) \langle x_j \rangle$, while leaving all other parameters at their nominal value, thereby allowing us to determine the mean of the fitting parameter $\langle X_i \rangle_{x_{\pm j}}$. The error associated with the modified parameter is defined as

$$P_{i,p_j} = \frac{\left| \langle X_i \rangle_{x_{+j}} - \langle X_i \rangle_{x_{-j}} \right|}{2 \langle X_i \rangle_{\langle x_j \rangle}}. \tag{C.3}$$

All uncertainties of the constants and the resulting error are summarized in table C.2 and the overall error corresponding to the uncertainties of the constants is calculated for σ and h_{NV}.

Table C.2: Overview of the precharacterized constants. The geometrical parameters of the stripe w, h and the film thickness t were determined using calibrated atomic force measurements. The NV orientation was determined from the crystal orientation and the measured magnetic field (see main text). The errors of the moment density P_{σ,p_j} and the height P_{h_{NV},p_j}, induced from the uncertainty of the predefined uncertainties are summarized.

Parameter x_j	Average $\langle x_j \rangle$	Uncertainty	$P_{\sigma,p_j}(\%)$	P_{h_{NV},p_j} (%)
t	$200\,\mathrm{nm}$	$20\,\mathrm{nm}$	7.9	4.5
w	$1\,\mu\mathrm{m}$	$50\,\mathrm{nm}$	8.0	5.3
h	$250\,\mathrm{nm}$	$20\,\mathrm{nm}$	1.4	3.1
θ_{NV}	$54\,^\circ$	$10\,^\circ$	26.2	0.02
φ_{NV}	$90\,^\circ$	$10\,^\circ$	5.13	7.1
$P_{i,\mathrm{const}} =$	$\sqrt{\sum P_{i,p_j}^2}$		$29.0\,\%$	$10.4\,\%$

The overall uncertainty can finally be calculated by

$$P_i = \sqrt{P_{i,\mathrm{stat}}^2 + P_{i,\mathrm{fit}}^2 + P_{i,\mathrm{const}}^2}, \tag{C.4}$$

which yields an error of $P_\sigma = 38.2\,\%$ and $P_{h_{\mathrm{NV}}} = 25.7\,\%$. Thus, with this procedure, we can state the moment density as $\sigma = 2.8 \pm 1\,\mu_{\mathrm{Bohr}}/\mathrm{nm}^2$ and the NV-to-sample distance as $h_{\mathrm{NV}} = 89 \pm 23\,\mathrm{nm}$.

List of Abbreviations

AC	Alternating current
AF	Antiferromagnet
AFM	Atomic force microscope
C	Carbon
CL	Cathodoluminescence
CFM	Confocal fluorescence microscopy
CW	Continuous wave
DC	Direct current
es	Excited state
ESEEM	Electron spin echo envelope modulation
ESR	Electron spin resonance
FIB	Focused ion beam
FWHM	Full width at half maximum
gs	Ground state
HSQ	Hydrogen silsesquioxane
ICP-RIE	Inductively coupled reactive ion etching
MRFM	Magnetic resonance force microscope
MRI	Magnetic resonance imaging
MW	Microwave
N	Nitrogen
NA	Numerical aperture
ND	Nanodiamonds
NMR	Nuclear magnetic resonance

NV center	Nitrogen vacancy center
ODMR	Optically detected magnetic resonance
PEEM	Photoemission electron microscopy
PSF	Point spread function
RMS	Root mean square
SEM	Scanning electron microscopy
SHPM	Scanning Hall probe microscopy
SQUID	Superconducting quantum interference device
SNR	Signal to noise ratio
TEM	Tunneling electron microscopy
TF	Tuning fork
TTL	Transistor-transistor logic
UV	Ultraviolet
XMCD	X-ray magnetic circular dichroism
XMLD	X-ray magnetic linear dichroism
ZFS	Zero field splitting
ZPL	Zero phonon line

List of Publications

1. E. Neu, P. Appel, M. Ganzhorn, J. Miguel-Sanchez, M. Lesik, V. Mille, V. Jacques, A. Tallaire, J. Achard and P. Maletinsky *Photonic nano-structures on (111)-oriented diamond*, Appl. Phys. Lett. **104**, 153108 (2014), URL

2. J. Teissier, A. Barfuss, P. Appel, E. Neu, P. Maletinsky, *Strain Coupling of a Nitrogen-Vacancy Center Spin to a Diamond Mechanical Oscillator*, Phys. Rev. Lett. **103**, 020503 (2014), URL

3. D. Riedel, D. Rohner, M. Ganzhorn, T. Kaldewey, P. Appel, E. Neu, R. J. Warburton, P. Maletinsky, *Low-Loss Broadband Antenna for Efficient Photon Collection from a Coherent Spin in Diamond*, Phys. Rev. Applied **2**, 064011 (2014), URL

4. J. Teissier, A. Barfuss, P. Appel, E. Neu, P. Maletinsky, *Strain Coupling of a Nitrogen-Vacancy Center Spin to a Diamond Mechanical Oscillator*, Phys. Rev. Lett. **103**, 020503 (2014), URL

5. P. Appel, M. Ganzhorn, E. Neu, P. Maletinsky, *Nanoscale microwave imaging with a single electron spin in diamond*, New J. Phys. **17**, 112001 (2015), URL

6. C. Arend, P. Appel, J.N. Becker, M. Schmidt, M. Fischer, S. Gsell, M. Schreck, C. Becher, P. Maletinsky, and E. Neu, *Site selective growth of heteroepitaxial diamond nanoislands containing single SiV centers*, Appl. Phys. Lett. **108**, 063111 (2016), URL

7. L.Thiel, D. Rohner, M. Ganzhorn, P. Appel, E. Neu, B. Mueller, R. Kleiner, D. Koelle, P. Maletinsky, *Quantitative nanoscale vortex imaging using a cryogenic quantum magnetometer*, Nature Nanotech. **11**, 677-681 (2016), URL

8. P. Appel, E. Neu, M. Ganzhorn, A. Barfuss, M. Batzer, M. Gratz, A. Tschoepe, P. Maletinsky, *Fabrication of all diamond scanning probes for nanoscale magnetometry*, Rev. Sci. Instrum **87**, 063703 (2016), URL

9. T. Kosub, M. Kopte, R. Hühne, P. Appel, B. Shields, P. Maletinsky, R. Hübner, M.O. Liedke, J. Fassbender, O.G. Schmidt, D. Makarov, *Purely antiferromagnetic magnetoelectric random access memory*, Nature Comm. **8**, 13985 (2017), URL

10. D. Riedel, I. Söllner, B. J. Shields, S. Starosielec, P. Appel, E. Neu, P. Maletinsky, R. J. Warburton, *Deterministic enhancement of coherent photon generation from a nitrogen-vacancy center in ultrapure diamond*, ArXiv Preprint: arXiv:1703.00815 (2017), URL

11. I. Gross, W. Akhtar, V. Garcia, L. J. Martínez, S. Chouaieb, K. Garcia, C. Carrétéro, A. Barthélémy, P. Appel, P. Maletinsky, J.-V. Kim, J. Y. Chauleau, N. Jaouen, M. Viret, M. Bibes, S. Fusil and V. Jacques, *Real-space imaging of non-collinear antiferromagnetic order with a single spin magnetometer*, submitted

12. P. Appel, B. J. Shields, T. Kosub, D. Makarov, P. Maletinsky, *Real Space Stray Field Imaging of Antiferromagnets*, to be published

Acknowledgments

I had the pleasure to meet and work with many extraordinary people during this Ph.D. thesis. Many results would not have been possible without their guidance, support and friendship. I thank everybody who contributed to this work as a colleague, friend or member of my family.

First and foremost, I would like to express my sincere gratitude to my supervisor, Patrick Maletinsky, for his continuous guidance of my Ph.D. research. He accepted me as the first student of his group and taught me all the details of NV magnetometry. Besides sharing his tremendous knowledge and expertise, he also motivated me with his unending enthusiasm, which is contagious. His inputs were always inspiring and his advices helped me to become a researcher. I enjoyed working with Patrick and thank him for his faith in me and my work.

When starting my Ph.D., I had a excellent mentor, Elke Neu. She and Patrick taught me the basics of microscopy, without which it would have been impossible to set up the magnetometer. Afterwards, during the endless hours developing the scanning probes, we often met in the evening, discussed about various things in life and became friends. I thank her not only for the outstanding teamwork in the lab, but also for her inputs, even after she left the group. Her courage in finding solutions motivated me and I highly appreciated working with her.

After my first year doing mostly nanofabrication, Marc Ganzhorn joined our team. Throughout my thesis, Marc and I worked together on several projects. He always gave me assistance, helped me find solutions and made me think from a different perspective. I thank Marc for all discussions – scientific and non-scientific – and count myself fortunate to have him as a co-worker, mentor and friend.

When the setup was fully operational and started to produce the first results, I had the pleasure to work with Brendan Shields. His inputs on the experiments were always inspiring. I thank him for patiently reading the manuscripts and for all his tips, which helped me to improve the presentation of the results.

In the end of my Ph.D. thesis, when spending most of the writing, I was lucky to have Natascha Hedrich as colleague. I thank Natascha for proofreading this work, which helped a lot to improve this thesis.

Throughout my Ph.D. work, Arne Barfuss, Daniel Riedel, Dominik Rohner, Lucas Thiel, and Jean Teissier always supported me. I thank all of them for the assistance they gave me during the last years.